Master Thesis, Department of Geosciences

Comparative study of the Nise formation seismic response between Møre and Vøring basin

Case studies

Juan Sáez Barrero

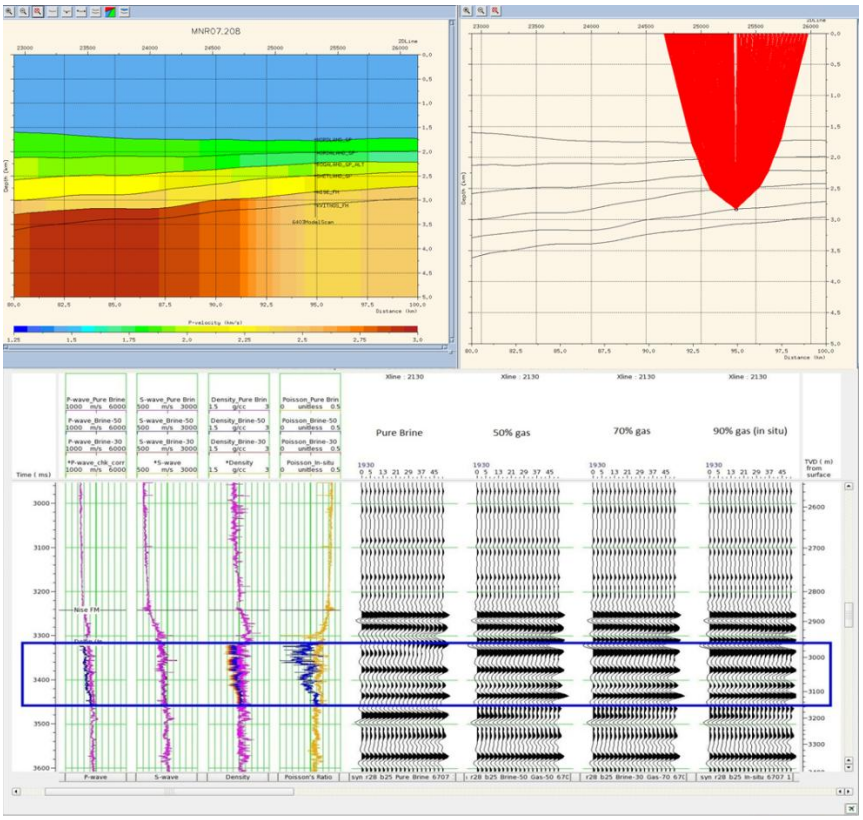

UNIVERSITY OF OSLO
FACULTY OF MATHEMATICS AND NATURAL SCIENCES

Comparative study of the Nise formation seismic response between Møre and Vøring basin

Case studies

Juan Sáez Barrero

Master Thesis in Geosciences
Discipline: Geophysics
Department of Geosciences
Faculty of Mathematics and Natural Sciences

University of Oslo

December 2012

Tutors: Isabelle Lecomte, (UiO) and Pujianto Lukito Harjo, (Repsol Norge A.S.).
This work is published digitally through DUO – Digitale Utgivelser ved UiO
http://www.duo.uio.no
It is also catalogued in BIBSYS (http://www.bibsys.no/english)

Acknowledgements

I would like to express my gratitude to my supervisors Isabelle Lecomte (UiO/NORSAR) and Pujianto Lukito Harjo (Repsol Norge A.S.) for their support and encouragement throughout my thesis work. I am very grateful to them for their advices and feedbacks on my work.

I also thank Repsol Norge A.S. for providing me the information and resources necessary to carry on this work and the opportunity to see the daily work in an oil company. I am also grateful to the staff at the exploration department for helping me whenever I had any technical issue.

I would like to thank NORSAR for granting me access to their office and software. I would also like to thank the people of NORSAR who were very kind with me during the time that I have spent at their offices.

Finally, my special thanks to my family for their support and patience, not only during this work, but also during the last years.

Summary

The Vøring and Møre Basins are located in the western part of the Norwegian Sea Continental margin and are characterized by huge thicknesses of Cretaceous sediments. The main play in the area is formed by Nise formation (Fm.) sandstones, charged by a hypothetical Cretaceous or proven Upper Jurassic source rock, and trapped along rotated fault blocks and Tertiary domes.

The aim of the present work is to analyse and compare four case studies (two wells in Vøring Basin and two wells in Møre Basin) in which nearby seismic sections show variation in amplitude with incident angle within the Nise Fm. This variation was sometimes associated to the presence of hydrocarbon; however that was not always the case.

Well data is used to create AVO (amplitude vs Offset)-AVA (amplitude vs angle) models, which are studied by using the three-term Aki-Richards approximation of the Zoeppritz equation, and then compared with the available seismic. Three of the models are able to replicate the same amplitude-variation trend observed in seismic. In the Vøring Basin cases, models show that the seismic response is largely affected by the presence of gas. On the other hand, in the Møre Basin cases, the increment in amplitude with incident angle is not as strong as it was initially observed and relates more to lithological change.

In addition, 2D velocity models are built and seismic modelling (ray tracing) is used to investigate possible wave-propagation effects in the amplitude variation with incident angle. This study discuss that the commonly-accepted direct relation reflectivity-amplitude cannot be taken for granted and that other factors like overburden or the reflector shape must be considered before AVO-AVA studies. However, once the effect of these factors is not present or it is removed, the AVO-AVA results can be considered valid. This is the case of the present work, where no remarkable wave-propagation effects have been found.

Table of Content

ACKNOWLEDGEMENTS ..... **V**

SUMMARY ..... **VI**

CHAPTER 1: INTRODUCTION **1**

1.1 OBJECTIVES 2

1.2 DATABASE AND METHODOLOGY 3

1.2.1 Methodology *6*

1.3 STRUCTURE OF THE REPORT 7

CHAPTER 2: GEOLOGICAL FRAMEWORK **8**

2.1 STRUCTURAL DESCRIPTION 8

2.2 STRUCTURAL EVOLUTION 9

2.3 STRATIGRAPHY DESCRIPTION AND DEPOSITIONAL ENVIRONMENT 11

2.3.1 Upper Cretaceous Formations *11*

CHAPTER 3: AVO-AVA FORWARD MODELLING **14**

3.1 THEORETICAL FRAMEWORK 14

3.2 METHODOLOGY 14

3.2.1 Data Preparation *14*

3.2.2 AVO-AVA Modelling *20*

3.3 RESULTS 22

3.3.1 Vøring Basin cases *22*

3.3.2 Møre Basin cases *28*

3.4 DISCUSSION 33

3.4.1 Gas effect in Vøring Basin cases *33*

3.4.2 Flat event analysis in Solsikke and Luva gas discovery reservoir base *36*

3.4.3 No-sand reservoir case in Møre Basin *37*

3.4.4 Qualitative comparison with seismic data *37*

CHAPTER 4: RAY-TRACING MODELLING **40**

4.1 THEORETICAL FRAMEWORK 40

4.2 METHODOLOGY 42

4.2.1 Seismic interpretation *43*

4.2.2 NORSAR-2D Data Preparation 44

4.2.3 Creation of a model in depth 45

4.2.4 Model calibration 46

4.2.5 Seismic modelling 50

4.3 RESULTS 51

4.3.1 Review of angle ranges used for partial stack sections 51

4.3.2 Geometrical spreading 52

4.4 DISCUSSION 53

CHAPTER 5: CONCLUSIONS 56

REFERENCES 58

LIST OF FIGURES 61

LIST OF TABLES 65

APPENDIX 67

APPENDIX A: FULL STACK AND OBSERVED VARIATION IN PARTIAL STACKS 67

APPENDIX B: AVO-AVA THEORETICAL FRAMEWORK 72

Reflection coefficient: variation with incident angle 72

1-D convolutional trace model 74

Gassmann Fluid substitution 75

AVO classification scheme 77

APPENDIX C: WELL CORRELATIONS 79

APPENDIX D: FLAT EVENTS 82

APPENDIX E: DETAILED CALCULATION OF R_p, G AND F 83

APPENDIX F: INTERVAL VELOCITY ESTIMATION AND DEPTH CONVERSION WITH NORSAR-2D. 86

APPENDIX G: SCRIPT TO CONVERT STACKING VELOCITY FROM CHARISMA (*.VG_VBASE) TO NORSAR-2D (*.STAB) FORMAT. 88

GLOSSARY 90

Chapter 1: Introduction

The Norwegian Sea continental margin is the area between parallels 62ºN and 69ºN (Blystad et al., 1995). Vøring and Møre Basins are located in the western part of the Norwegian Sea Continental margin and they have been explored since 1987 (first well, 6607/5-1) (Fjellanger et al., 2005).

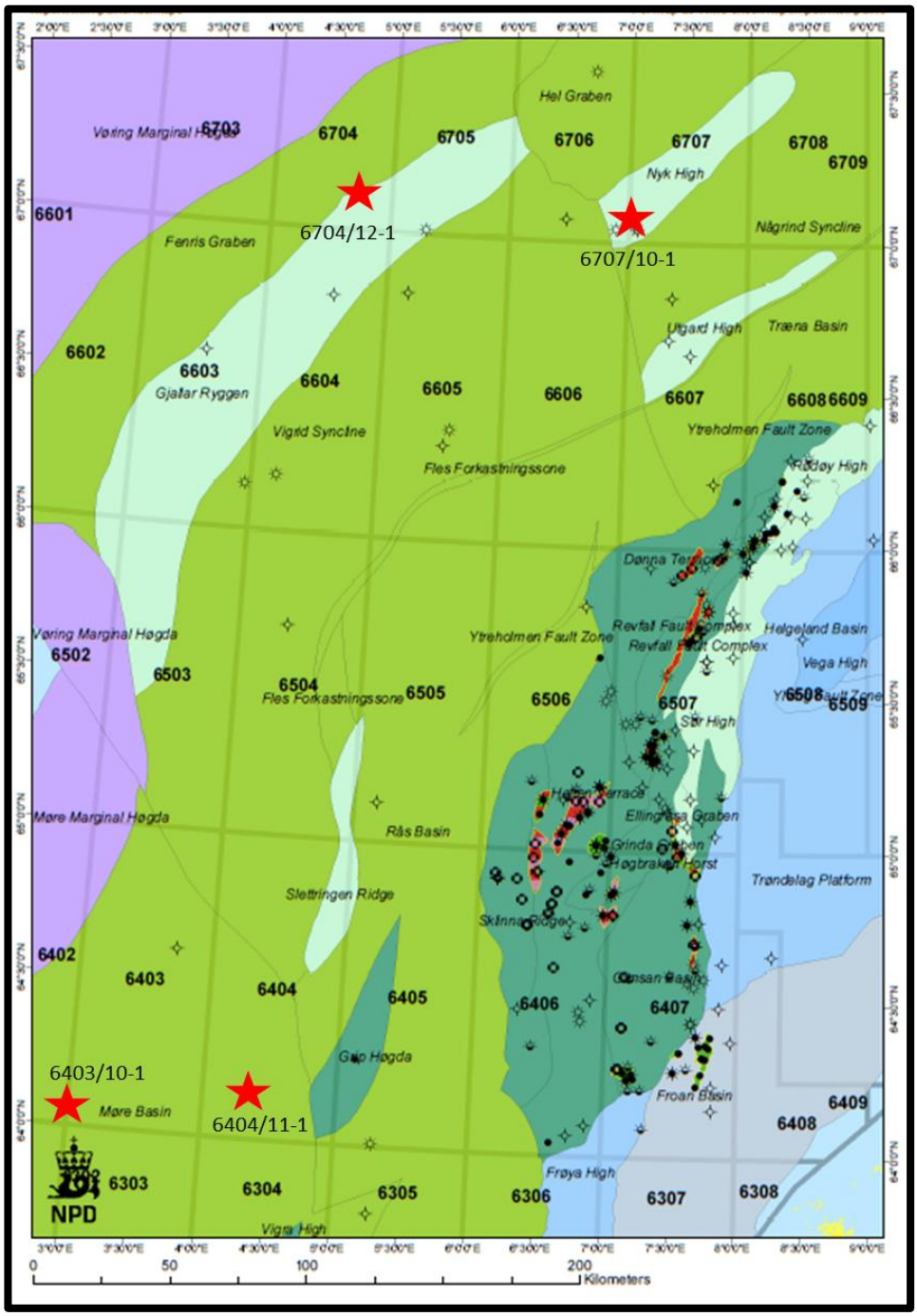

FIGURE 1. 1 - VØRING AND NORTHERN MØRE BASINS WITH THE MAIN GEOLOGICAL FEATURES. LOCATIONS OF WELLS USED IN THIS REPORT ARE IDENTIFIED WITH A RED STAR (MODIFIED FROM NORWEGIAN PETROLEUM DIRECTORATE – NPD-FACTMAPS).

The Vøring and Møre Basins are characterized by a huge thickness of the Cretaceous sediments (Brekke et al., 1999). One of the prospective intervals in the area is the Upper Cretaceous sandstones, with three main formations: Lysing Fm., Nise Fm., and Springar Fm. (Brekke et al., 1999). The depositional environment interpretation for the Lysing Fm. varies from shallow to deep marine -submarine fan deposits- (Dalland et al., 1988). Nise Fm. and Springar Fm. are interpreted as deep-water fan systems (Fjellanger et al., 2005).

Gas discoveries have been made in the northern Vøring Basin in the Nise Fm. and Springar Fm. (Luva, Asterix, and Gro). The Luva discovery shows a very distinct seismic response in the partial angle stacks, with increase in amplitude from near-angle stack to far-angle stack.

In the northern Møre Basin and for the same formations, some wells have been drilled based on a similar bright amplitude in the far offset, but they failed to find reservoir sandstones. Instead, they found inter-bedded laminations of siltstones, mudstones and limestone streaks.

1.1 Objectives

In order to better understand the reasons for apparent similar seismic responses between the two basins within the same formations, while lithology and fluid contents appeared to be different, the Nise Fm. seismic response is especially investigated by modelling in this project. To achieve that, four case studies are carried out in the area, i.e., two in the Vøring Basin (reservoirs) and two in the Møre Basin (no reservoirs) (see Figure 1.1):

Vøring Basin – reservoirs

- Well 6707/10-1 (Luva discovery) is located in the Nyk High, in the North Vøring Basin, and it was the first well drilled in the Vøring Basin deep water area. Its main objective was to identify the presence, quality, and fluid content of the Nise Fm. (Norwegian Petroleum Directorate – NPD- factpages). It found gas in the Nise Fm. and therefore will represent the gas-saturated sand case in this study.
- Well 6704/12-1 is located on the Gjallar Ridge, in North-West Vøring Basin, and it was drilled to test the petroleum potential of the Upper Cretaceous formations. The Latest Campanian sandstones reservoir quality was excellent (NPD factpages) but only found low gas saturations. It will represent a marginally gas-saturated sand case in this study.
- Note that in both Nyk High and Gjallar Ridge wells, the sandstones facies of Nise Fm. are referred as Delfin Fm.

Møre Basin – no reservoirs

- Well 6403/10-1 is located in the Solsikke dome structure, in the North-West Møre Basin. The main objective was a potential hydrocarbon accumulation above a flat event in the Nise Fm., but the well was dry. Mudstone and high content of siltstone (with high porosity and low permeability) were encountered in the Nise Fm. (NPD factpages). It represents a purely lithological flat event or "non-hydrocarbon flat spot" case in the study.

- Well 6404/11-1 is located in North Møre Basin. One of the drilling objectives was again the Nise Fm. sandstones, but they showed to be poorly developed (NPD factpages). It represents a no-sand reservoir case in this study.

Partial-stack time migrated sections (Near stack, Near/mid stack, Far/Mid stack, Far stack) are available close to the three last cases, showing variations in amplitude with angle according to observations (See appendix A and Figure 1.2).

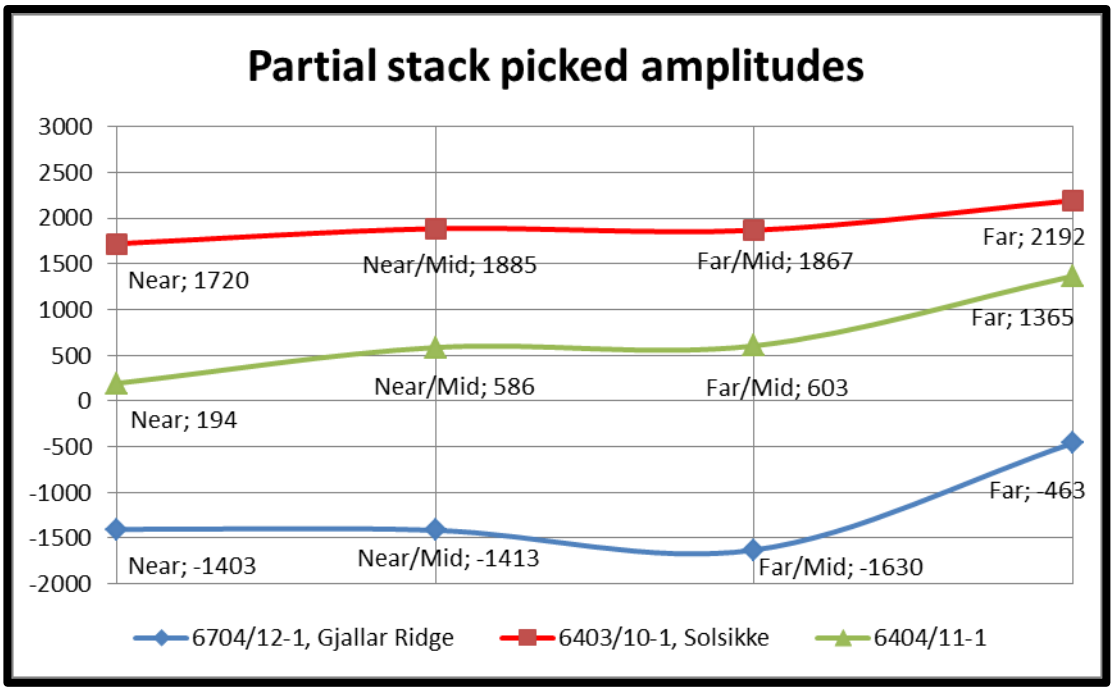

FIGURE 1. 2 - PICKED AMPLITUDES IN PARTIAL-STACK SECTIONS: NEAR STACK, NEAR/MID STACK, FAR/MID STACK, FAR STACK.

The objectives of the present work were therefore to:

- Check whether the observed variation in amplitude with angle can be reproduced through standard forward modelling of the wells (1D-model based).
- Better take into account potential complex wave propagation effects by building 2D velocity models used for seismic modelling (ray tracing) in order to further study amplitudes.
- Find a plausible explanation for the observed seismic behaviour in each of the wells.

1.2 Database and Methodology

Composite petrophysical logs of wells 6403/10-1 (Solsikke), 6404/11-1, 6704/12-1 (Gjallar ridge) and 6707/10-1 (Luva gas discovery) are used in this study as the input of forward modelling of the wells. These logs include:

- Caliper (inch), which measures the diameter of the borehole and allows the identification of areas with potential erratic measurements during logging.
- Compressional sonic (us/ft), from which P-wave velocity, V_p (m/s), is calculated.

- Shear sonic (us/ft), from which S-wave velocity, V_s (m/s), is derived.
- Bulk density (g/cc).
- Gamma ray (API) to estimate shale content.

The Kelly Bushing level is 25 meters for all wells and depths are given in Measured Depth (MD, m). In addition check-shot correction is used to constrain the time-depth curve between seismic section and wire logs.

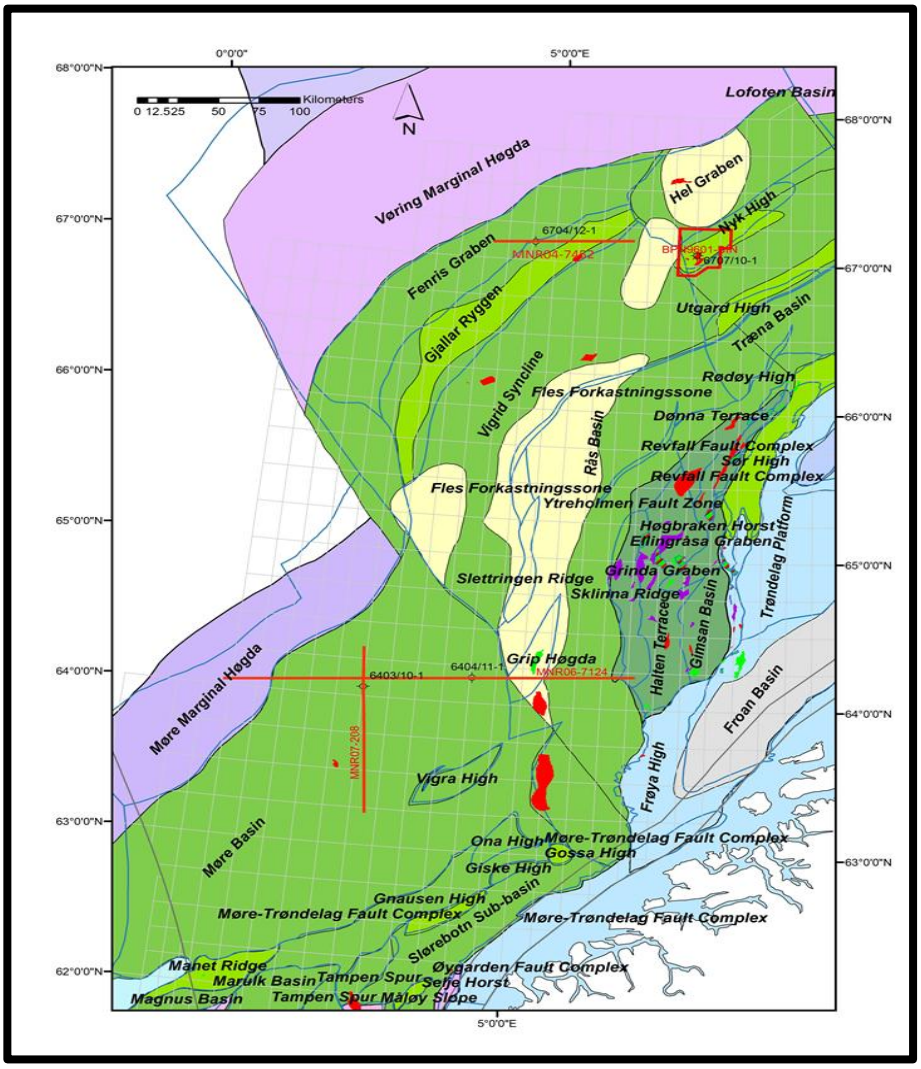

FIGURE 1. 3 - WELLS AND SEISMIC LINES LOCATIONS SUPERIMPOSED ON THE MAIN GEOLOGICAL FEATURES.

Three 2D seismic sections close to the wells are also used (MNR07-208, MNR06-7124 and MNR04-7452) (Figure 1.3):

- Full-stack time migrated sections (appendix A) are interpreted for input to ray-tracing modelling (picked time-migrated horizons). They are also used to extract the wavelet in wells 6403/10-1 (Solsikke), 6404/11-1 and 6704/12-1 (Gjallar ridge), as it will be showed later in Chapter 3.

- Partial-stack time migrated sections (appendix A) are also available. According to the Fugro processing report (confidential), the stacking velocity field is smoothed and interval velocities are calculated with Dix approximation. A bending-ray method is later used to identify incident angles and to produce a field of angle-based mute functions for each CMP (Common Mid-Point). Finally, angle-band mutes defined in Table 1.1 are applied and the result (each angle band) is stacked to produce these partial-stack sections.

TABLE 1. 1 – ANGLE RANGE FOR EACH PARTIAL STACK SECTION

Stack volume	Inner angle (degrees)	Outer angle (degrees)
Near	5	20
Near-Mid	15	30
Far-Mid	25	40
Far	35	50

The partial-stack sections are qualitatively compared with AVO-AVA modelling output. Ray-tracing modelling is used to check the relation angle-offset and the validity of the selection of these angles.

In Table 1.2, note that these seismic sections do not cross the wells; they are at a distance of between 20 m in well 6403/10-1 (Solsikke) and 330 m in well 6404/11-1. This represents a major uncertainty for wells 6704/12-1 (Gjallar ridge) (250 m) and 6404/11-1 (329 m) in this study.

3D seismic cube BPN9601 (Figure 1.3) is used in well 6707/10-1 to extract the wavelet, as it will be explained in Chapter 3.

TABLE 1. 2 – WELL/SEISMIC LINE RELATION. WELL POSITION (WELL PROJECTION ON THE LINE) AND WELL/SEISMIC LINE DISTANCE.

Well	Seismic line	Position	Distance (m)
6403/10-1	MNR07-208	CPD 25162	19.48
6404/11-1	MNR06-7124	CPD 42879	326.87
6704/12-1	MNR04-7452	CPD 14168	248.66
6707/10-1	BPN9601	Inline 1930, Xline 2130	0

1.2.1 Methodology

Log edition

The Interactive Petrophysics software is used for log quality control and editing. Some logs that are missing (e.g., shear sonic in well 6404/11-1) are generated from other existing input logs based on empirical relations and/or linear regressions, as will be explained.

AVO-AVA modelling

The Hampson-Russell software is used for AVO-AVA modelling. The Geoview module is the main interface of the Hampson-Russell software and it is the link between different Hampson-Russell modules:

- Well log information is loaded in Well database and it is available for other utilities for further analysis. Check-shot correction and well correlations were done from here.
- Seismic information is loaded in the Seismic Section module and horizons in areas of interest are interpreted from that module.
- eLog module is used to upscale well log data by creating blocks of tens of meters. This is necessary because log data measures with a resolution of centimetres whereas seismic data with a resolution of up to a few tens of meters.
- AVO Modelling is used to define different pore saturation scenarios (Fluid Replacement Modelling - FRM - based on Biot-Gassmann equations) and to generate synthetic of NMO-corrected CMP gathers (1D model).
- Synthetic seismic data amplitudes are extracted and analysed with the AVO Analysis module.

Interpretation

The Charisma seismic module is used for interpretation of horizons that are later used to build velocity models for 2D ray-tracing modelling. These horizons correspond to the top of the principal groups and formations given by the well logs and are in accordance with NPD definitions.

Ray-tracing modelling

NORSAR-2D (N2D) is the ray-modelling software that was used here to first create 2D P-wave velocity (V_p) models from interpreted time-migrated horizons and stacking velocities, and then to perform ray tracing in order to study propagation effects on seismic amplitudes. In this study,

- Laterally-varying interval velocities are estimated from stacking velocities and full stack time-migrated horizons following the approach of Hubral (1980).

- In interaction between the N2D Velocity Estimator and Model Builder modules, time horizons are depth-converted by means of ray tracing using the estimated interval velocities. This is done in a layer per layer mode starting from the sea bottom.

1.3 Structure of the report

The report is structured in chapters and appendices. Chapters represent the workflow of the investigation, whereas appendices provide more detailed information about specific topics.

Chapter 2 introduces the geological framework of the area, with the presentation of the main structures, the structural evolution and a stratigraphy description of Upper Cretaceous formations.

Chapter 3 focuses on the study of amplitude variations as a function of incident angle. AVO-AVA forward models are produced to determine the relationship between elastic rock properties and AVO-AVA responses. In the two discovery wells (Vøring Basin), various gas saturation scenarios are also modelled to investigate the effect of gas on seismic response.

In Chapter 4, modelling wave-propagation effects which may potentially affect the observed amplitudes on the seismic results are studied by using ray tracing modelling. The advantage of a seismic model against AVO-AVA analysis is that lateral velocity variations (2D model) are taken into account. Incident-angle ranges associated with the various partial stack sections are also reviewed for control.

Finally, in Chapter 5, the main conclusions of the project are presented after some discussions.

Chapter 2: Geological framework

2.1 Structural description

The Norwegian Continental Shelf (NCS) is divided into three main provinces for hydrocarbon exploration: North Sea, Norwegian Sea continental margin and Western Barents Sea. Norwegian Sea continental margin is located between parallels 62ºN and 69ºN. The main structural elements can be recognized in Figure 2.1, according to Blystad et al. (1995) naming convention.

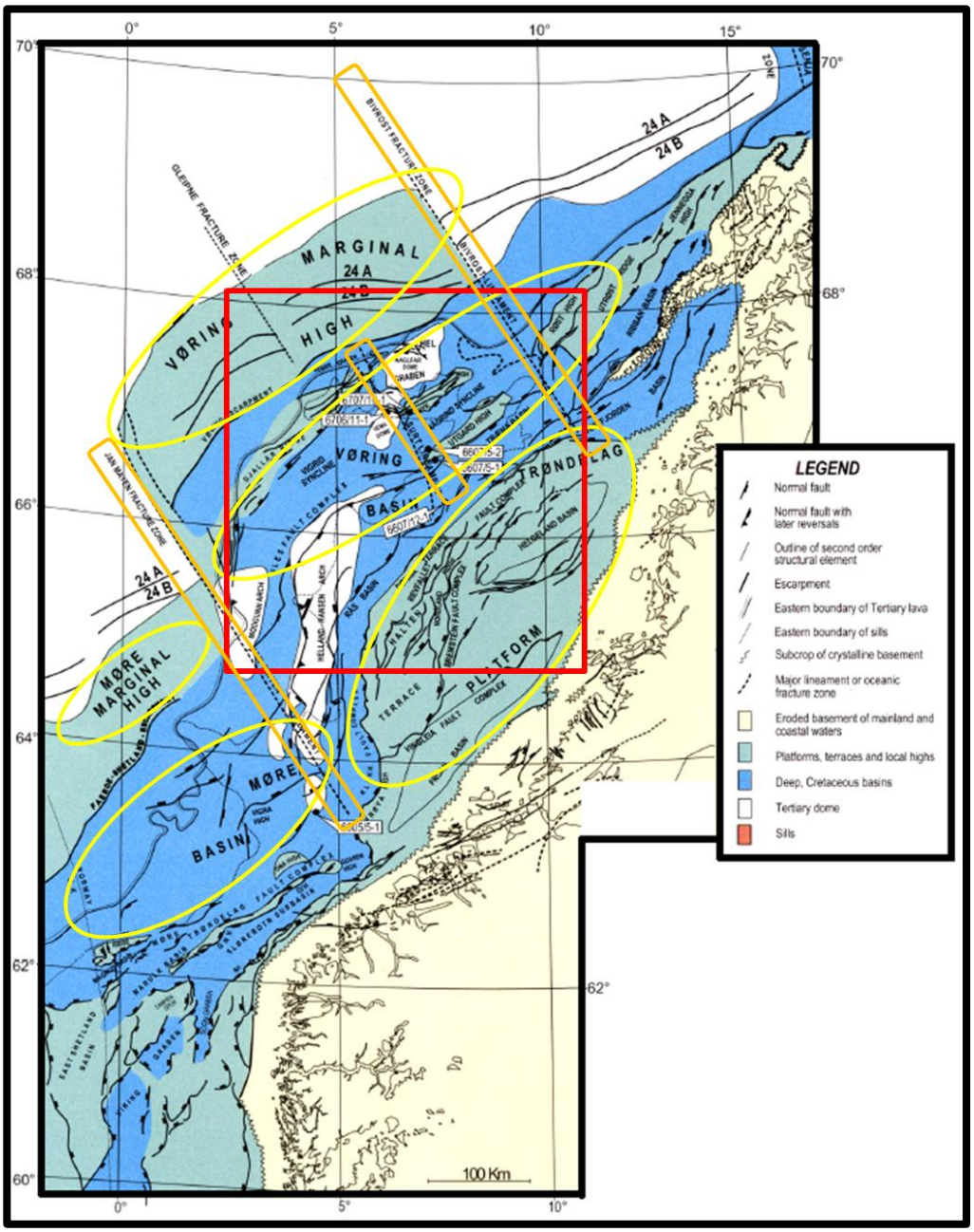

FIGURE 2. 2 - MAIN STRUCTURAL ELEMENTS IN NORWEGIAN SEA CONTINENTAL SHELF. MAIN STRUCTURES ARE HIGHLIGHTED. AREA IN THE BOX IS ZOOMED IN FIGURE 2. FIGURE MODIFIED AFTER BREKKE (2000).

The following structures can be distinguished (Figure 2.1):

- Vøring and Møre Basins: Deep Cretaceous basins in the central part with a general NE-SW trending. They are characterized by a huge thickness of the Cretaceous sediments (Brekke et al., 1999). Træna Basin and Rås sub-Basin, in the northeast and southeast of the Vøring Basin, are also Cretaceous basins.
- Vøring and Møre Marginal highs: Platforms to the west of the basins, with thick, Lower-Eocene basalt flows that make difficult to identify the underlying sediments (Brekke et al., 1999).
- Trøndelag Platform: Upper Jurassic/Lower Cretaceous Platform to the east in the central area.
- Tertiary Domes: From south to north, Helland Hansen Arch, Modgunn Arch, Vema Dome and Naglfar Dome. Most of them located in Vøring Basin.

The Norwegian Sea continental margin is crossed by NW-SE trending lineaments: Jan Mayer, Surt and Bivrost. Jan Mayer acted as a barrier between tectonically active Vøring Basin and inactive Møre Basins during Upper Cretaceous and Tertiary (Brekke et al., 1999).

2.2 Structural evolution

The present structural configuration is a consequence of different extensional episodes that occurred in Upper Jurassic to Lower Cretaceous and Upper Cretaceous to Paleocene rifts following by compression after the Early Eocene continental break-up (e.g., Bukovics and Ziegler 1985; Færseth and Lien 2002). The NE-SW trend of the Vøring Basin is understood to come from the Caledonian suture system (Doré et al., 1997).

The crustal extension, due to the Upper Jurassic-Lower Cretaceous rift phase and later thermal subsidence, opened the deep Basin area (Møre and Træna Basin and Rås sub-Basin). In Lower Cretaceous, at the east of the Træna Basin and Rås Sub-basin, Nordland and Sklinna Ridges (see 1 in Figure 2.2) became topographic highs and were eroded, providing sediments that were deposited in the restricted basin (along Møre, Træna, Rås rift axis) (Fjellanger et al., 2005).

During the end of Lower Cretaceous and Upper Cretaceous, Jurassic faults were reactivated due to tectonic activity associated to a new extension (Upper Cretaceous-Paleocene rift). The basin increased the subsidence rate and the flanks were uplifted, producing tilting to the West in Trøndelag Platform and to the East in Gjalla Ridge (Brekke et al., 1999). Upper Cretaceous sediments were either deposited from Norway mainland or from East Greenland:

- In the East of the basin, due to the erosion of rejuvenated Nordland Ridge footwall, the Lange Fm. sandstones were deposited into the basin during Cenomanian and Turonian times. During the Turonian-Coniacian, the basin was totally filled and, therefore, the Lysing Fm. (thick deep-water fan) was deposited over Dønna Terrace and Halten Terrace area (2 in Figure 2.2) without any distribution restriction. The source of sediments was Nordland Ridge. Lysing Fm. is composed by turbidites,

debrites and heterolithic sandstones and mudstones, with good reservoir properties and more connected than Lower Cretaceous sediments (Fjellanger et al., 2005).

- The west part of the basin was controlled by Rym Fault Zone and Gjallar Ridge (3 in Figure 2.2). During Upper Cretaceous, Gjallar Ridge faults were active and Fenris Graben (3 in Figure 2.2) was developed to the west (Blystad et al., 1995). Hel Graben, Någrid Syncline and Vigrid Syncline (4 in Figure 2.2) subsided and extended.
    - Large and uniform basin-floor turbidite systems were deposited during the end of Upper Cretaceous: Nise Fm. in Campanian time and Springar Fm. in Maastrichtian time. A northeast Greenland provenance is suggested (Morton and Grant 1998), with Surt and Bivrost Lineaments controlling the sediment entry point position.
    - Some Basin areas were uplifted, faulted and eroded during Maastrichtian and Paleocene (Bukovics and Ziegler, 1985). Examples are Utgard High in the East, Nyk High in the center and Gjallar Ridge to the West (5 in Figure 2.2).

During Early Eocene, extension was finalized and the continental separation between Norway and East Greenland produced an intense volcanism, with the eruption of basaltic lavas that flowed through eroded areas (Brekke et al., 1999). This volcanism produced extrusive and intrusive magmatic rocks that make difficult seismic imaging in West and North-west margins of the basin.

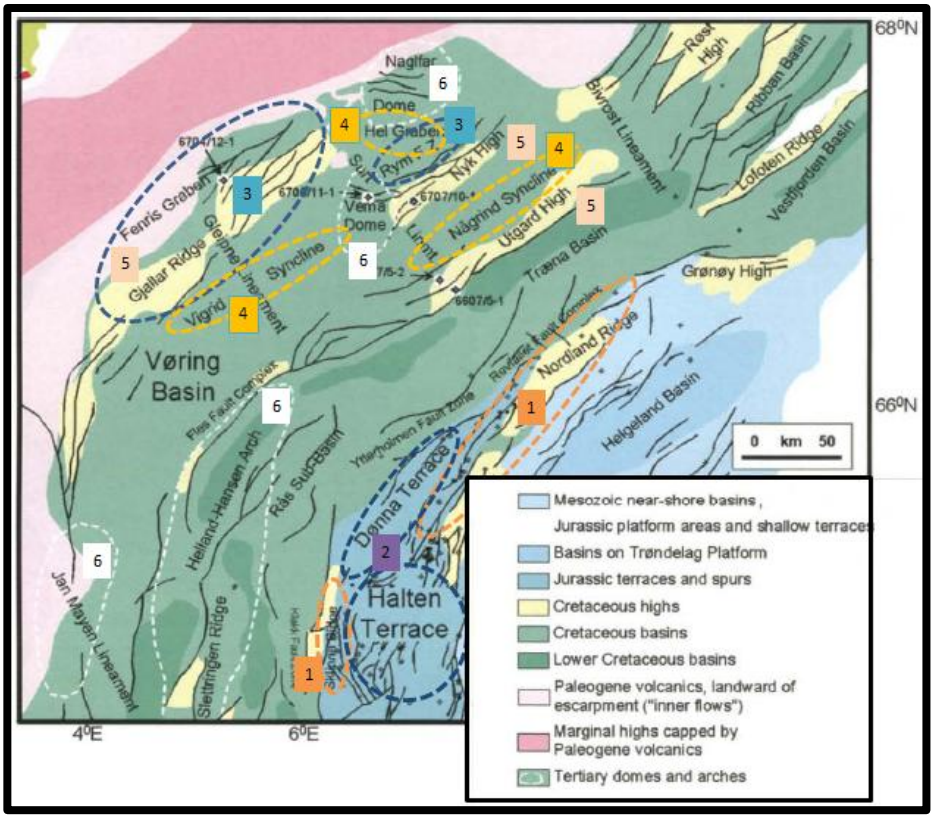

FIGURE 2. 1 - VØRING BASIN STRUCTURAL EVOLUTION. STRUCTURES REFERRED IN THE TEXT ARE NUMBERED. FIGURE MODIFIED AFTER FJELLANGER ET AL. (2005)

During post Early Eocene to Late Pliocene, due to the separation and plate reorganization, the horizontal stress pattern changed from Northwest-Southeast extension to Northwest-Southeast compression, resulting in the creation of tertiary domes and arches (Doré and Lundin 1996) (6 in Figure 2.2).

In Late Pliocene and Quaternary, eastern margin of the basin experienced a rapid subsidence as a consequence of the Norwegian mainland uplift, producing an acceleration of hydrocarbon generation and migration in Halten Terrace areas (Koch and Heum 1995) and deposition of large amount of sediments on the surrounding shelf (Brekke et al., 1999).

2.3 Stratigraphy description and depositional environment

2.3.1 Upper Cretaceous Formations

The Upper Cretaceous sandstones (Lysing Fm, Nise Fm and Springar Fm) (Figure 2.3), charged by a hypothetical Cretaceous source rock, and trapped along rotated fault blocks and Tertiary domes, represent one of the plays in Vøring and Møre Basins (Brekke et al., 1999). These reservoirs cover from slope to basin-floor fan deposits.

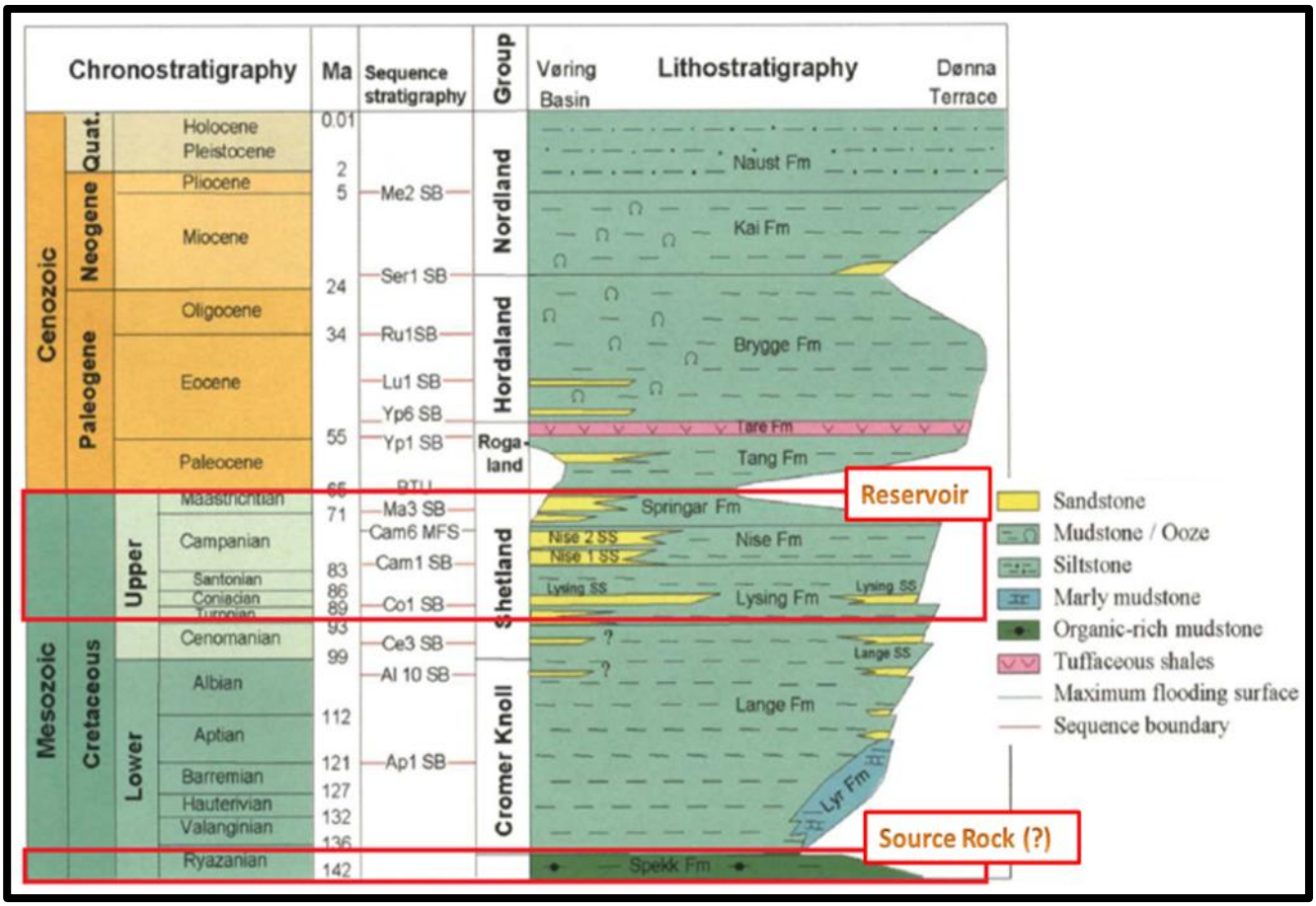

FIGURE 2. 2 - VØRING BASIN STRATIGRAPHY (CRETACEOUS-CENOZOIC). LYSING FM, NISE FM AND SPRINGAR FM ACT AS RESERVOIRS AND SPEKK FM AS POSSIBLE SOURCE ROCK. FIGURE MODIFIED AFTER FJELLANGER ET AL. (2005)

Lysing Fm.

The formation is present in Dønna Terrace and Halten Terrace, but not in Trøndelag Platform. The lithology is mainly fine to medium, occasionally coarse-grained, white-grey sandstones, partly carbonate-cemented and interbedded with shales (Dalland et al., 1988).

The depositional environment is interpreted as a fan system, composed by turbidites, debrites and heterolithic sandstones and mudstones. Cores from wells close to Gjallar ridge are interpreted as mid basin-floor fan, cores from Dønna Terrace as lower-slope basin-floor fan, and cores from Nordland ridge as a part of the upper-slope fan system (Fugelli and Olsen 2005).

Nise Fm.

The formation is present in the entire region, but is not in parts of the Nordland Ridge and on highs on the west of the Trøndelag Platform. The lithology consists mainly of grey and greyish-green claystones interbedded with carbonate and sandstone stringers (Dalland et al., 1988).

The depositional environment is interpreted as a fan complex (Figure 2.4). It was developed in Fenris and Hel Grabens, between Bivrost Lineament (North-east) and Gleipne Lineament (South-west). The deposits thicken towards the basin along the Surt Lineament and they reach the maximum thickness (approx. 900 m) at Nyk and Vema areas. The fan complex shales out to the Utgard High and the Fles Fault zone. (Fjellanger et al., 2005).

- Cores in Nyk High are sheet sediments in a mid-fan position, with massive, stacked, normally graded sandstones deposited by turbidity flows with intervals of bioturbated mudstones deposited during periods of fan abandonment (Fjellanger et al., 2005).
- Cores in Vema Dome are similar to cores in Nyk High, but with higher degree of amalgamation, meaning that it was in a mid-fan position, but closer to a channel (Fjellanger et al., 2005).
- Cores in Utgard High are heterolithic sandstones, with massive sandstones at the top, representing a Basin-fan far from the provenance area (Fjellanger et al., 2005).

Delfin Fm.

The Delfin Fm. is present in several wells in the northern Vøring Basin. It is Early Campanian and Late Santonian in age and is formed by basin floor fan sandstones intercalated between Nise Fm. shales. Thicknesses can reach up to more than 1000 meters of good quality sandstones (NPD factpages).

Springar Fm.

The Springar Fm. is widespread in the area, but not present on parts of the Nordland Ridge. The lithology is mainly greyish-green claystones interbedded with stringers of carbonates and sandstones (Dalland et al., 1988).

Sediments were probably channelled by valleys between Nyk High and Gjallar ridge into the basin. The depositional environment is interpreted as a fan system, with the depocenter in the middle of Vøring Basin. Cores from wells in Gjallar Ridge area shows beds of normally graded sandstones with few mud interbeds deposited by density to turbidity flows. Their composition is very uniform and they are interpreted to be located in mid-to-outer fan (Fjellanger et al., 2005).

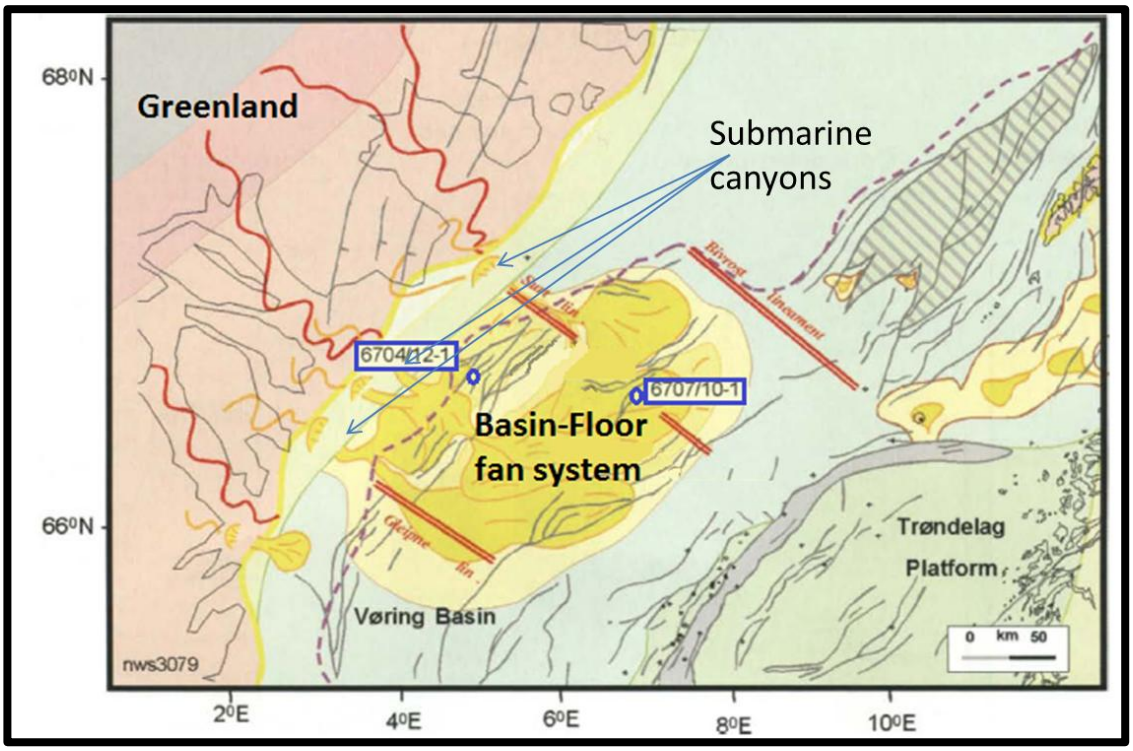

FIGURE 2. 3 - CAMPANIAN PALEOGEOGRAPHY OF THE VØRING BASIN SHOWING A BASIN-FLOOR FAN SYSTEM DEPOSITED IN THE DEEP BASIN THROUGH SUBMARINE CANYONS. GREENLAND CONTINENTAL SHELF. AFTER FJELLANGER ET AL. (2005).

Chapter 3: AVO-AVA forward modelling

3.1 Theoretical framework

AVO-AVA is a technique that analyses the variations of amplitudes as a function of offset or incident angle in NMO-corrected CMP gathers along the reflector in order to extract rock properties. Ostrander (1984) showed indeed that amplitude varies with offset for hydrocarbon-saturated sandstones and, since then, AVO has become a common technique in hydrocarbon exploration. More recent works (e.g., Mavko et al., 1998; Avseth et al., 2005) proposed guidelines to use this technique in an effective manner.

Appendix B gives a detailed theoretical framework for AVO-AVA forward modelling, including Zoeppritz (1919) equations and some linearized approximations, 1-D convolutional trace model, Gassmann (1951) theory, some effective medium models and AVO classification based on Rutherford and William (1989).

In the AVO-AVA forward modelling, the amplitudes are calculated using the full Zoeppritz equation and synthetic traces (NMO-corrected CMP gathers) are generated for angles from 0° to 50°. This modelling approach assumes horizontal layers without lateral velocity variations. Such AVO-AVA modelling is applied here for each of the four case studies. Different fluid saturation scenarios are modelled by using Gassmann theory.

3.2 Methodology

3.2.1 Data Preparation

The main input log curves used for AVO-AVA modelling are upscaled density, V_p and V_s. Some preliminary work must be done on these curves before using them:

- Correct density log from erratic measurements during logging.
- Generate V_s curves from V_p curves in wells where it is not available.
- Upscale logs.

In addition, some values, such as porosity or matrix density, must be calculated in target intervals. In order to do it, volume of shale is first estimated from Gamma ray logs.

Finally, a calibration or ‘tie’ between seismic data (in time) and well data (in depth) must be done to correlate seismic events with elastic properties measured in the well. This is performed in two steps:

- Check-shot correction.
- Wavelet extraction and well tie.

Logs Editing and QC

Bulk density logs were corrected in areas where caliper showed large deviations and anomalously low values of density (see areas in the ellipse in Figure 3.1). The reason is that those measurements correspond to mud density, not to the formation.

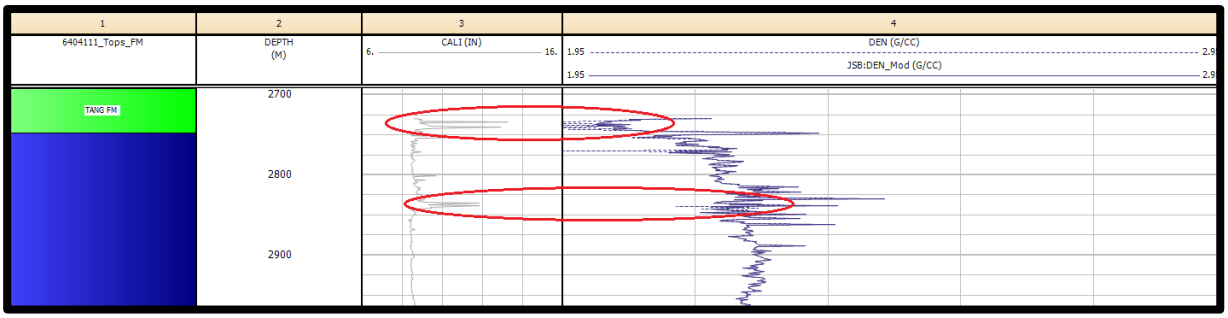

FIGURE 3. 1 - DENSITY CORRECTION IN WELL 6404/11-1

V_p and V_s were directly calculated from compressional sonic (DTC) and shear sonic logs (DTS) from equations (3.1) and (3.2):

$$Vp(m/s) = \frac{10^6}{DTC(\mu s/ft)} 0.3048 \quad (3.1)$$

$$Vs(m/s) = \frac{10^6}{DTS(\mu s/ft)} 0.3048 \quad (3.2)$$

Shear-velocity estimation

Shear sonic information was not available for the Springar Fm. in well 6403/10-1 (Solsikke) and in the whole depth range of well 6404/11-1. For this reason, V_s was estimated as follow:

- V_s was computed from V_p for the Springar Fm. in well 6403/10-1 (Solsikke) by using the Greenberg-Castagna (1992) (Equation 3.3) empirical relation for shale, as this well mainly corresponds to shale according to Gamma ray logs (Figure 3.14). Note that V_p and V_s must be measured in km/s in this equation.

$$Vs = 0.76969\, Vp - 0.86735 \quad (3.3)$$

- The corresponding output curve is compared with the real curve in areas where it was available (Figure 3.2). As they matched in the ellipse (Figure 3.2), a new curve was created by merging the original log below the top of the Nise Fm. and using the Greenberg-Castagna (Equation 3.3) derived curve in the Springar Fm.
- Then, a linear regression in V_p/V_s plots was computed for the Springar Fm. and the Nise Fm. in well 6403/10-1 (Solsikke) to see the general V_p/V_s trend in the area (Figure 3.3).
- V_s was computed from V_p in well 6404/11-1 by using two methods:
    - Linear regression for V_p/V_s relation computed in well 6403/10-1 (Figure 3.3).
    - Greenberg-Castagna (1992) empirical relation for shale (Equation 3.3).

- And, then, they were compared (Figure 3.4). Based on their observed similarity, the Greenberg-Castagna approximation was used to calculate V_s for well 6404/11-1.

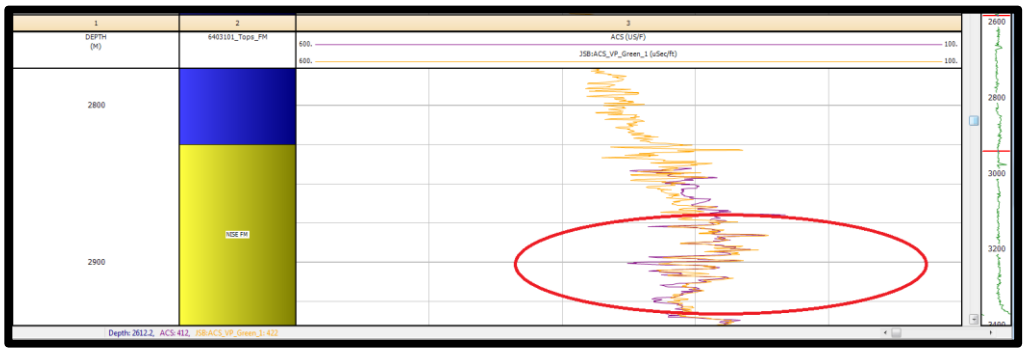

FIGURE 3. 2 - GREENBERG-CASTAGNA DERIVED CURVE (ORANGE) AND REAL DATA (PURPLE). THEY MATCH IN THE ELLIPSE.

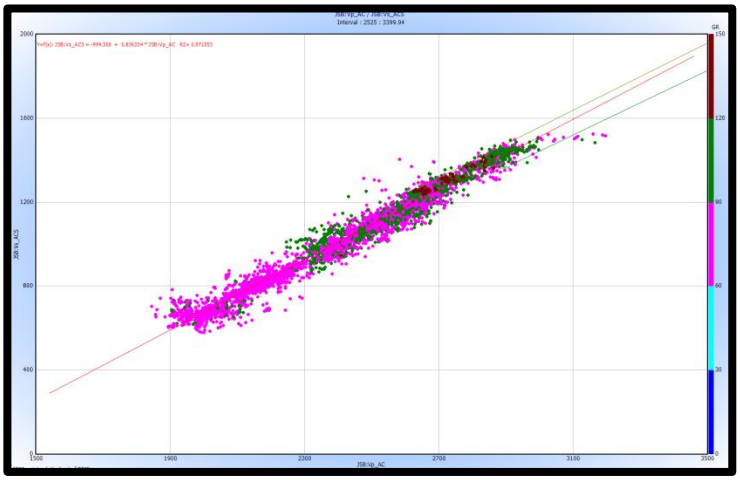

FIGURE 3. 3 - VP/VS CROSSPLOT FOR WELL 6403/10-1. LINEAR REGRESSION IS COMPUTED AND DISPLAYED FOR THE SPRINGER FM. AND THE NISE FM.

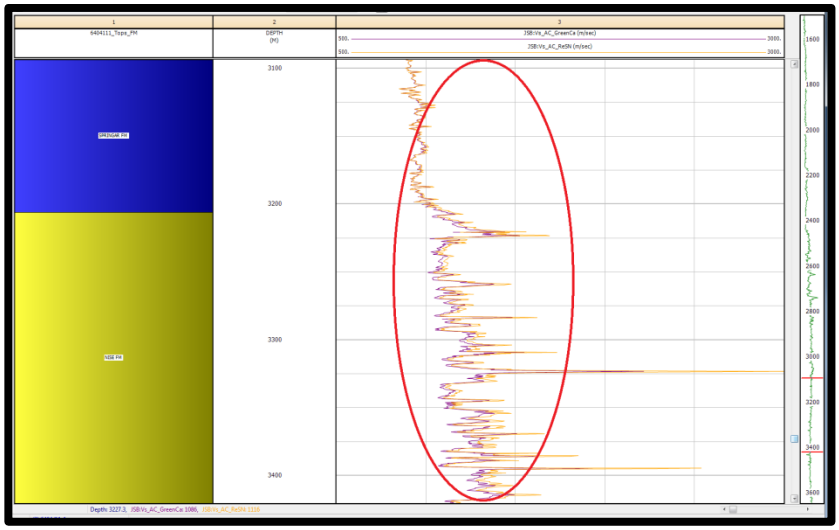

FIGURE 3. 4 - V_S CALCULATION FOR WELL 6404/11-1. NOTE HOW REGRESSION (ORANGE) AND GREENBERG-CASTAGNA (PURPLE) DERIVATIONS FIT IN SPRINGAR FM. AND NISE FM

Volume of shale (Vshale) estimation

The total volumetric shale (V_{sh}) is calculated from the Gamma Ray (GR) log by using the equation:

$$V_{sh} = \frac{GR_{log} - GR_{min}}{GR_{max} - GR_{min}} \quad (3.4)$$

where GR_{min} corresponds to the minimum value in the formation (more sandy areas) and GR_{max} corresponds to the maximum value in the formation (more shaly areas).

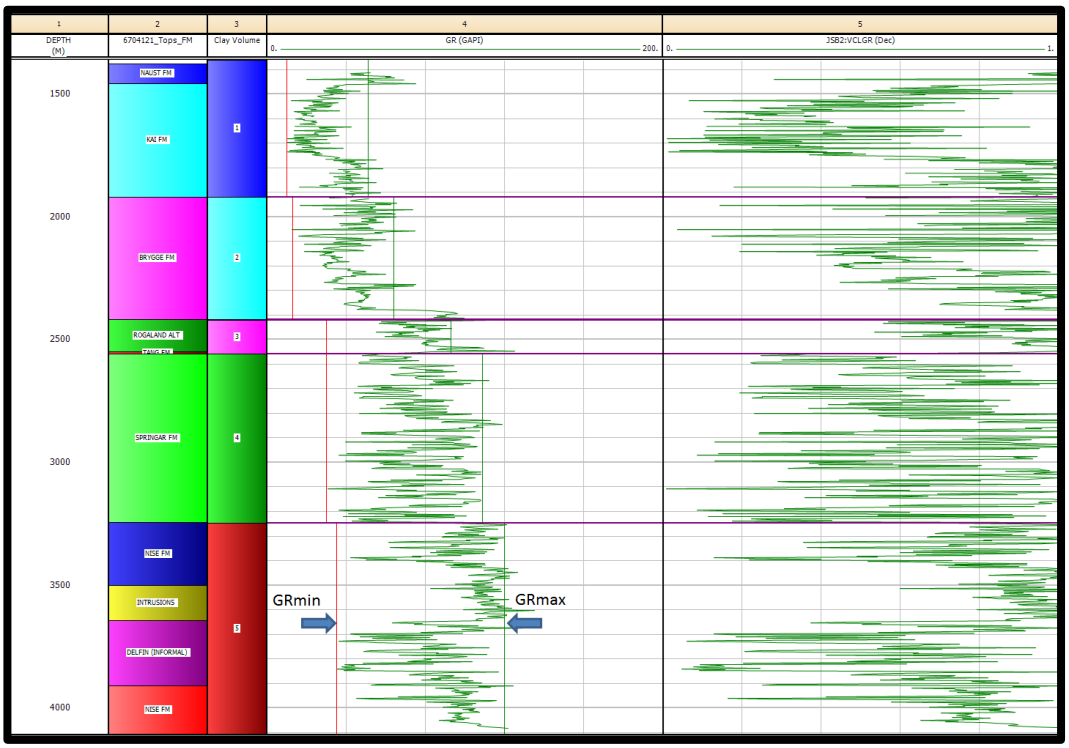

FIGURE 3. 5 - GJALLAR RIDGE WELL (6704/12-1) VSH ESTIMATION. GR LOG IS DIVIDED INTO ZONES BASED ON FORMATIONS. FOR EACH ZONE, GR_{MAX} AND GR_{MIN} ARE DEFINED AND V_{SH} IS COMPUTED.

Check-shot correction

Sonic log data (high-frequency, KHz) measures with a resolution of centimetres and seismic data (lower frequency, Hz) with a resolution of a few tens of meters. Sonic log is also dependent on the borehole conditions and it can only measure tens of centimetres into the formation, which might not be accurate for the estimation of interval velocity of the whole formation.

The check shot is a borehole seismic data survey designed to measure the seismic traveltime from the surface to a given depth. With check-shot correction (Figure 3.6), sonic log is calibrated, i.e., the time-depth curve from the sonic log (and the sonic log/P-wave velocities) will match the time-depth relationship derived from seismic data after check-shot correction. The process is as follow:

- From sonic/ V_p log, time is computed for specific depths.

$$t_{li} = \frac{z_{li}}{V_{li}} \qquad (3.5)$$

Where t_{li}, z_{li} and V_{li} are time, depth and log velocity at position i.

- Time-depth pairs (t_{ci}, z_{li}) are recorded at the same position from the check shot (seismic frequency).
- The difference $\mathbf{\Delta t = t_{li} - t_{ci}}$ is used to correct sonic and time-depth well logs.

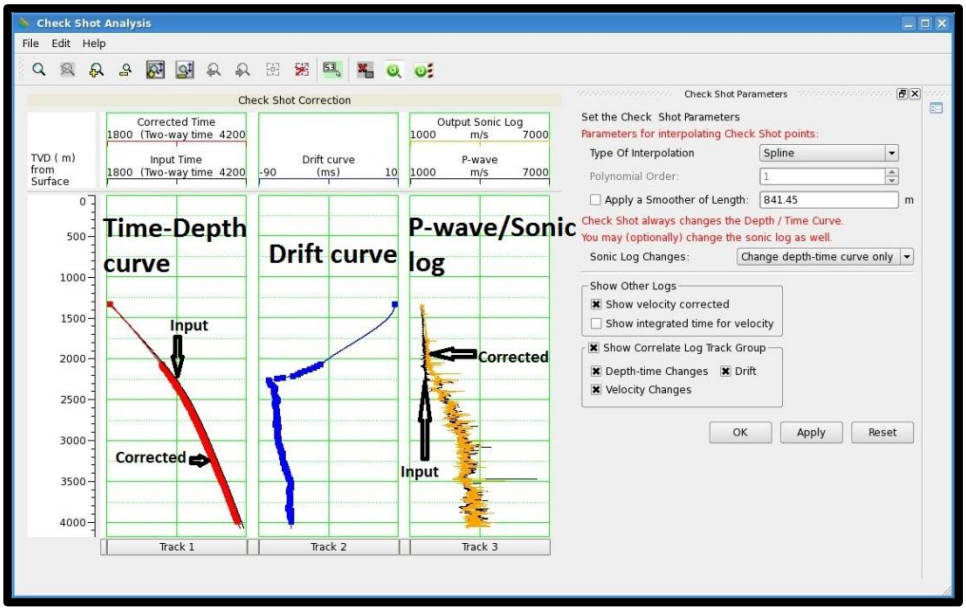

FIGURE 3. 6 - GJALLAR RIDGE WELL (6704/12-1) CHECK-SHOT CORRECTION. DRIFT CURVE (CENTRE) IS INTERPOLATED TO SHOW THE DIFFERENCE BETWEEN THE TIME-DEPTH CURVE LOG AND CHECK-SHOT DATA. TIME-DEPTH CURVE (LEFT) AND SONIC/ V_P (RIGHT) LOGS ARE CORRECTED USING THE DRIFT CURVE.

Wavelet extraction and well correlation

The wavelet extraction method (Figure 3.7) uses well information and seismic data close to that well. First, acoustic impedances are calculated from sonic and density logs and, then, reflectivity is derived from acoustic impedances. The wavelet is extracted by finding the operator which, convolved with the reflectivity, produces an output similar to the neighbouring seismic traces. A constant-phase method (Figure 3.7a) is selected because the Full-wavelet and Roy-White algorithm require high correlation between well logs and seismic data (Hampson-Russell manual).

Well correlation (Figure 3.8) is used to improve the match between the well log time-depths and the measured P-wave seismic times. Synthetic traces derived from well log are shifted and manually stretched until they match seismic (i.e., they are well correlated). In this study and at that location, a correlation above 0.6 is considered good. However, in well 6404/11-1 (Møre Basin) located at around 350 m from the line, a correlation of 0.5 is considered acceptable due to the distance between the well and the seismic line. Well correlations and extracted wavelets for the four lines/wells are available in appendix C.

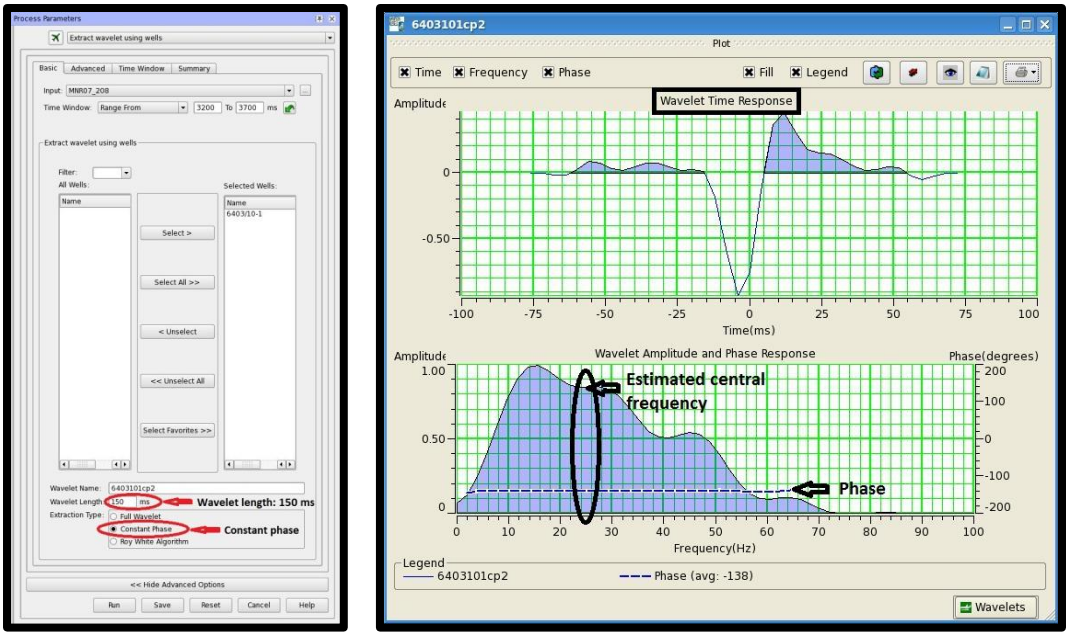

(A) (B)

FIGURE 3. 7 - WAVELET EXTRACTED FROM SOLSIKKE WELL (6403/10-1) AND SEISMIC LINE MNR07-208. (3.7A) WAVELET LENGTH IS 150 MS AND A CONSTANT-PHASE METHOD IS SELECTED. (3.7B) EXTRACTED WAVELET WITH A DOMINANT FREQUENCY AROUND 25 HZ.

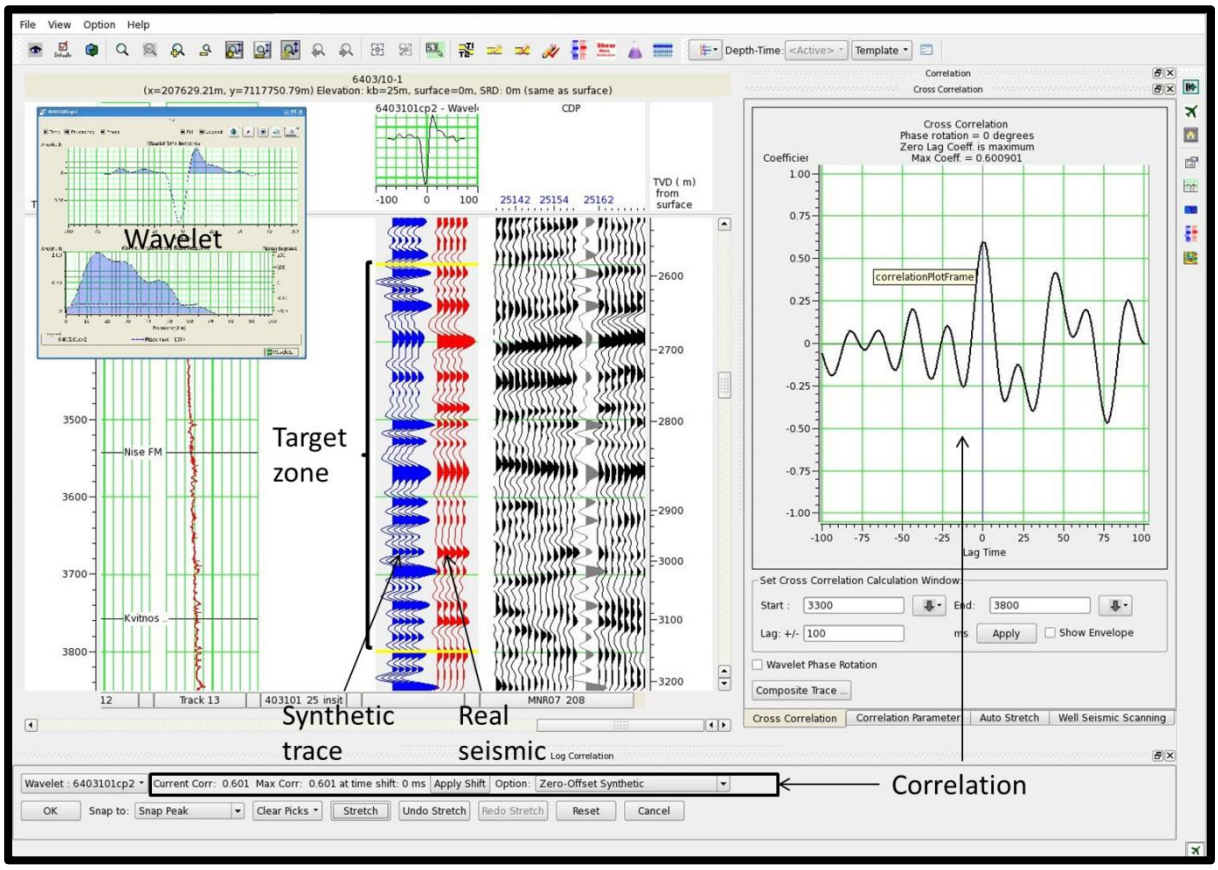

FIGURE 3. 8 - WELL CORRELATION FOR SOLSIKKE WELL (6403) AND SEISMIC LINE MNR07-208 SHOWING A CORRELATION OF 0.6 IN THE TARGET ZONE.

Upscaling

Since high-frequency (KHz) log data measures with a resolution of centimetres and lower frequency seismic data (Hz) with a resolution of up to a few tens of meters, upscaling is needed to match both. The Backus average (Backus, 1962) is used for this purpose. In this method, elastic properties (bulk and shear modulus) are calculated from densities, V_p and V_s of stacked thin layers. Then, these modulus and densities are averaged (blocked) over large intervals according to the seismic resolution and, finally, the velocities of these intervals are computed from these averages.

As the seismic vertical resolution is given by the tuning thickness, a good way to estimate an appropriate block size is the calculation of this thickness. An approximation of the tuning thickness in the Nise Fm. can be derived from the average V_p in the target zone and the dominant frequency (f_0) of the wavelets extracted for each well. Based on Table 3.1, a block size of 25 m is defined for upscaling in wells 6403/10-1 (Solsikke) and 6707/10-1 (Luva discovery), 26 m for 6404/11-1 and 51 m for well 6704/12-1 (Gjallar Ridge).

$$\text{Tuning thickness} = \frac{\lambda}{4} = \frac{V_p}{4f_0} \tag{3. 6}$$

TABLE 3. 1 – UPSCALLING BLOCK SIZES BASED ON TUNING THICKNESS.

Well name	Vp average (m/s)	f_0 (Hz)	Tuning thickness (m)
Solsikke (6403/10-1)	2500	25	25
6404/11-1	2700	26	26
Gjallar Ridge (6704/12-1)	3700	18	51
Luva discovery (6707/10-1)	2800	28	25

3.2.2 AVO-AVA Modelling

AVO-AVA forward models are produced to determine the relationship between elastic rock properties and AVO-AVA seismic responses. The result is then compared qualitatively with the variation in amplitude with incident angle observed in partial-stack data (Appendix A).

- The two wells in Vøring Basin found gas in the Nise Fm. sandstones with very different saturations: Luva discovery well (6707/10-1) was a gas discovery with gas saturations around 90%, while Gjallar Ridge well (6704/12-1) found only residual gas (10% saturation). Therefore, both wells have been used to investigate the effect of various gas saturations in AVO-AVA response. Fluid Replacement Modelling is used to evaluate different scenarios.

- The two wells in Møre Basin, Solsikke (6403/10-1) and 6404/11-1, were dry, so the investigation focuses here on the effect of the lithology in the AVO-AVA response.

Target zone intervals are located in the Nise Fm. for Møre Basin wells, and the Delfin Fm. (sandstones in Nise Fm.) in Vøring Basin wells. The depths for the intervals are presented in Table 3.2.

TABLE 3. 2 – DEPTH INTERVALS FOR TARGET FORMATIONS (NISE FM. IN MØRE BASIN AND DELFIN FM. IN VØRING BASIN)

Well name	Start	End
Solsikke (6403/10-1)	2825 m	3098 m
6404/11-1	3181 m	3600 m
Gjallar Ridge (6704/12-1)	3619 m	3885 m
Luva discovery (6707/10-1)	2952 m	3100 m

The properties within the target zone are:

Matrix properties:

- Mineral composition: Clay and Quartz.
- The content of clay is determined by the volumetric shale (V_{sh}) (previously derived).
- The content of Quartz is 100 – V_{sh}, where V_{sh} is expressed in percentage.
- The mineral elastic properties are given in Table 3.3:

TABLE 3. 3 – QUARTZ AND CLAY DENSITY (Ρ), BULK (K) AND SHEAR (Μ) MODULUS

Mineral	ρ (g/cc)	K (GPa)	μ(GPa)
Quartz	2.65	36.6	45
Clay	2.58	20.9	6.9

- The density is computed from:

$$\rho_{matrix} = V_{sh}\rho_{clay} + (1 - V_{sh})\rho_{quartz} \quad (3.7)$$

- The bulk and shear modulus are calculated using the Hashin-Shtrikman (1963) average (Table B.1 in Appendix B).

Fluid properties:

- The density is computed from:

$$\rho_{fluid} = S_{brine}\rho_{brine} + S_{oil}\rho_{oil} + S_{gas}\rho_{gas} \quad (3.8)$$

where S_i is the saturation of element i.

- The fluid elastic properties in Table 3.4 are based on Batzle and Wang (1992):

TABLE 3. 4 - BRINE AND GAS DENSITY (P) AND BULK (K) MODULUS

Fluid Type	ρ (g/cc)	K (GPa)
Brine	1.09	2.38
Gas	0.10	0.02

- Fully and homogeneous pore saturation is assumed and, hence, Wood (1955) or Reuss (1929) average (Table B.1 in Appendix B) is used to calculate the bulk modulus of the fluid mixture.

The porosity is derived from the density log and density of the matrix:

$$\Phi = \frac{\rho_{matrix} - \rho_{log}}{\rho_{matrix} - \rho_{fluid}} \quad (3.9)$$

The effective bulk for different gas saturations in Vøring Basin are calculated with the Gassmann (1951) equations (Equations B.27 in Appendix B) from in-situ conditions.

In all the wells, synthetic traces for the different scenarios are generated using a Ricker wavelet and applying Zoeppritz equations (Zoeppritz, 1919). The average frequency of the Ricker wavelet is the same as the dominant frequency of the extracted wavelet. Geometrical spreading and transmission-loss effects are not considered in the model. The incident angle ranges from 0° to 50°.

Synthetic traces are NMO-corrected CMP gathers displayed in normal polarity convention, i.e., on zero-phase seismic data an increase in acoustic impedance is a peak, whereas a trough is a decrease in acoustic impedance.

3.3 Results

3.3.1 Vøring Basin cases

Gas-saturated sand case- Luva discovery (6707/10-1)

Luva discovery (6707/10-1) is a gas discovery in the upper Delfin Fm. sandstones (sandstones within the Nise Fm.) with 90% gas saturation (in-situ saturation). Different gas saturations are used to study their effect in the AVO-AVA response. Pure brine, 90% gas-10% brine (in-situ case), 70% gas-30% brine and 50% gas-50% brine cases are modelled. Wiggled traces are generated by blocking logs in sizes of 25 meters and for incident angles between 0° and 50°. In Figure 3.9, Delfin Fm. sandstones can be identified by their low values in Gamma Ray log and the presence of gas is observed in the highlighted area by the

large resistivity log measurement. V_p, V_s, density and Poisson's ratio for each of saturation scenario together with wiggled traces are displayed in Figure 3.10.

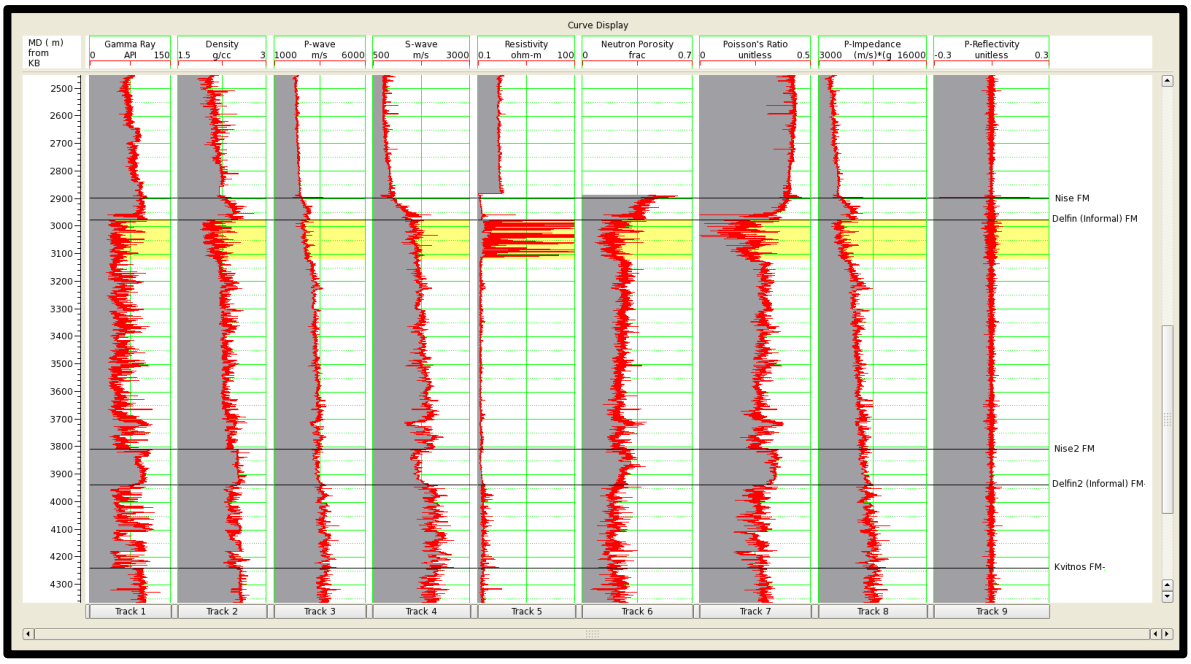

FIGURE 3. 9 - GAMMA RAY, DENSITY, V_P, V_S, RESISTIVITY AND NEUTRON POROSITY FROM LUVA DISCOVERY WELL (6707/10-1) COMPOSITE LOG. POISSON'S RATIO, P-IMPEDANCE AND P-REFLECTIVITY ARE CALCULATED. AREA OF INTEREST BETWEEN THE DELFIN (INFORMAL) FM. TOP AND BASE OF THE RESERVOIR IS HIGHLIGHTED.

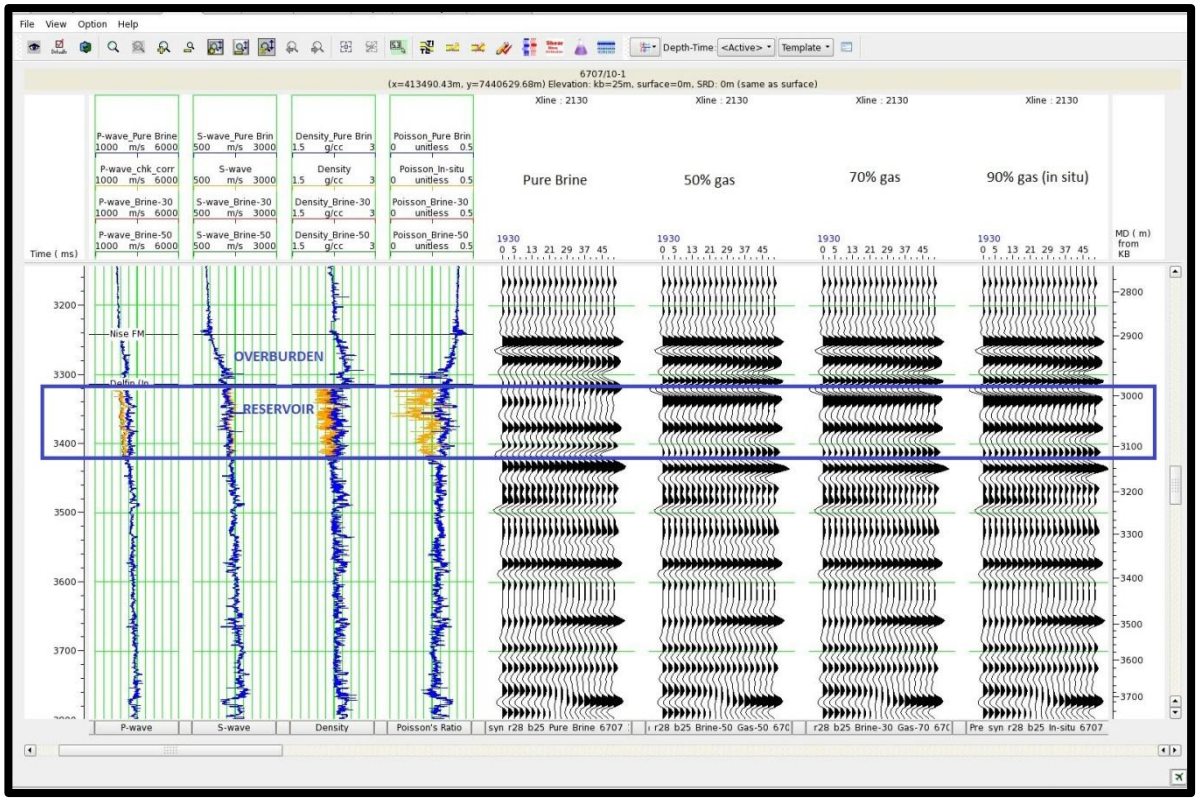

FIGURE 3. 10 - ELASTIC PROPERTIES (V_P, V_S, DENSITY AND POISSON'S RATIO) FROM LUVA DISCOVERY WELL (6707/10-1) DISPLAYED TOGETHER WITH WIGGLED TRACES FOR PURE BRINE , 90% GAS-10% BRINE (IN-SITU FLUID SATURATION), 70% GAS-30% BRINE, AND 50% GAS-50% BRINE SCENARIOS

The effective elastic properties of the reservoir for the different scenarios (Figure 3.10), together with those of the overburden layer, are listed in Table 3.5. This information is based on 25-m blocks. In addition, variations in percentage of elastic properties for different gas saturations compared with the pure brine case are shown in Table 3.6.

TABLE 3. 5 – V_P, V_S, DENSITY AND POISSON'S RATIO IN OVERBURDEN LAYER AND IN RESERVOIR FOR DIFFERENT PORE SATURATIONS (LUVA DISCOVERY)

Model	Vp (m/s)	Vs (m/s)	ρ (g/cm3)	Poisson's Ratio
Overburden layer	2808	1443	2.445	0.305
Pure Brine	2977	1482	2.324	0.332
Gas 90% (in situ)	2613	1544	2.146	0.234
Gas 70%	2634	1529	2.186	0.235
Gas 50%	2658	1516	2.223	0.236

TABLE 3. 6 - V_P, V_S, DENSITY AND POISSON'S RATIO PERCENTAGE VARIATION FOR THE MODELLED GAS SATURATIONS WITH RESPECT TO THE BRINE CASE (LUVA DISCOVERY)

Gas (%)	%ΔVp	%ΔVs	%Δρ (g/cm3)	%ΔPoisson's Ratio
90 (in situ)	-12.2	4.1	-7.7	-29.5
70	-11.5	3.2	-5.9	-29.2
50	-10.7	2.3	-4.3	-28.9

Based on tables 3.5 and 3.6, the increment of gas saturation reduces the value of V_p (-12.2%) in the reservoir. It also reduces density, but in a lesser extent, whereas V_s slightly increases. The consequence of all these changes is a dramatic drop of Poisson's value (29%). When the 90% gas saturation case is compared with the 70% and 50% gas saturation ones, the changes in elastic properties are very small.

To show the effects in seismic response of changes in elastic parameters due to different gas saturations, the variation of amplitude with incident angle for each model is plotted in Figure 3.11. In this figure, the zero-offset reflection coefficient (amplitude) is, in absolute value, much lower in pure brine case than in all gas-saturated cases. This effect is due to the decrease of V_p and density in the gas-saturated reservoir, which produces an increment in the contrast between reservoir and overburden impedances. Note also how the amplitude is becoming more positive with incident angle in the pure-brine scenario (with a change in polarity) and becoming more negative in the gas-saturated scenarios. The reason, as it will be discussed later, is the difference between Poisson´s ratio in reservoir and overburden. Figure

3.11 also shows that for gas saturations higher than 50%, the variation in amplitude with angle is almost the same regardless of the gas saturation. This demonstrates that AVO-AVA response is insensible to the increment of gas for gas saturations higher than 50% and it is in accordance with the slight variation of Poisson´s ratio in all those cases (Table 3.6).

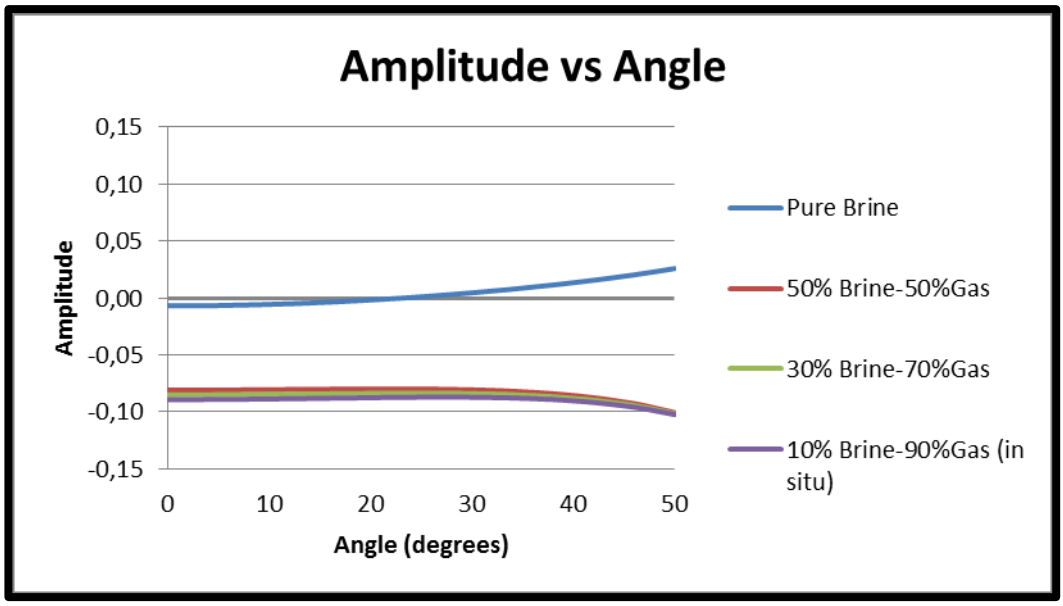

FIGURE 3. 11 - ELASTIC PROPERTIES (V_P, V_S, DENSITY AND POISSON'S RATIO) FROM LUVA DISCOVERY WELL (6707/10-1) DISPLAYED TOGETHER WITH WIGGLED TRACES FOR PURE BRINE , 90% GAS-10% BRINE (IN-SITU FLUID SATURATION), 70% GAS-30% BRINE, AND 50% GAS-50% BRINE SCENARIOS

Marginally gas saturated sand case - Gjallar Ridge (6704/12-1)

Gjallar Ridge well (6704/12-1) is a dry well with residual gas and the Delfin Fm. represents the potential reservoir. The AVA response for low-gas saturations is studied at the top of the cleaner sand interval which is marked in blue in Figure 3.12 and Figure 3.13. The scenarios modelled are pure brine, 5% gas-95% brine, 10% gas-90% brine (in-situ fluid saturation), and 20% gas-80% brine. Wiggled traces are generated by blocking logs in sizes of 51 m and for incident angles between 0° and 50°. In Figure 3.12, Delfin Fm. sandstones can be identified by their relative low values in Gamma Ray log and the presence of marginal gas is perceived in the highlighted area by the slight increment in resistivity log measurement. V_p, V_s, density and Poisson's ratio for each of saturation scenario together with wiggled traces are displayed in Figure 3.13. The target reflector is marked in red.

The effective elastic properties for different gas saturation scenarios in the selected clean-sand interval and those of the layer above are listed in Table 3.7. In addition, variations in percentage of elastic properties for different gas saturations compared with the pure brine case are shown in Table 3.8.

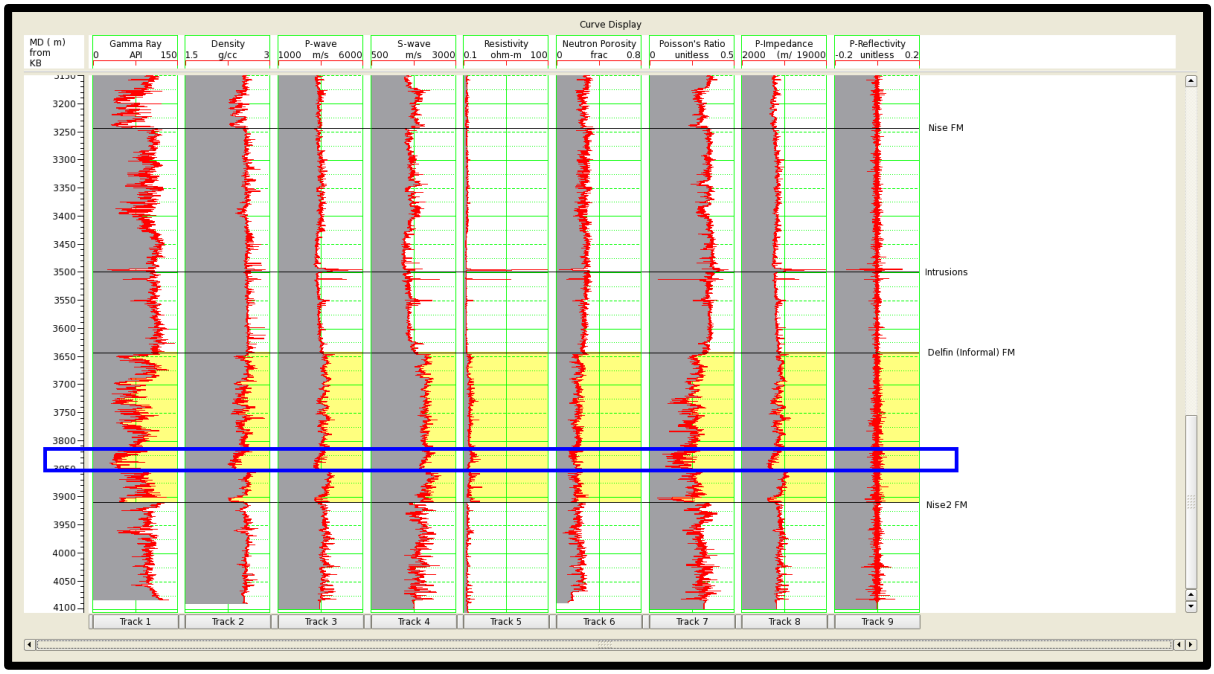

FIGURE 3. 12 - GAMMA RAY, DENSITY, V_P, V_S, RESISTIVITY AND NEUTRON POROSITY FROM GJALLAR RIDGE WELL (6704/12-1) COMPOSITE LOG. POISSON'S RATIO, P-IMPEDANCE AND P-REFLECTIVITY ARE CALCULATED. AREA OF INTEREST BETWEEN DELFIN (INFORMAL) FM TOP AND NISE 2 FM 2 IS HIGHLIGHTED.

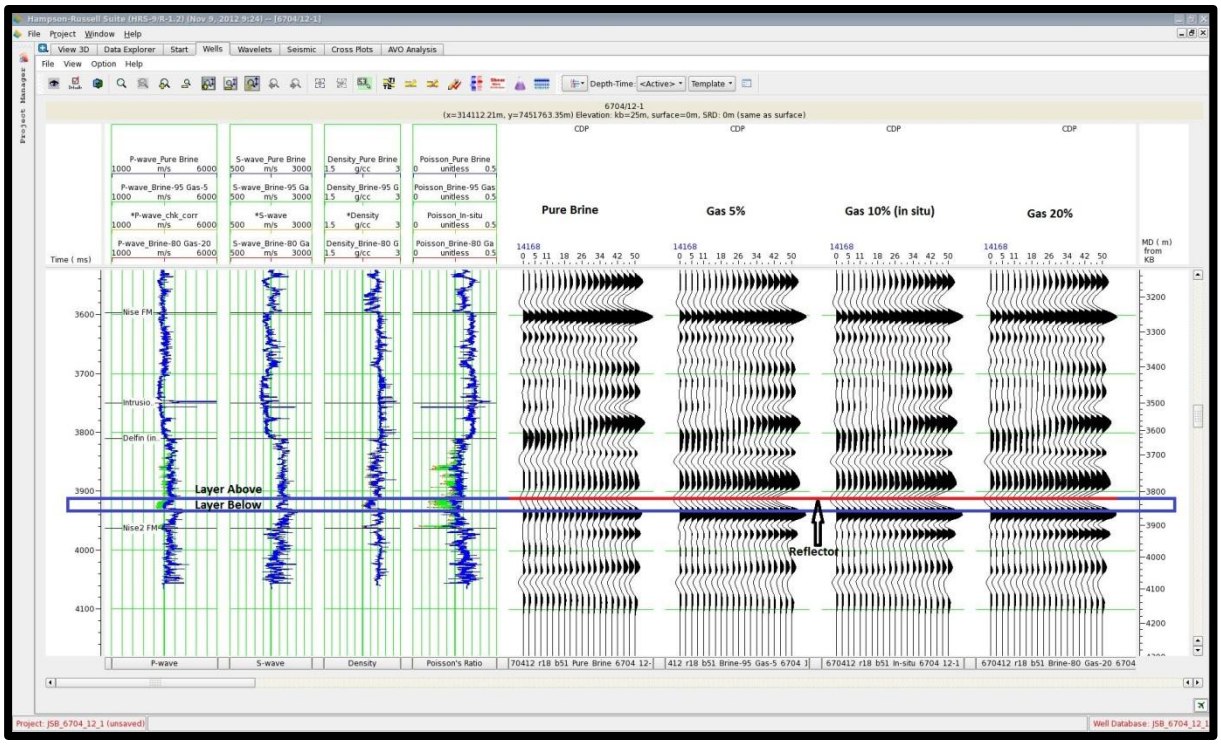

FIGURE 3. 13 - ELASTIC PROPERTIES (V_P, V_S, DENSITY AND POISSON'S RATIO) FROM GJALLAR RIDGE WELL (6704/12-1) DISPLAYED TOGETHER WITH WIGGLED TRACES FOR PURE BRINE , 5% GAS-95% BRINE, 10% GAS-90% BRINE (IN-SITU FLUID SATURATION) AND 20% GAS-80% BRINE SCENARIOS.

TABLE 3. 7 - V_P, V_S, DENSITY AND POISSON'S RATIO IN OVERBURDEN LAYER AND IN RESERVOIR FOR DIFFERENT PORE SATURATIONS (GJALLAR RIDGE)

Model	Vp (m/s)	Vs (m/s)	ρ (g/cm3)	Poisson's Ratio
Layer above	3740	2101	2.542	0.267
Pure Brine	3735	2111	2.480	0.264
Gas 5%	3558	2112	2.474	0.220
Gas 10% (in situ)	3535	2115	2.470	0.216
Gas 20%	3532	2119	2.459	0.212

TABLE 3. 8 - V_P, V_S, DENSITY AND POISSON'S RATIO PERCENTAGE VARIATION FOR THE MODELLED GAS SATURATIONS WITH RESPECT TO THE BRINE CASE (GJALLAR RIDGE)

Gas (%)	%ΔVp (m/s)	%ΔVs (m/s)	%Δρ (g/cm3)	%ΔPoisson's Ratio
5	-4.7	0.07	-0.24	-16.7
10 (in situ)	-5.3	0.20	-0.4	-18.2
20	-5.4	0.42	-0.8	-19.7

In Table 3.8, note how the effect of residual gas (5%) reduces the value of V_p (-4.7%) whereas V_s and density hardly change. This illustrates the insensitivity of V_s to pore fluid. The overall consequence is a dramatic drop of Poisson's value (17%). When the gas saturation is increased to 10% or 20%, the changes in elastic properties are more limited.

To show the effects in seismic response of changes in elastic parameters due to low-gas saturations, the variation of amplitude with incident angle for each model is plotted in Figure 3.14.

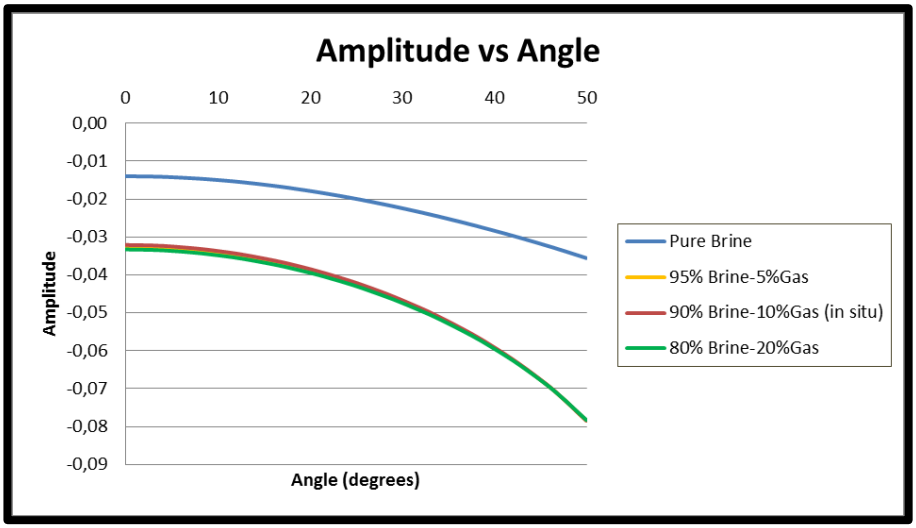

FIGURE 3. 14 - AMPLITUDE VS INCIDENT-ANGLE IN GJALLAR RIDGE WELL (6704/12-1) FOR PURE BRINE, 10% GAS-90% BRINE (IN-SITU FLUID SATURATION), 20% GAS-80% BRINE, AND 30% GAS-70% BRINE SCENARIOS.

In Figure 3.14, the zero-offset reflection coefficient (amplitude) is, in absolute value, lower in pure-brine case than in all gas-saturated cases. This difference is due to the drop of V_p and density with residual gas, which produces a decrease in the impedance of the layer and,

hence, an increment in the contrast between the impedance of the layers above and below the reflector. Note also how the amplitude decreases (increases the absolute value) more rapidly in gas-saturated scenarios than in pure-brine scenario. The reason is the lower Poisson´s ratio value in the reservoir and the overburden. In addition, the variation in amplitude with angle is very similar regardless of the gas saturation. This demonstrates that AVO-AVA response is insensible to the increase of gas saturation when it is higher than 10% (moreover, in this case, the 5% gas saturation case also shows similar response).

3.3.2 Møre Basin cases

Non-hydrocarbon flat event case - Solsikke (6403/10-1)

Based on NPD factpages, Solsikke well (6403/10-1) was drilled to test the hydrocarbon potential over a flat seismic event in the top the Nise Fm. (Appendix D). The result was a dry well with neither sand reservoir nor gas saturation. This is seen in Figure 3.15, where the Nise Fm. (highlighted) shows no sand interval in the Gamma Ray log and no presence of hydrocarbon in the resistivity log. In the available seismic data, the flat event was observed at 3560 ms. It is a positive amplitude that in partial stack data (Appendix A) shows a slight increment with angle.

The AVA response for pure brine saturation is modelled in the top of Nise Fm. in order to check whether this increment can be reproduced. For this purpose, wiggled traces are generated by blocking logs in sizes of 25 meters and for angles between 0° and 50°. V_p, V_s, density, acoustic impedance and Poisson's ratio for 25-m blocks, together with wiggled traces, are displayed in Figure 3.16, where an increase in amplitude with angle can be observed in the flat event (red line).

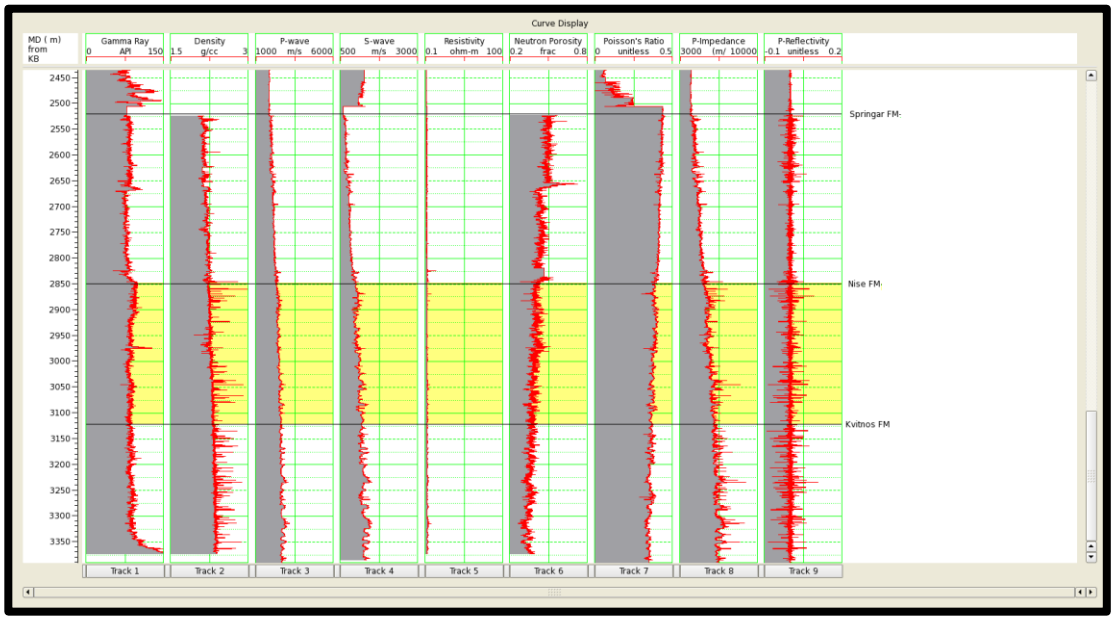

FIGURE 3. 15 - GAMMA RAY, DENSITY, V_P, V_S, RESISTIVITY AND NEUTRON POROSITY FROM SOLSIKKE WELL (6403/10-1) COMPOSITE LOG. POISSON'S RATIO, P-IMPEDANCE AND P-REFLECTIVITY ARE CALCULATED. AREA OF INTEREST BETWEEN NISE FM. TOP AND KVITNOS FM. TOP IS HIGHLIGHTED.

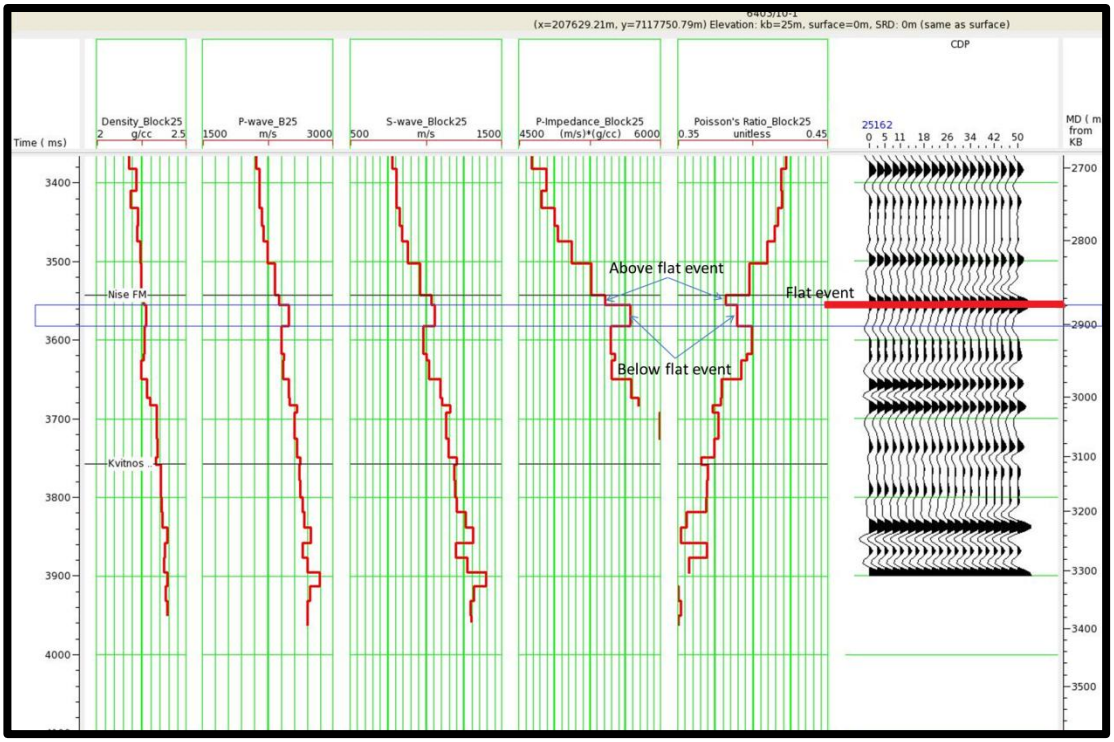

FIGURE 3. 16 - P-IMPEDANCE AND POISSON'S RATIO IN SOLSIKKE WELL (6403/10-1) ARE DISPLAYED FOR BLOCKING OF 25 METERS. SYNTHETIC SEISMIC TRACES FOR ANGLES BETWEEN 0 AND 50 ARE ALSO DISPLAYED FOR BLOCKING OF 25 METERS.

The Luva gas discovery well (6707/10-1 in Vøring Basin) has a flat event (Appendix D) at the base of the reservoir due to a fluid contact (gas-water contact; GWC), whereas the flat event observed in the Solsikke well (6403/10-1, no-discovery in Møre Basin) (Appendix D) is not associated with hydrocarbon accumulation. In order to compare the two cases, the effective elastic properties along the flat events (above and below) in both wells are evaluated in Table 3.9. This information is based on 25-m blocks. In addition, variations in elastic properties along the flat event are also calculated for both cases in Table 3.10.

TABLE 3. 9 - V_P, V_S, DENSITY AND POISSON'S RATIO ABOVE AND BELOW FLAT EVENTS OBSERVED AT THE RESERVOIR BASE OF LUVA GAS DISCOVERY WELL (6707/10-1) AND AT SOLSIKKE WELL (6403/10-1)

	Vp (m/s)	Vs (m/s)	ρ (g/cm3)	Poisson's Ratio
Solsikke (above flat event)	2387	1040	2.26	0.382
Solsikke (below flat event)	2494	1057	2.275	0.389
Luva gas discovery (above flat event)	2755	1646	2.17	0.234
Luva gas discovery (below flat event)	3042	1647	2.23	0.291

TABLE 3. 10 - V_P, V_S, DENSITY AND POISSON'S RATIO VARIATIONS ALONG THE FLAT EVENT IN LUVA GAS DISCOVERY (6707/10-1) AND IN SOLSIKKE WELL (6403/10-1)

	ΔVp (m/s)	ΔVs (m/s)	Δρ (g/cm3)	ΔPoisson's Ratio
Solsikke	107	17	0.015	0.007
Luva gas discovery	287	1	0.06	0.057

Based on Table 3.10, the increase in V_p and density is higher in the base of the Luva gas discovery (6707/10-1), whereas Solsikke well (6403/10-1) shows a notable increase in V_s. The result is a higher change in Poisson's ratio in the Luva discovery (6707/10-1, in Vøring Basin) than in the Solsikke well (6403/10-1, no-discovery in Møre Basin).

When comparing the variation of amplitude with incident angle for both wells (Figure 3.17), the amplitude increases in both Luva gas discovery (6707/10-1) and Solsikke well (6403/10-1) for large angles. However, this increment is much lower in Solsikke (6403/10-1) due to a lower Poisson ratio variation, as it will be discussed later.

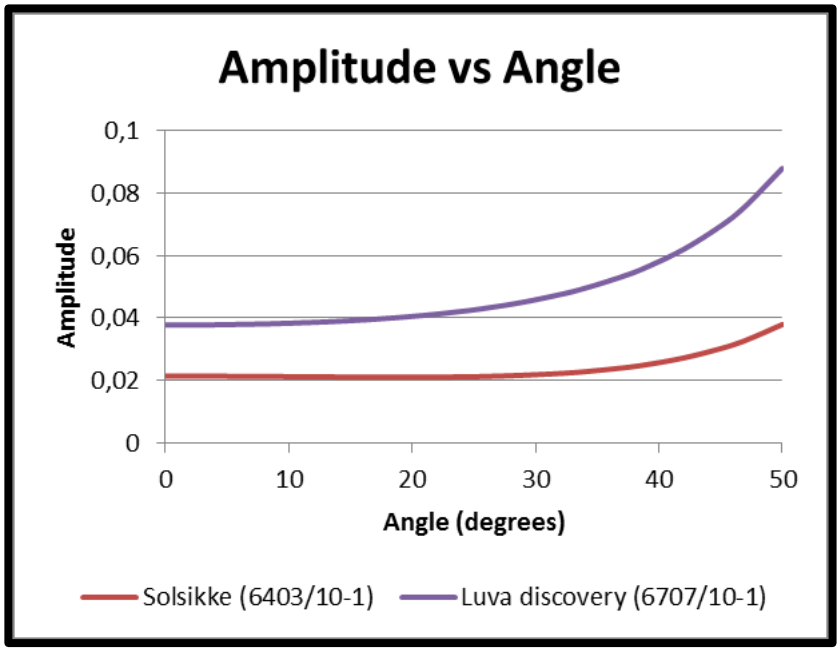

FIGURE 3. 17 - AMPLITUDE VS INCIDENT ANGLE VARIATION IN SOLSIKKE WELL (6403/10-1) AND LUVA DISCOVERY WELL (6707/10-1).

No-sand reservoir case (6404/11-1)

Well 6404/11-1 is a dry well with poor sand presence. This is observed in Figure 3.18, where the Nise Fm. (highlighted) does not show any sand interval in the Gamma Ray log and there is no hydrocarbon sign in the resistivity log. The absolute values of amplitudes, both positive and negative, increase with incident angle in partial-stack data (appendix A). The AVA response for pure-brine saturation is studied on top of the Nise Fm. in order to check whether the observed amplitude variation with angle can be reproduced. For this purpose, wiggled traces are generated by 26-m blocking logs for angles between 0° and 50° (Figure 3.19).

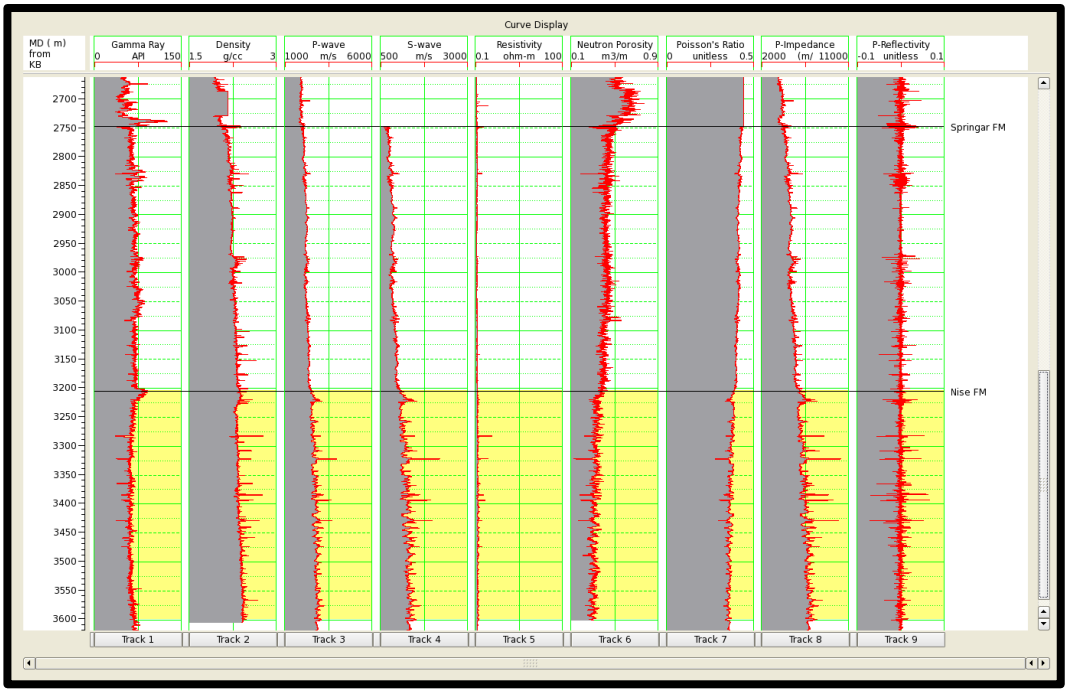

FIGURE 3. 18 - GAMMA RAY, DENSITY, V_P, V_S, RESISTIVITY AND NEUTRON POROSITY FROM WELL 6404/11-1 COMPOSITE LOG. POISSON'S RATIO, P-IMPEDANCE AND P-REFLECTIVITY ARE CALCULATED. AREA OF INTEREST BETWEEN NISE FM. TOP AND 3600 METERS IS HIGHLIGHTED.

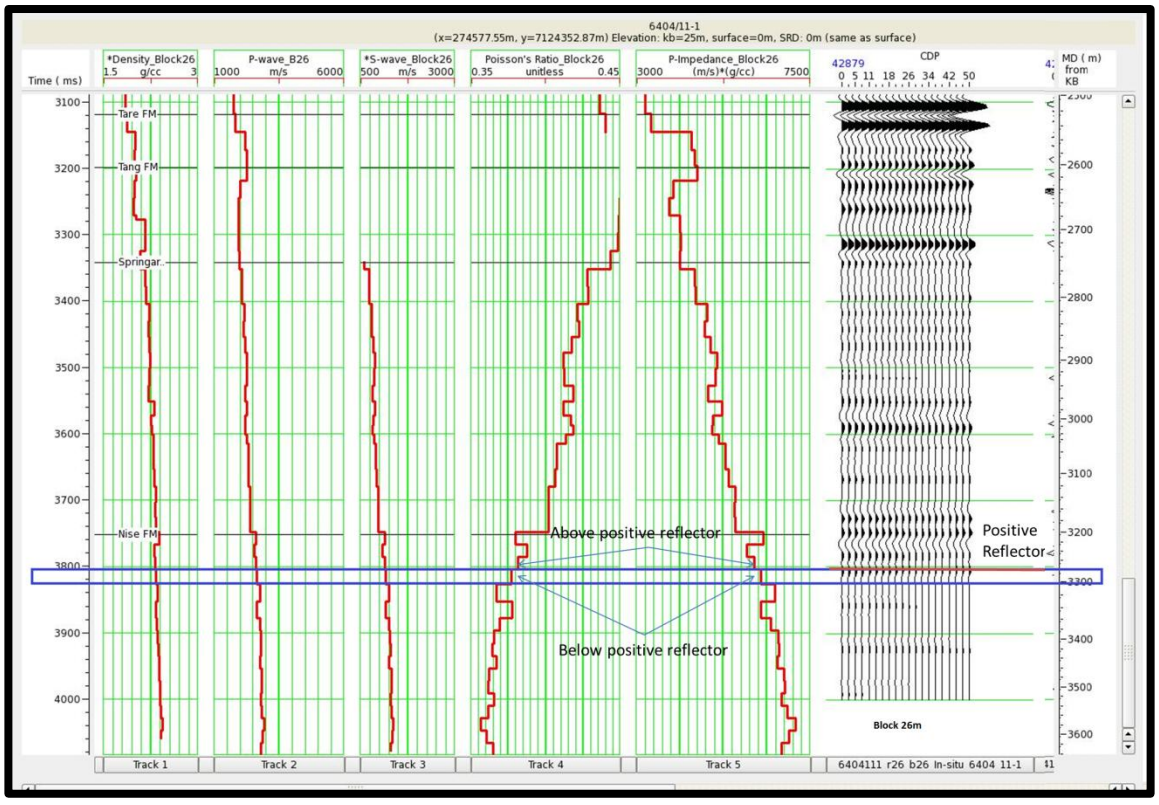

FIGURE 3. 19 - P-IMPEDANCE AND POISSON'S RATION ARE DISPLAYED FOR BLOCKING OF 26 METERS. SYNTHETIC SEISMIC TRACES FOR ANGLES BETWEEN 0 AND 50 ARE ALSO DISPLAYED.

In Figure 3.19, the amplitude seems to be constant for all traces in the target reflector. The effective elastic properties above and below the positive target reflector (see Figure 3.19) are

listed in Table 3.11, and variations in elastic properties between layers are in Table 3.12. In Table 3.12, an increase in V_p, density (and hence, impedance) and V_s is observed. However, the change in Poisson's ratio is small and negative, opposite to what was found in the base of Luva discovery (6707/10-1) and the Solsikke well (6403/10-1).

TABLE 3. 11 - V_P, V_S, DENSITY AND POISSON'S RATIO ABOVE AND BELOW POSITIVE REFLECTOR OBSERVED IN WELL 6404/11-1

	Vp (m/s)	Vs (m/s)	ρ (g/cm3)	Poisson Ratio
Above positive reflector	2610	1139	2.33	0.381
Below positive reflector	2660	1177	2.34	0.377

TABLE 3. 12 - V_P, V_S, DENSITY AND POISSON'S RATIO VARIATIONS ALONG THE POSITIVE REFLECTOR IN WELL 6404/11-1

	ΔVp (m/s)	ΔVs (m/s)	Δρ (g/cm3)	ΔPoisson's Ratio
6404/11-1	50	38	0.01	-0.004

Figure 3.20 shows that the amplitude remains approximately constant in well 6404/11-1 for all angle ranges. For comparison, variation of amplitude with angle for Luva gas discovery well (6707/10-1) is also plotted.

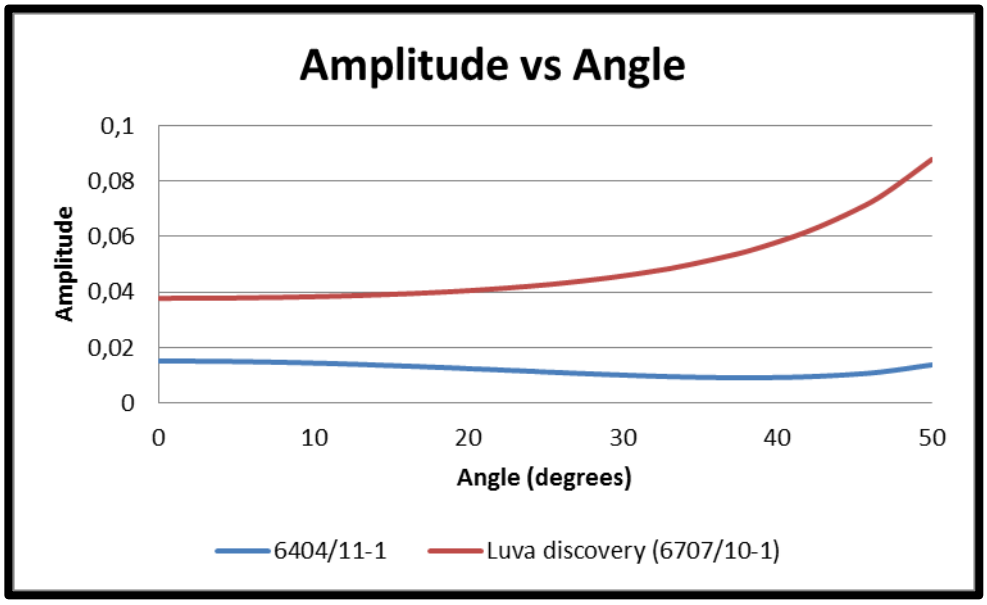

FIGURE 3. 20 - AMPLITUDE VS ANGLE VARIATION IN WELL 6404/11-1 WITH BLOCK 25M AND WELL 6707/10-1

3.4 Discussion

The 3-terms Aki-Richards (1980) approximation (first-order linearized simplification of the Zoeppritz equation) can be rearranged and interpreted in terms of different incident angles (Avseth et al., 2005):

$$R_{pp}(\theta) = R_p + Gsin^2\theta + F(tan^2\theta - sin^2\theta) \quad (3.10)$$

Where:

- $R_{p=}\frac{1}{2}\left(\frac{\Delta V_p}{V_p}+\frac{\Delta\rho}{\rho}\right)$ is the normal-incidence reflection coefficient. (3.11)
- $G = \frac{1}{2}\frac{\Delta V_p}{V_p} - 2\left(\frac{V_s}{V_p}\right)^2\left[2\frac{\Delta V_s}{V_s}+\frac{\Delta\rho}{\rho}\right]$ is the dominant term in intermediate angles. (3.12)
- $F = \frac{1}{2}\frac{\Delta V_p}{V_p}$ is the dominant term in far angles, near the critical angle. (3.13)

The Poisson's ratio is related to the V_p/V_s ratio as:

$$\vartheta = \frac{0.5\left(\frac{v_p}{v_s}\right)^2-1}{\left(\frac{v_p}{v_s}\right)^2-1} \quad (3.14)$$

From the equation 3.14, it can be inferred that a decrease in Poisson ratio (decrease in $(V_p/V_s)^2$) will imply an increase in $(V_s/V_p)^2$ and, hence, a more negative AVO gradient (G) (equation 3.12). As a consequence, negative amplitudes will become even more negative when angle increases.

On the other hand, if the Poisson ratio increases (increase in $(V_p/V_s)^2$ ratio), it will imply a decrease in $(V_s/V_p)^2$ and the effect of negative second term in AVO gradient will be much lower (equation 3.12).

3.4.1 Gas effect in Vøring Basin cases

In the top of the Delfin Fm. in Luva gas discovery (well 6707/10-1) and clean-sand case in Gjallar Ridge well (6704/12-1 with residual gas), it was found that the effect of gas produced a decrease in V_p and density. Since V_s is less sensitive to pore fluid, the Poisson's ratio decreased dramatically. A cross-plot of V_p versus Poisson's ratio and V_s versus Poisson's ratio for in-situ conditions in both cases illustrates this effect (Figure 3.21 and Figure 3.22):

- In Figure 3.21a, low values of V_p and Poisson's ratio corresponds with the reservoir in Luva discovery whereas, in Figure 3.21b, the reservoir can be identified due to the low value of Poisson's ratio, but V_s shows normal values.
- In Figure 3.22a, low values of V_p and Poisson's ratio corresponds with sands with residual gas in Gjallar Ridge well. In Figure 3.22b, these sands can be identified due to the low value of Poisson's ratio, but V_s shows normal values.

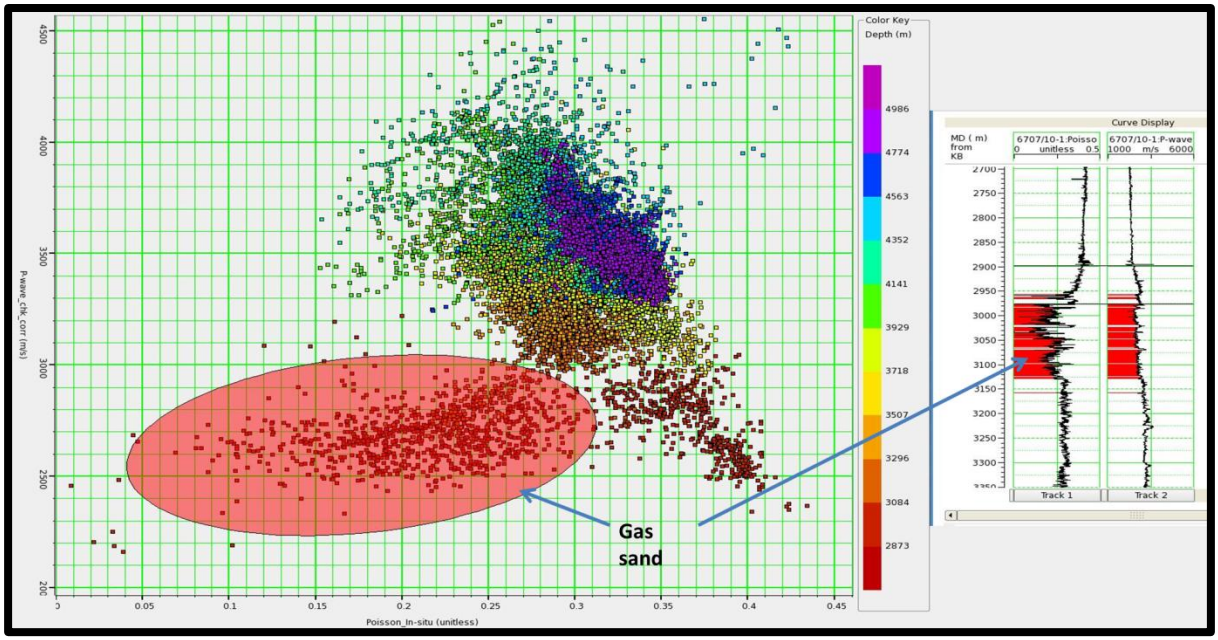

(A)

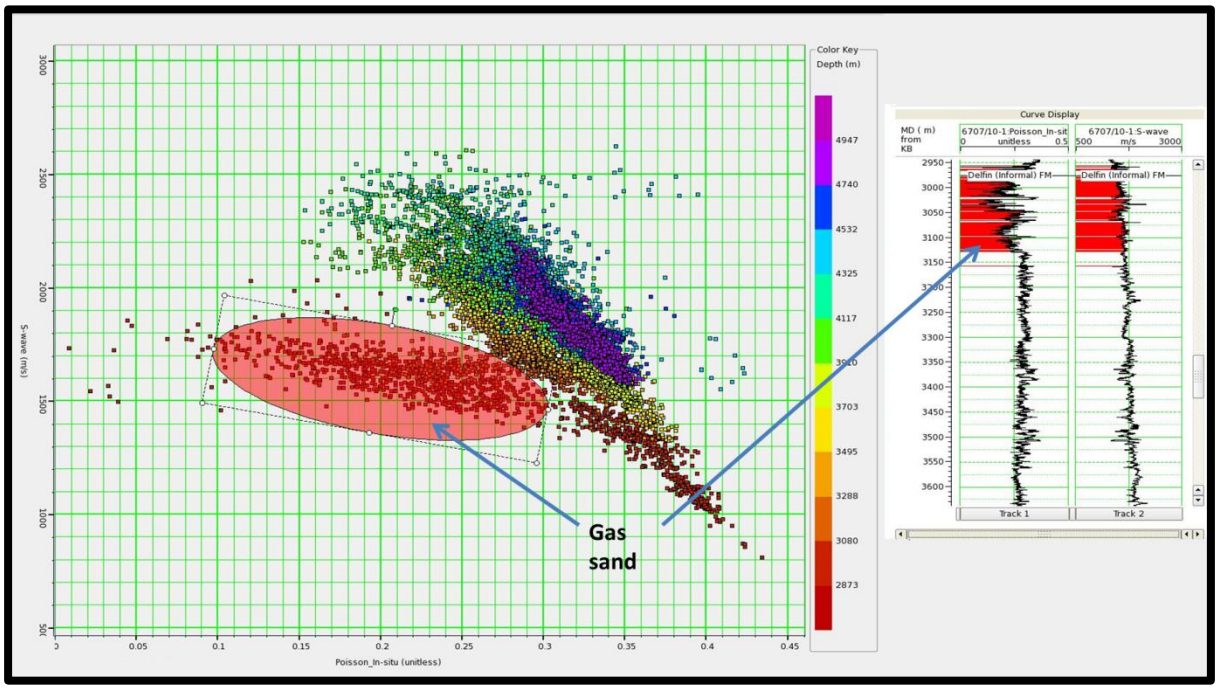

(B)

FIGURE 3. 21 - (A) V_P VS POISSON´S RATIO AND (B) V_S VS POISSON´S RATIO (LUVA GAS DISCOVERY). BOTH DEPTH COLOUR CODED.

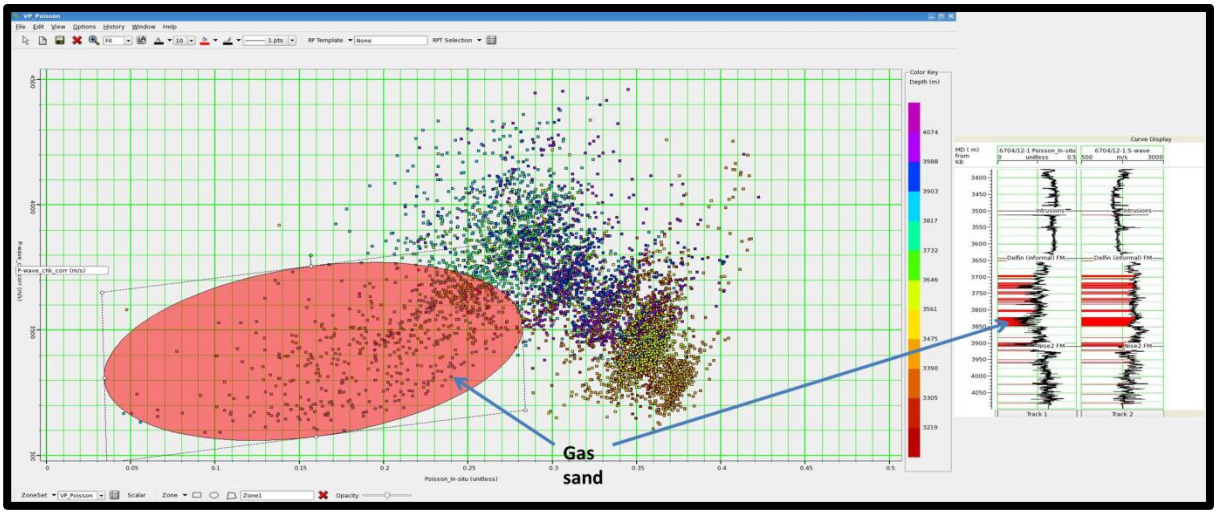

(A)

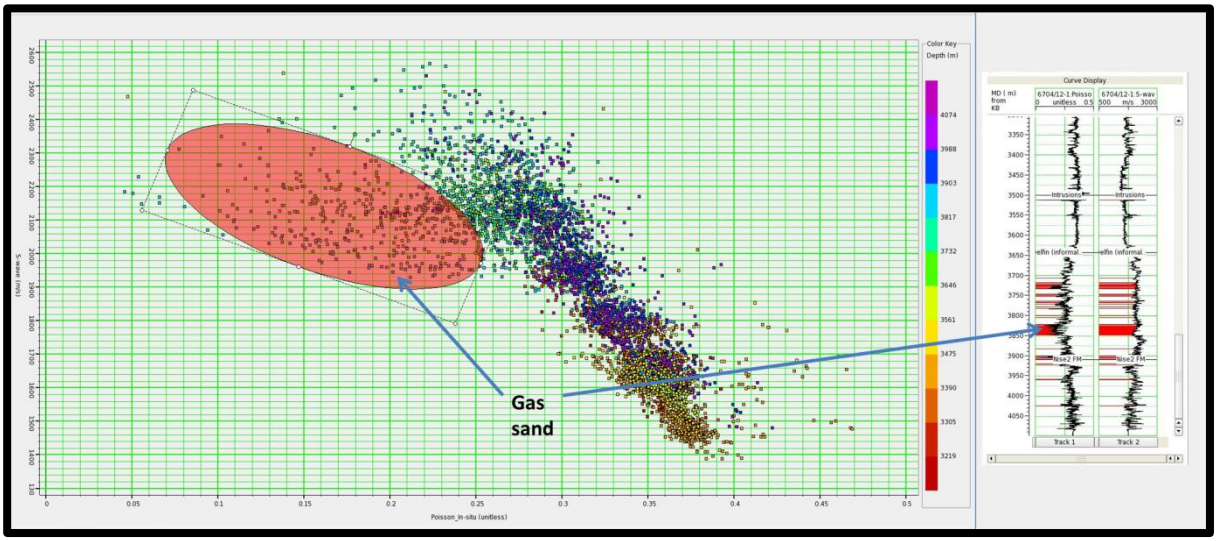

(B)

FIGURE 3. 22 - (A) V_P VS POISSON´S RATIO AND (B) V_S VS POISSON´S RATIO (GJALLAR RIDGE, MARGINALLY GAS SATURATED SAND CASE). BOTH DEPTH COLOUR CODED.

The variations in elastic properties along the top of the reservoir in Luva gas discovery (well 6707/10-1) and the top of the clean sands in, marginally gas saturated, Gjallar Ridge well (6704/12-1) for in-situ cases are listed in table 3.13.

TABLE 3. 13 - V_P, V_S, DENSITY AND POISSON'S RATIO VARIATIONS ALONG TOP REFLECTORS IN LUVA GAS DISCOVERY (6707/10-1) AND GJALLAR RIDGE (6704/12-1)

	ΔVp (m/s)	ΔVs (m/s)	Δρ (g/cm3)	ΔPoisson's Ratio
Luva (6707/10-1)	-195	101	-0.299	-0.071
Gjallar Ridge (6704/12-1)	-205	14	-0.072	-0.051

The results observed in both models can be explained based on equation 3.10 and on the variation of the elastic properties (Table 3.13). The R_p, G and F coefficients in equation 3.10 are calculated in appendix E:

- The normal-incidence reflection coefficient (R_p) is negative in both cases due to the decrease in density and V_p, i.e., a decrease in acoustic impedance.
- The AVO gradient (G) is negative due to the decrease in V_p and the increase in V_s.
- For far angles, F is negative due to a decrease in V_p.
- This combination produces negative amplitudes at zero incident angle that decrease (increase in absolute value) with angle. This is what the model for in-situ cases shows (figures 3.11 and 3.14) and also what is observed in real data (see section 3.4.4).
- The effect on residual gas and high-gas saturation leads to a very similar decrease in V_p and Poisson's ratio. Hence AVO-AVA analysis will not be able to discriminate gas saturations between 10% and 90%.

3.4.2 Flat event analysis in Solsikke and Luva gas discovery reservoir base

In the flat event in Solsikke well (6403/10-1 in Møre Basin) (appendix D), it was found that V_p, V_s and density increase below the reflector and Poisson's Ratio also slightly increases. The observed results in synthetic traces for this case can be explained based on equation 3.10 and the variation of the elastic properties (Table 3.10). The R_p, G and F coefficients in equation 3.10 are calculated in appendix E:

- The normal-incidence reflection coefficient (R_p) is positive in both cases due to the increase in density and V_p, i.e., the increase in acoustic impedance.
- The AVO gradient (G) is positive and very small. The reason is that the increase in V_p is compensated by the second term. This term is negative due to the positive and relatively large variation in V_s and the positive variation in density.
- For large angles, F is positive due to an increase in V_p.
- This combination produces positive amplitudes at zero incident angle that maintains almost constant for intermediate incident angles, but increase slightly for large incident angles. This is what the model shows and also what it is observed in real data (see section 3.4.4).

When flat events (appendix D) in Solsikke (Møre Basin) and the reservoir base in Luva gas discovery (Vøring Basin) were compared, the result was a variation of amplitude with incident angle in both cases, but higher in the Luva gas discovery (Figure 3.17). These results can be explained based on the equation 3.10 and the variation of the elastic properties (Table 3.10):

- Both wells show an increase in V_p velocities, density and Poisson's ratio, but it is much higher at the Luva gas discovery due to the gas-water transition.

- Solsikke well shows an increase in V_s while, in the Luva gas discovery, it is almost constant. V_s is more or less fluid-insensitive (Avseth et al., 2005) and therefore does not change between gas-saturated sandstones and brine-saturated sandstones, whereas lithological/diagenetics effects will change V_s, as it might happen in Solsikke well (6403/10-1). However, a more detailed rock physics study is necessary to confirm this statement.
- When R_p, G and F factors are calculated (appendix E), all of them are larger in the Luva gas discovery (Vøring Basin) than in the Solsikke well (Møre Basin).
- The effect in seismic response is a higher amplitude variation with incident angle in the Luva gas discovery due to a larger positive variation of V_p and a lower effect of density and V_s (Figure 3.17).

3.4.3 No-sand reservoir case in Møre Basin

In Well 6404/11-1 (Møre Basin), amplitude in synthetic traces showed to remain approximately constant. The result also showed increases in V_p, V_s and density and a very small decrease in Poisson´s ratio. The observations in synthetic traces can be explained based on equation 3.10 and the variation of the elastic properties through the reflector (Table 3.12) (The R_p, G and F coefficients in equation 3.10 are calculated in appendix E):

- Normal-incidence reflection coefficient (R_p) is positive and small due to the slightly increase in density and V_p, i.e., the increase in acoustic impedance.
- AVO gradient (G) is negative due to a relative small variation in V_p and density and a notable increase in V_s.
- For large angles, F is slightly positive due to a relative small increase in V_p.
- This combination produces positive amplitudes at zero offset that slightly decrease with offset. For large angles there is a slightly increase with offset. However we can consider that there is almost no change in amplitude with angle.

3.4.4 Qualitative comparison with seismic data

In this section, a comparison between partial-stack time-migrated sections and synthetic NMO-corrected CMP gathers is done for each well. As in the partial stacks a range of incident angles is stacked, migrated and loaded in Charisma database, this comparison is qualitative, i.e., only the trends are compared (Figure 3.23).

Vøring Basin cases

Luva gas discovery (Well 6707/10-1, Nyk High)

The well was a gas discovery and the synthetic model shows a class-III AVO anomaly. Unfortunately, there is no partial-stack data to compare with. However, Figure A.5 (appendix A) seems to show higher amplitudes in far-angle stack (large incident angles) than in near-angle stack (small incident angles).

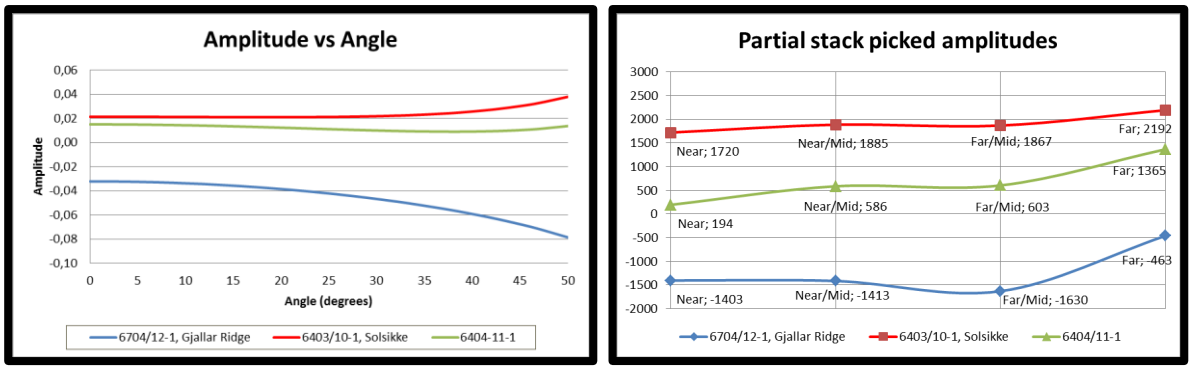

(A) (B)

FIGURE 3. 23 – (A) AMPLITUDE VARIATION WITH INCIDENT ANGLE IN SYNTHETIC MODELS AND (B) PICKED AMPLITUDES IN PARTIAL STACK DATA (NEAR, NEAR/MID, FAR/MID, FAR)

Gjallar Ridge (Well 6704/12-1, marginally gas saturated sand)

The well was dry at the Nise Fm but petrophysical analysis shows residual gas saturations of approximately 10%. The partial stacks, from a seismic line located 248 m north of the well, are shown in Figure A.6 (appendix A). The synthetic model (Figure 3.23a) shows that the amplitude becomes more negative with angle and the partial stacks show that the amplitude slightly becomes more negative up to Far/Mid angles (Figure 3.23b), i.e., both follow the same trend. However, for the Far partial stack section, this is not the case because the amplitude (in module) decreases, right the opposite to the synthetic model result. Possible explanations for the different results (partial stacks vs synthetic model) are:

1. Partial stacks shows at the Delfin interval how the sandstones layers are pinching out towards the well. This produces tuning effects that create interferences and therefore mask the AVO variation. Note how in the far stack, due to its lower frequency content, the vertical resolution is not enough to resolve the pinch-out.
2. The synthetic model neglects noise effects that could be present in the seismic and could mask the AVO variation.
3. The synthetic model does not consider lateral velocity variations which could have an impact at larger angles.

Møre Basin cases

Solsikke (Well 6403/10-1)

The well was drilled to test a flat event at the Nise Fm, but it found no hydrocarbons and poor reservoir properties. The partial stacks, from a seismic line located 19-m away of the well, are shown in Figure A.7 (Appendix A). The synthetic model shows a slight increase in amplitude with angle at the flat event location and a similar effect is observed in the partial stacks (Figure 3.23a and Figure 3.23b). In this case the seismic data is very close to the well location so a direct comparison is valid.

Well 6404/11-1

The well was dry at the Nise Fm and showed very poor reservoir properties. The partial stacks, from a seismic line located 326 m away of the well, are shown in Figure A.8 (Appendix A). The synthetic model shows a positive reflection due to the increase in density and V_p with almost no amplitude variation with incident angle (Figure 3.23a). However, partial stacks show a positive reflection which increases with angle (Figure 3.23b). Possible explanations for the different results (partial stacks vs synthetic model) are:

1. As in Gjallar Ridge well (6704/12-1) case, noise effects and lateral velocity variations could have masked the AVO variation.
2. As the well is not located at the seismic line, there might be small lateral changes in lithology that could change the seismic response such as pinch-outs, narrow channels or faults. A good solution for imaging these potential geological features would be a 3D seismic coverage.

During this chapter, amplitude has been considered as a scaled version of reflectivity. However, wave propagation may produce amplitude variations not necessary related to reflectivity. In addition, partial stack sections have been compared with AVO-AVA model results. These sections are derived from angle-based mute functions as it was explained in the introduction. In the next chapter, the incident-angle ranges associated with angle mute functions will be reviewed and the wave propagation effects will be investigated by 2D seismic modelling.

Chapter 4: Ray-Tracing modelling

4.1 Theoretical Framework

Ray tracing is an approximation of the general seismic wave equation solution. It is valid for high frequencies and, hence, for short wavelengths. This limitation has practical effects when generating models (Gjøystdal et al., 2007):

- The seismic wavelength must be significantly smaller than the smallest details of the model (e.g., radius of curvature and length of the interfaces or layer size). In other words, the model must only represent large scale elements and characteristics and is therefore a so-called macro model.
- Interfaces and elastic properties must therefore be smoothed to remove small details and variations.
- During depth conversion and velocity estimation, time horizons and velocity functions must be smoothed as well.

Geometrical ray tracing

In geometrical ray tracing, rays are reflected and transmitted following Snell's law at all interfaces. The ray source, the initial ray direction and the ray code must be defined from the beginning. The ray code defines the rules which establish the ray (reflected or transmitted, P or S) that is generated when an incident ray reaches an interface. Geometrical ray tracing can be implemented in two ways:

- Kinematic ray tracing – Raypaths and traveltimes along the raypath can be calculated with this method. The inputs are the wave velocities (V_p and V_s) in each layer of the model. The process is as follow:
    - Within a layer, raypaths and traveltimes are calculated by solving the kinematic ray-tracing differential equation system. The result depends on the velocity function within the layer (e.g., if velocity is constant, the result is a straight line).
    - When the ray is close to the next layer, the *intersection point* at the interface is calculated.
    - At the interface, the ray code is checked to determine which rays will follow. The ray directions are given by the Snell's law.
    - These previous three steps are repeated in each layer until a *stop criterion* is satisfied. This criterion is defined in the ray code. Examples of stop criteria are when the ray gets specific traveltimes, or when the critical angle is reached, etc.
- Dynamic ray tracing – This method is applied after kinematic ray tracing to compute along a raypath seismic wavefield properties such as wavefront curvature and amplitude coefficients. The inputs are the wave velocities (V_p and V_s) and the density in each block of the model.

The overall ray-tracing process (Figure 4.1) used to generate all parameters is as follow (NORSAR-2D manual):

- Raypath and traveltimes along the raypath are calculated with the kinematic ray tracing. Values of geometrical spreading factors (G), wavefront curvatures (K) and amplitude coefficients (A real, B imaginary) are also provided in the source point.
- Within each layer, G, K, A, and B are computed along the raypaths.
- At the interfaces:
    - The change in G and K values due to transmission and reflection is calculated by wavefront conversion.
    - The new transmission and reflection coefficients are calculated by amplitude conversion.

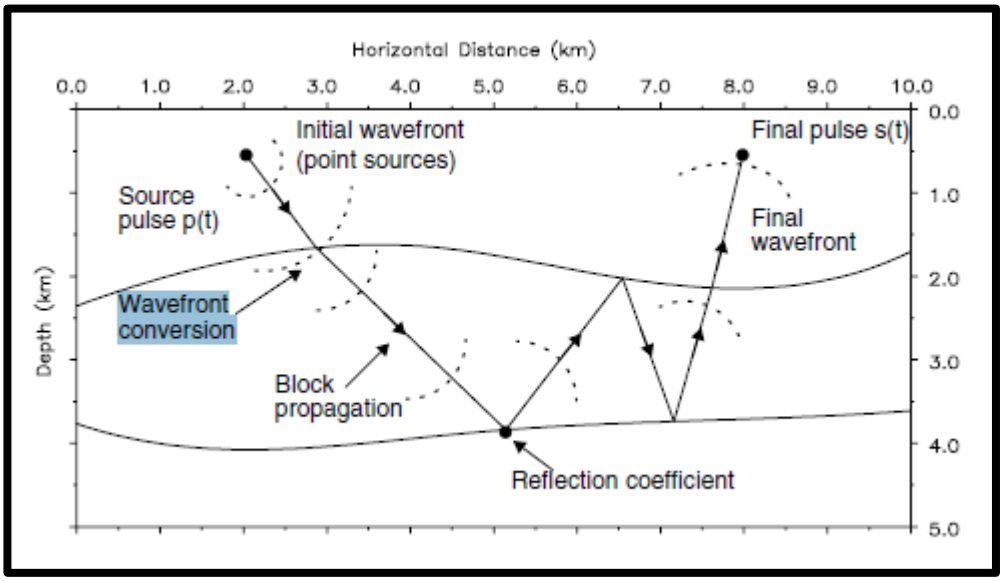

FIGURE 4. 1 - SCHEMATIC REPRESENTATION OF DYNAMIC RAY TRACING (NORSAR-2D MANUAL)

Seismic modelling: two-point ray tracing

In a seismic survey, a source generates a pulse that is recorded by some receivers and, hence, only raypaths between the source and given receivers are of interest. However, the initial ray direction for a ray which arrives at a specific receiver is unknown. In order to determine the initial direction, the "shooting method" is used in an iterative manner:

- A ray fan is shot in a large range of directions with a given sampling in shooting direction.
- Rays passing close to receivers are selected and a denser fan of rays is produced for near directions. This process is repeated until the source-receiver ray is found within a given accuracy (maximum distance to the given receiver position, e.g., 10 cm). For the iterative process, NORSAR-2D uses the "paraxial method", where every new ray is calculated from the previous ray spreading factor by using dynamic ray tracer.

When all source-receiver rays are found, all parameters calculated by ray tracing (e.g., traveltimes, complex amplitudes, polarization, etc.) are stored in an "event" file, each event corresponding to one arrival for the corresponding shot/receiver pair. Such parameters might be used directly for various analyses, as will be done in the present work to study amplitudes and reflectivity as function of incident angle, etc. Eventually, synthetic seismograms can be calculated, using the parameters in an event file and a selected time pulse, and compared with real data. For each source/receiver pair, a trace is obtained by convolving the time pulse with a reflectivity log containing all arrivals recorded at the receiver and applying the complex amplitudes obtained by dynamic ray tracing.

4.2 Methodology

In order to investigate the possible propagation effects in the amplitude, two 2D-models are created:

- Vøring Basin line model: Line MNR04-7452 and Gjallar Ridge well (6704/12-1) are used as inputs for this model.
- Møre Basins line model: Line MNR07-208 and Solsikke well (6403/10-1) are the inputs in this case.

To create these models in depth, laterally-varying interval velocities are derived from time-migrated horizons and stacking velocities following the approach of Hubral (1980). When the interval velocity is known, time-migrated horizons can be migrated to depth. In these processes, two ray techniques are used:

- Normal Incidence Path (NIP) ray tracer – Shot-receiver pairs (zero-offset survey) are regularly distributed along a horizontal line and they can be projected to a horizon if needed (e.g., seafloor or earth's surface). Rays are traced from and perpendicular to the selected reflectors to all shot-receiver points. This configuration simulates post-stack non-migrated data.
- Image ray tracer – Shot-receiver pairs (zero-offset survey) are regularly distributed along a horizontal line. Rays are vertically shot and they are traced until the stop criterion is met. Two-way traveltimes (TWT) are calculated when an interface is intersected. This configuration simulates post-stack time-migrated data.

Once the models are defined, they are compared at well positions with check-shots and well logs in order to calibrate and validate the model. Finally, the seismic survey is simulated and amplitudes, reflectivity, etc., are extracted for rays hitting the target reflector and are then analysed. The simulation is done by using the common shot tracer module, in which shots and receivers are regularly distributed and receiver positions are coupled to the shot positions (e.g., marine surveys with streamers towed behind a boat as is the case here).

4.2.1 Seismic interpretation

Lines MNR04-7452 near to Gjallar Ridge (6704/12-1) well (Vøring Basin line model) (Figure 4.2) and MNR07-208 near to Solsikke (6403/10-1) well (Møre Basin line model) (Figure 4.3) were interpreted as a first input for ray tracing modelling. Note that, due to ray-tracing requirements (smoothness with respect to wavelength), the interpretation does not focus on small details.

The interpretation was done along the Top of the representative groups and formations. In Figure 4.2, there is a clear change in the seismic character and the structural configuration from the Tertiary to the Cretaceous section (above and below dark blue horizon). The Tertiary sediments are characterized by parallel to subparallel reflectors with amplitudes that range from high to medium-low depending on the seismic sequences. No major deformation is observed. On the contrary, Cretaceous sediments are distributed along synthetic and antithetic lystric faults and are characterized by medium to low amplitudes. To the West, just beneath the Shetland reflector (dark blue horizon), there is a high amplitude and chaotic seismic package that represent thick intrusions.

In Figure 4.3, the two different deformation regimes are also observed in the southern part of the section: the main faulting activity occurs in the Cretaceous section (above and below dark blue horizon) while the Tertiary seems to be a relatively tectonically quiet period. The situation changes in the northern part where Cretaceous faults are reactivated during the Tertiary up to even Neogene times (seafloor). The high amplitude events observed above Shetland reflector (dark blue horizon) to the south correspond again to basalt intrusions.

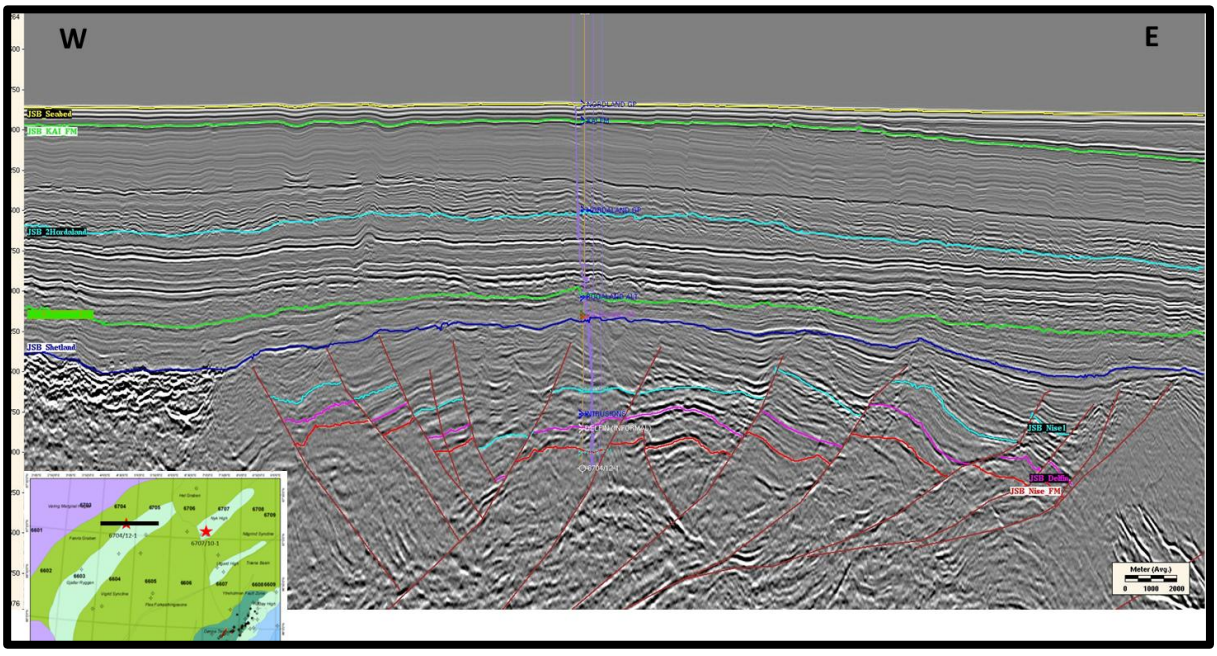

FIGURE 4. 2 - INTERPRETATION OF SEISMIC LINE MNR04-7452 AROUND GJALLAR RIDGE WELL (6704/12-1, SANDS WITH MARGINAL GAS). THE DELFIN HORIZON (DARK GREEN AT ABOUT 3800 MS) IS THE TARGET IN THE STUDY.

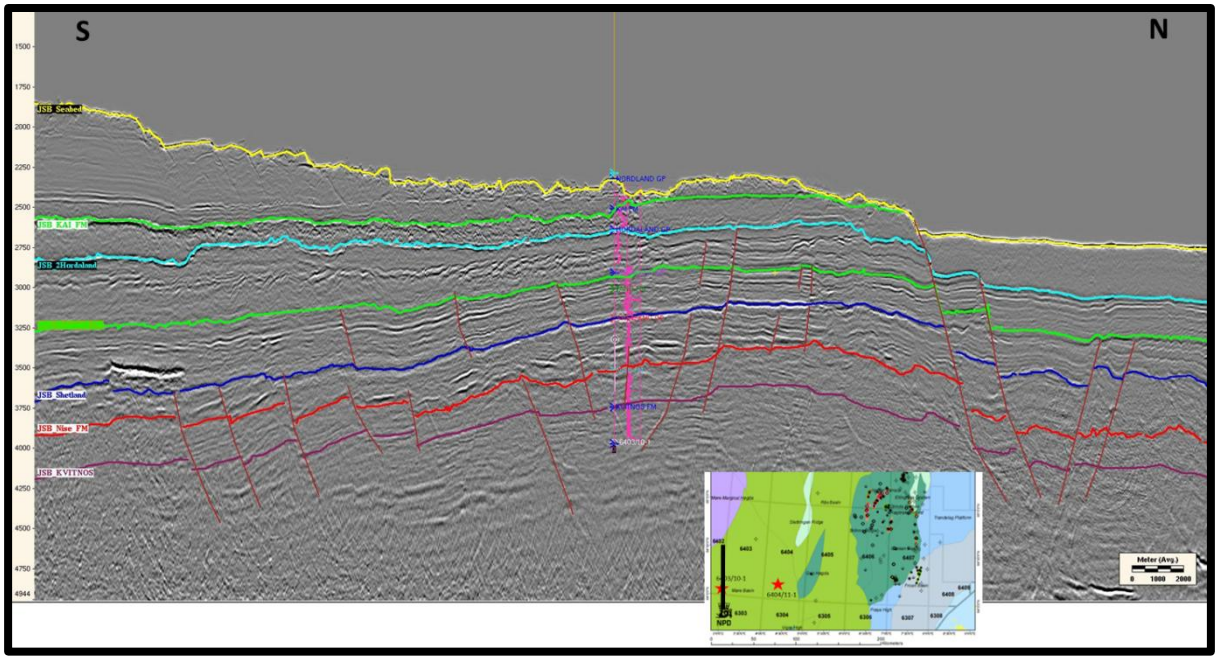

FIGURE 4. 3 - INTERPRETATION OF SEISMIC LINE MNR07-208 AROUND SOLSIKKE WELL (6403/10-1, NO SAND). THE NISE HORIZON (RED) IS THE TARGET IN THIS STUDY.

4.2.2 NORSAR-2D Data Preparation

- **Model project definition** – The modelling project was defined to cover an area that includes Vøring Basin and the north of Møre Basin (Figure 4.4).

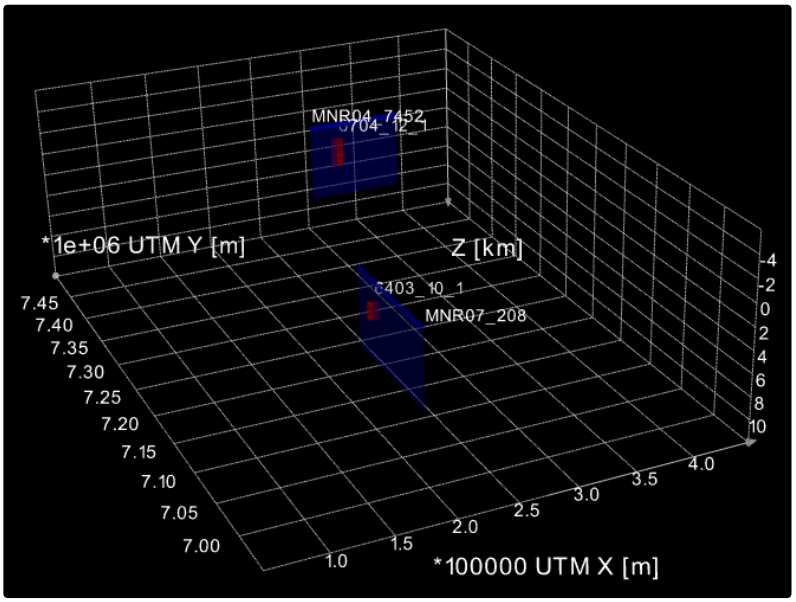

FIGURE 4. 4 - CUBE SHOWING THE AREA DEFINITION FOR THE PROJECT. LINE MNR04-7452 AND WELL 6704/12-1 (VØRING BASIN LINE MODEL) IN THE NORTH AND LINE MNR07-208 AND WELL 6403/10-1 (MØRE BASIN LINE MODEL) IN THE SOUTH.

- **Lines and section definition** – Information required for creating 2D lines includes first and last CDP and their positions (in UTM coordinates). These were extracted

from seismic data SEG-Y files using Seismic Unix (SU webpage). So-called Modelling sections were then created associating each section to a 2D line.

- **Stacking velocities** – In NORSAR-2D, a stacking velocity grid is derived from "stacking velocity function" (stacking velocity as a function of TWT at a given CMP position). These functions are stored in *.Stab files and there is no possibility to import them from Charisma stacking velocity formats as produced here (*.VG_VBASE). For this reason, a script was developed to transform Charisma format into NORSAR-2D format (VBASE2STAB.vbs in appendix G). Once the stacking velocity functions are loaded, the stacking velocity grid can be generated in Velocity Estimator module. Note that the stacking velocity grid must be smoothed to meet ray tracing requirements.
- **Horizons import** – NORSAR-2D allows importing Charisma horizon files with the Import/Export module. However, these files had to be resampled before importing due to the large density of samples.

4.2.3 Creation of a model in depth

A model in depth can be created by using the NORSAR-2D Velocity Estimator and Model builder modules in parallel. In the present case, full-stack time-migrated horizons (in zero-offset TWT) and interval velocities estimated from stacking velocities were used. Note that the interval velocities obtained in this manner can only vary laterally in the model, but are constant vertically for each layer. As each layer is delimited by the interpreted horizons (see Figures 4.2 and 4.3), the choice of the latter is crucial for the validity of the final model. Well logs help however to tie the model in depth.

To build the model in depth, an iterative process is followed, starting from the shallower layer and finishing in the deepest. This process is described below and shown in detail in appendix F:

1. In Model builder, an initial model is generated and stored. This model has two layers with a constant V_p corresponding to the water layer (constant velocity of 1480 m/s) and the seabed at its proper position in depth (depth conversion performed in the same module).
2. In Velocity Estimator, this initial model is loaded. At the start of the process, a stacking velocity grid must be loaded and CMP positions used for the estimation must be selected. Then, the first time horizon (below seabed) that will be migrated is selected and the uncertainties and acceptance limits for velocity estimation are set. Finally, the estimation process can be launched. The output of this process is a velocity sample file giving estimates of possibly laterally-varying interval velocities above the selected horizon.
3. In Model builder, the velocity sample file is loaded and it can optionally be modified and smoothed before creating a sampled velocity function (constant, linear trend or spline representation). Then, the velocity function is assigned to the layer right below the previously depth-converted horizon.

4. Still from Model Builder, the corresponding time horizon can be depth converted using the estimated interval velocities. As the time horizons are already migrated in this study, the image ray tracer described earlier is used in this step for proper lateral positioning. The model will now include a new layer at its bottom down to the depth converted horizon and is therefore updated for the following step.
5. The new model is loaded in the Velocity Estimator module (see step 2) and the process is repeated for the next time horizon until there are no more time horizons and the final depth model is built. Note that below the deepest horizon, no interval velocities can be estimated using the present process and only well logs (if deep enough) or other information can be used to assign properties at the bottom of the model.

In line MNR04-7452, only the part of the Nise Fm. and the Delfin Fm. around Gjallar Ridge well (between the two faults) was selected, and then, they were extended in the model.

4.2.4 Model calibration

In order to validate the models, data from wells present in the area are compared with data extracted from the models. Two key parameters are compared:

- Petromarkers – Depth migrated horizons are compared with petromarkers (formation tops) in depth in the well to check that they are in the right position.
- Interval velocities – Interval velocities are computed from check-shot log in the well and they are then compared with interval velocities in the model for each layer. Note that these velocities are V_p velocities.

Once the wells are calibrated, density and V_s properties must be included in the model for each layer because reflection coefficient depends on these two parameters in addition to V_p.

- Density is estimated by averaging density values from well composite logs in each layer. For layers where there is no density log, density is estimated from V_p with Gardner equation (Gardner et al., 1974):

$$\rho = 0{,}31 V_p^{0{,}25}, with\ V_p\ in\ m/s \qquad (4.\ 1)$$

- V_s is estimated with two methods:
  - The mudrock line equation (Castagna, 1985) is used in the Vøring Basin line model for the whole interval as it is considered a good approximation in a water saturated sandstone-shale system. Note that in areas of Delfin Fm. with marginal gas saturation this approximation slightly underestimates Vs.
  - The Greenberg-Castagna (1992) empirical relation (Equation 3.3) for shale is used in the Møre Basin line model, as it showed to be more accurate than the mudrock line equation.

V_p, V_s and density extracted from the model are compared with the same parameters extracted from wells check-shot and wire logs are in Figures 4.5 and 4.6.

- In Figure 4.5, the retrieved interval velocities in the model are not showing vertical variations within the layer as they can only vary laterally per definition in the used modelling method, whereas check-shot and well logs provides such vertical variations along the well. However, the correlation between Gjallar Ridge well (6704/12-1, sands with marginal gas case in Vøring Basin) check shot and wire logs and the model is fairly well.
- In Figure 4.6, the match between Solsikke well (6403/10-1, no sand case in Møre Basin) check shot and wire logs and the model is also good, with only a large deviation in Kvitnos formation. The reason is that the velocity for this layer has not been estimated because top Kvitnos was the last horizon that was used during the estimation. However, the study of amplitude is in top Nise, so this layer is not used during ray-tracing modelling.
- In Figure 4.5 and 4.6, density, which represents the average density in each layer, shows a fairly good match.

The final model for each case is in figure 4.7. Note how petromarkers in the well match with the depth-migrated horizons coming from seismic data in both cases. This confirms the validity of the elastic models in depth.

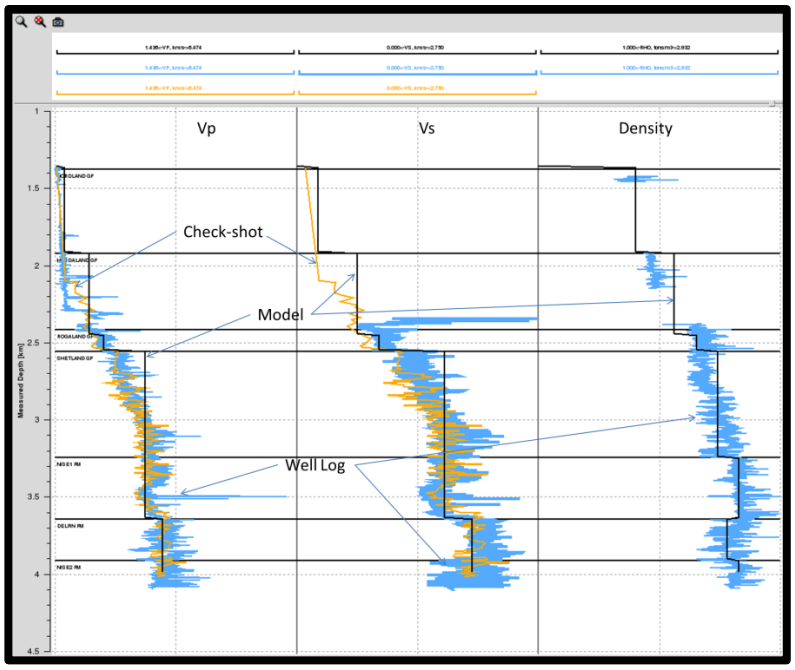

FIGURE 4. 5 - VØRING BASIN LINE MODEL CALIBRATION, SHOWING V_P, V_S AND DENSITY EXTRACTED FROM THE MODEL AND FROM WELL 6704/12-1 (SANDS WITH MARGINAL GAS) CHECK-SHOT AND WIRE LOG. V_S FOR THE MODEL AND CHECK-SHOT LOG IS DERIVED BY MUDROCK LINE EQUATION.

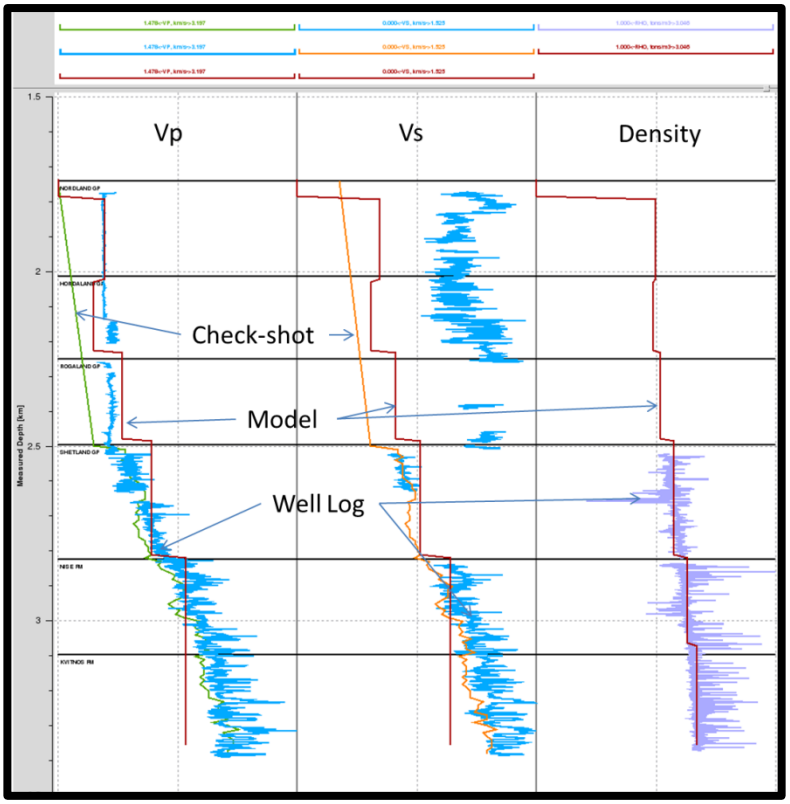

FIGURE 4. 6 - MØRE BASIN LINE MODEL CALIBRATION, SHOWING V_P, V_S AND DENSITY EXTRACTED FROM THE MODEL AND FROM WELL 6403/10-1 (NO SAND) CHECK-SHOT AND WIRE LOG. V_S FOR THE MODEL AND CHECK-SHOT LOG IS DERIVED BY GREENBERG-CASTAGNA (1992) EMPIRICAL RELATION.

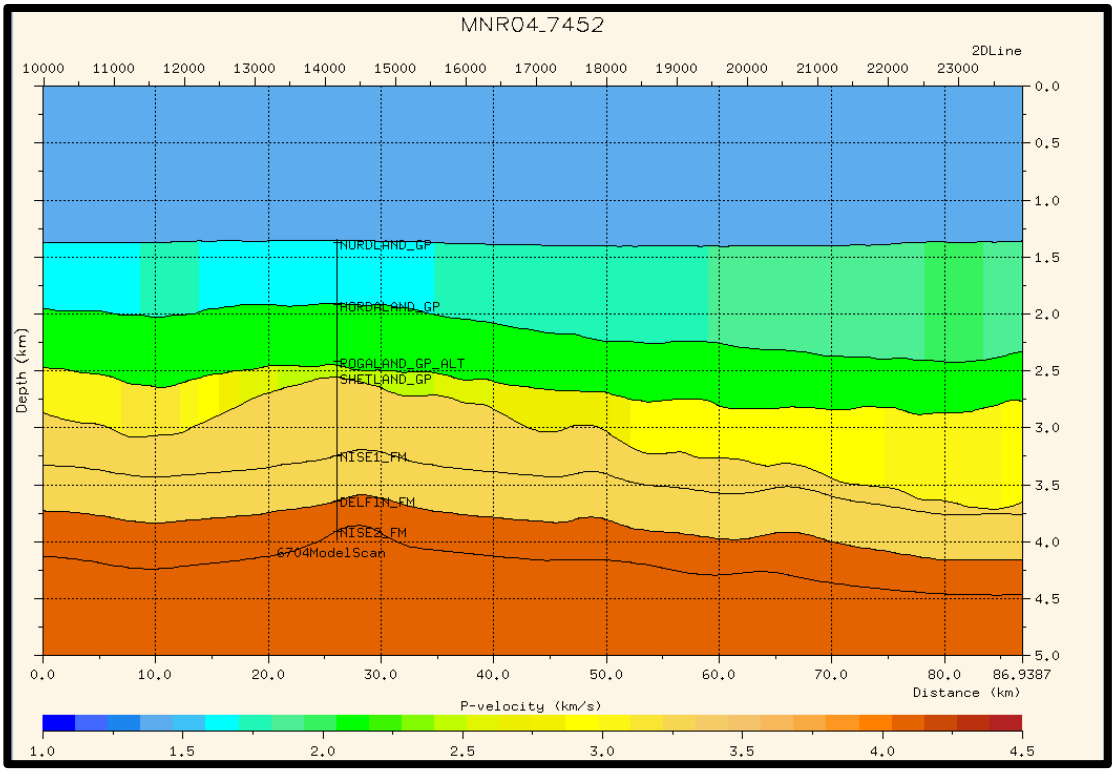

(A)

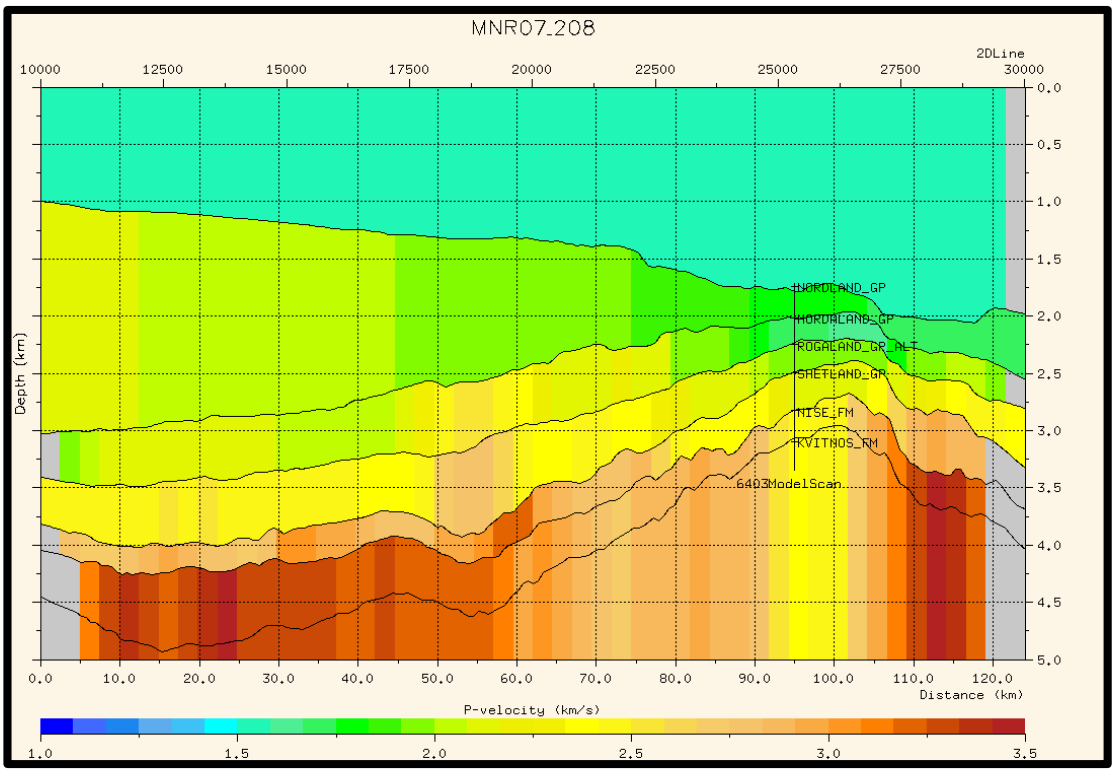

(B)

FIGURE 4. 7 - (A) VØRING-BASIN 2D MODEL (SEISMIC LINE MNR04-7452 AND WELL 6704/12-1; SANDS WITH MARGINAL GAS). (B) MØRE-BASIN 2D MODEL (SEISMIC LINE MNR07-208 AROUND WELL 6403/10-1; NO SAND). NOTE THAT THE VERTICAL SCALE (DEPTH) IS EXAGGERATED (VERTICAL/HORIZONTAL = 5) FOR A BETTER DISPLAY.

4.2.5 Seismic modelling

Seismic modelling allows us to include propagation effects when amplitudes are studied. In this project, ray-tracing modelling is used due to its fastness, flexibility and event-identification capability, i.e., for each source/receiver pair and considered reflection, raypath, amplitudes and many other parameters can be calculated, extracted and analysed. This is in contrary to more "black-box" process (e.g., finite-difference modelling) producing only seismograms, though the latter are much more complete (full wavefield with all possible wave phases) than those obtainable by ray tracing (Lecomte et al., 2003, Gjøystdal et al., 2007). The Common Shot Tracer module is used to simulate the marine survey (Figure 4.8). Some key parameters are defined based on the processing report:

- Source depth: 7.5 meters.
- Cable depth: 9 meters
- Streamer parameters: Length 10050 m., Receiver interval 12.5 m, Near offset: 125 m.
- Survey direction: From small to large CDP.

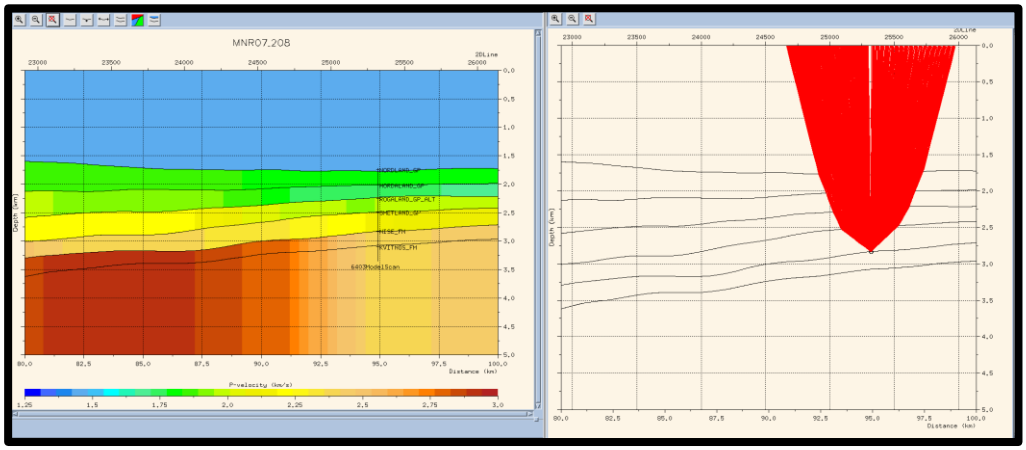

(A)

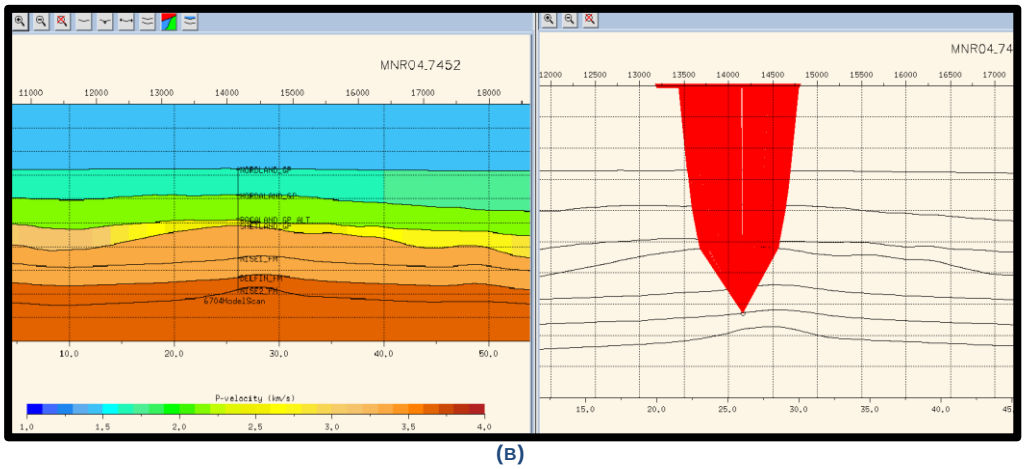

(B)

FIGURE 4. 8 - (A) VØRING BASIN LINE MODEL ZOOMED AROUND WELL POSITION. V_P PROPERTY AND WELL 6704/12-1 POSITION WITH PETROMARKERS ARE DISPLAYED IN THE LEFT. REFLECTION POINT FOR THE SAME POSITION AND TRACED RAYS ARE PLOTTED IN THE RIGHT (B) ZOOMED MØRE BASIN LINE MODEL AROUND WELL POSITION. V_P PROPERTY AND WELL 6403/10-1 POSITION WITH PETROMARKERS ARE DISPLAYED IN THE LEFT. REFLECTION POINT FOR THE SAME POSITION AND TRACED RAYS ARE PLOTTED IN THE RIGHT.

The survey is designed to cover the reflector point which is located at the well position in the target reflector (Top Delfin, sands in the Nise Fm., in Vøring basin line model and Top Nise in Møre basin line model) (see figure 4.8a and 4.8b). Only primary P-P reflections are considered.

4.3 Results

4.3.1 Review of angle ranges used for partial stack sections

As it was presented in the introduction, partial-stack time migrated sections (appendix A) were generated by creating a field of angle-based mute functions for each CMP gather. These functions were then used to define angle band mutes (Table 4.1) which were applied. The resultant angle-muted CMP gather were stacked to produce the partial-stack sections.

TABLE 4. 1 - ANGLE RANGE FOR EACH PARTIAL STACK SECTION

Stack volume	Inner angle (degrees)	Outer angle (degrees)
Near	5	20
Near-Mid	15	30
Far-Mid	25	40
Far	35	50

The angle ranges associated with the partial stack sections are reviewed in this chapter. To do it, offset vs angle, amplitude vs angle and reflectivity vs angle cross-plots are studied for both Vøring and Møre basin line models (Figure 4.9). The relation between offset and angle at the studied reflection point (Figures 4.9a and 4.9b) is linear in the used angle ranges (5° to 50°) for both Vøring and Møre cases. This is due to the lack of abrupt lateral velocity changes and the almost horizontal configuration of the reflectors (Figures 4.8a and 4.8b). In Figures 4.9c and 4.9d, there is a large increase in amplitude after 50°. The amplitude reaches its maximum value around 65° in both cases, which corresponds to the critical angle. Figures 4.9e and 4.9f show that stacking with the selected angle ranges (see table 4.1) is reasonable as the reflectivity trend is kept, i.e.:

- In the Vøring case, there is a continuous decrease of reflectivity with angle. Near, Near-Mid, Far-Mid and Far partial stacks will therefore also show decreasing values.
- In the Møre case, there is a decrease of reflectivity with angle up to 35°. Near, Near-Mid, Far-Mid will show the same trend. After 35°, there is a reflectivity increases that will be detected by the far angle stack (35° to 50°).

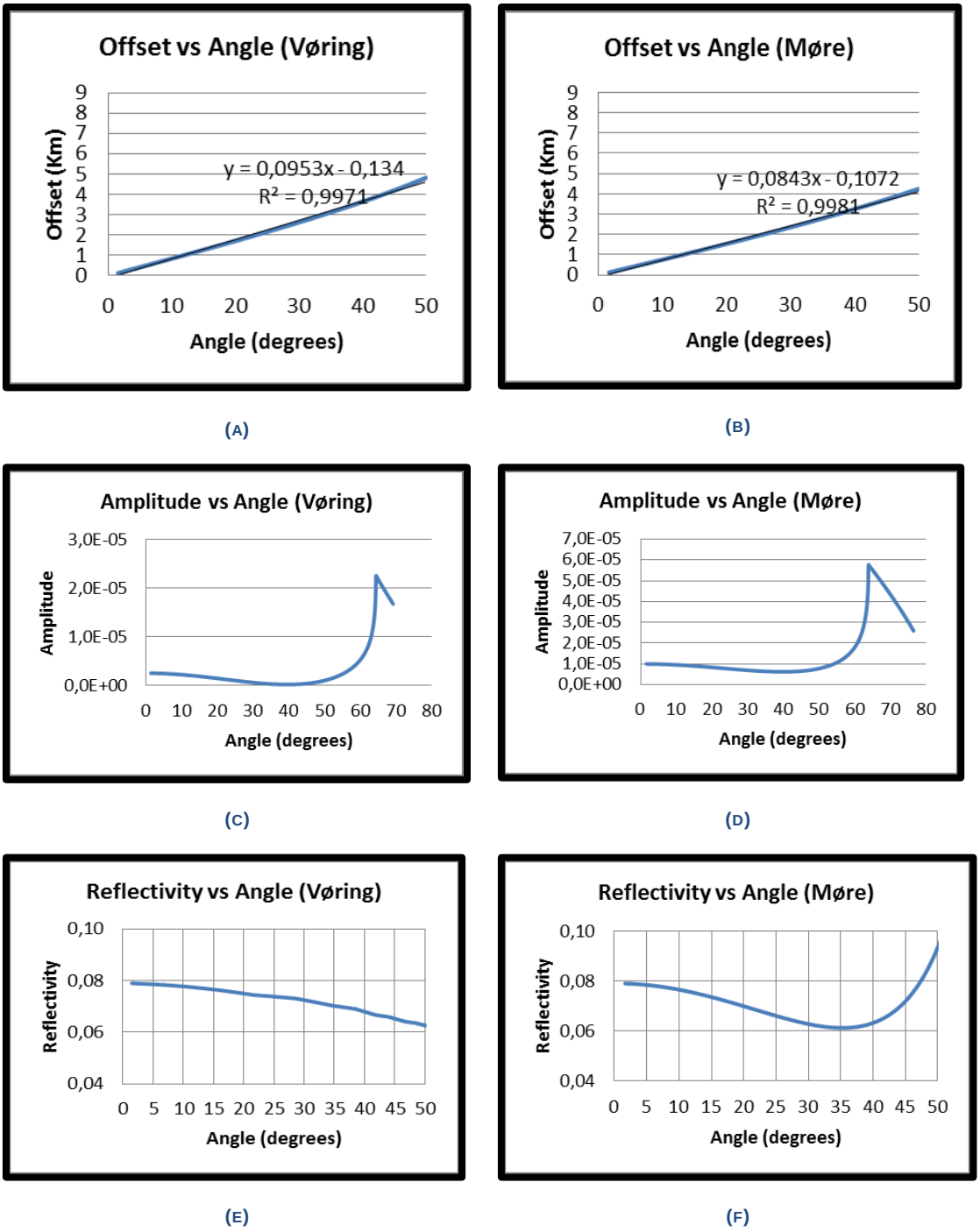

FIGURE 4. 9 - OFFSET VS ANGLE (A), AMPLITUDE VS ANGLE (C) AND REFLECTIVITY VS ANGLE (E) CROSS-PLOTS FOR THE VØRING BASIN LINE MODEL. OFFSET VS ANGLE (B), AMPLITUDE VS ANGLE (D) AND REFLECTIVITY VS ANGLE (F) CROSS-PLOTS FOR THE MØRE BASIN LINE MODEL.

4.3.2 Geometrical spreading

In order to investigate the potential wave-propagation effects which may affect the observed amplitudes, the total effect of geometrical spreading along ray is calculated. Figure 4.10 shows the amplitude variation only due to geometrical spreading versus offset for Vøring

and Møre cases. Møre model shows higher amplitude values and a higher decrease in amplitude with offset due to geometrical spreading than Vøring model.

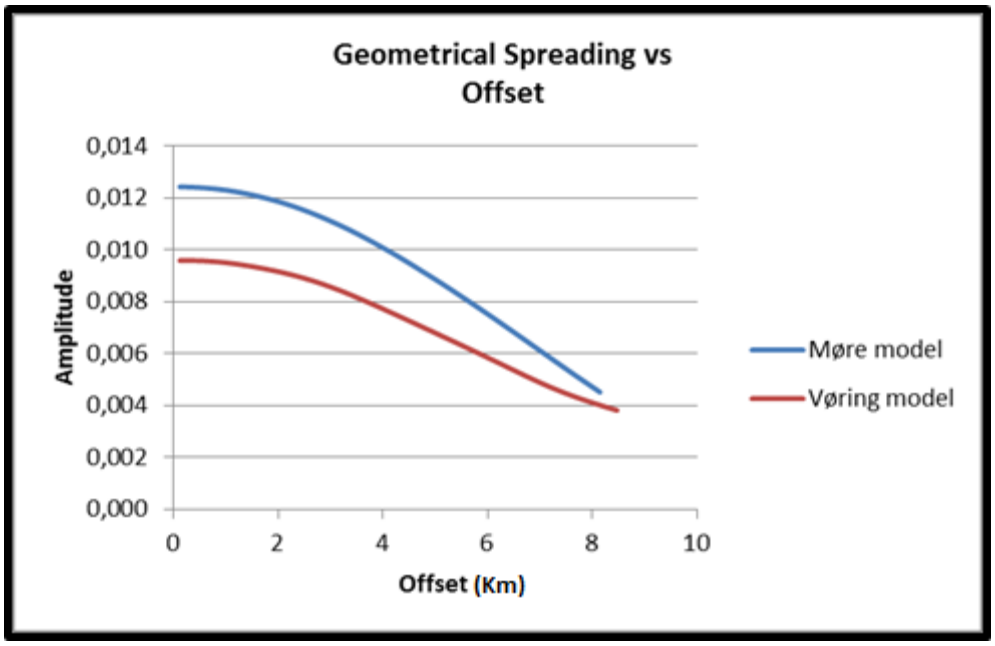

FIGURE 4. 10 - AMPLITUDE VARIATIONS DUE TO GEOMETRICAL SPREADING VS OFFSET FOR VØRING AND MØRE CASES.

4.4 Discussion

The selection of angle ranges (Table 4.1) is appropriate because:

- The offset-angle relation is linear up to 50°.
- The maximum angle (50°) is far from critical angle.
- Figures 4.9e and 4.9f show that partial stack sections based on angle-mutes keep the reflectivity variation trend with angle and should therefore not mask any change in the trend.

In general, amplitude variations in a migrated 3D cube (both in depth or in time) are not only caused by the reflectivity of the subsurface, but also by other effects such as survey layout, transmission/reflection through the overburden, focusing/defocusing and shape of the target reflector (Figure 4.11). Some effects may be removed by processing, but some others, like the overburden or the shape of the target reflector, may remain in the final output (Laurain, 2006). These elements are therefore analysed in both models of the present study:

- Geometrical spreading is a combination of three factors (Cerveny, 2001):
  - Source-Reflector propagation.
  - Reflector-Receiver propagation.
  - Reflector shape.

  In Figure 4.10, as it was expected, the effect of geometrical spreading can be explained by means of raypath length in Vøring and Møre cases: the longer the offset, the longer the raypath and, consequently, the larger the geometrical spreading

effect is. However, in the processing report (confidential), it is mentioned that geometrical spreading is compensated by a gain time function:

$$A_{output}(t) = A_{input}(t)t^{1.5} \quad (4.2)$$

where $A_{output}(t)$ is the amplitude after compensation at time t, $A_{input}(t)$ is the amplitude before compensation at time t and t is the TWT in seconds.

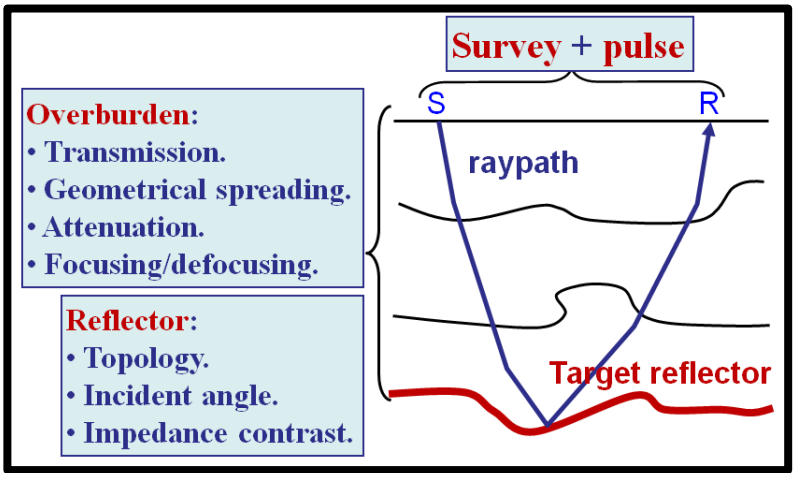

FIGURE 4. 11 - EFFECTS DURING PROPAGATION WHICH MAY CONTRIBUTE TO AMPLITUDE VARIATIONS.

- Intrinsic attenuation is due to the conversion of seismic energy to heat. This attenuation can be measured by the so called quality factor (Q) as:

$$A(t) = A_0 e^{-\omega t/2Q} = A_0 e^{-\pi f t/Q} \quad (4.3)$$

where A(t) is the amplitude at time t, A_0 is the amplitude at t=0, ω is the angular frequency and Q is the quality factor. In the 2D models of the present study, Q is not included because there is not information available. From equation 4.3, if Q is supposed constant, it can be inferred that the higher the frequency, the higher the amplitude decay with time (and/or distance). As a consequence, low frequency content in the frequency spectrum is expected in Far stack sections due to a larger raypath.

- Focusing effect produces a phase shift of π when the wave is propagated through a focus (e.g., focus produced in a syncline). This is true when source and receiver are sufficiently far from the focus (Gelius et al., 1991). NORSAR-2D allows the evaluation of this change in phase by counting the number of times that the ray passed a focus point. In both Vøring and Møre cases the result was zero times, meaning that there is no focusing effect to account for.

According to the analysis, no complex wave propagation effects exist in Vøring and Møre cases. In order to check whether the assumption that amplitude is a scaled version of reflectivity used in AVO modelling, a cross plot amplitude vs reflectivity is analysed in Vøring and Møre cases (Figure 4.12).

In the Vøring Basin case, the amplitude and the reflectivity decrease from 0° until around 50° (Figures 4.9c and 4.9e) and show a linear relation (Figure 4.12a). In the Møre Basin case, the amplitude and the reflectivity decrease with angle until 35° (Figures 4.9d and 4.9f) and they also show a linear relation. From 35 to 50°, however, the amplitude and the reflectivity increase with angle (Figures 4.9d and 4.9f), but they still show a linear relation. These two linear trends are shown in Figure 4.12b. Therefore, the assumption that amplitude is a scaled version of reflectivity used in AVO analysis can be considered valid for both cases.

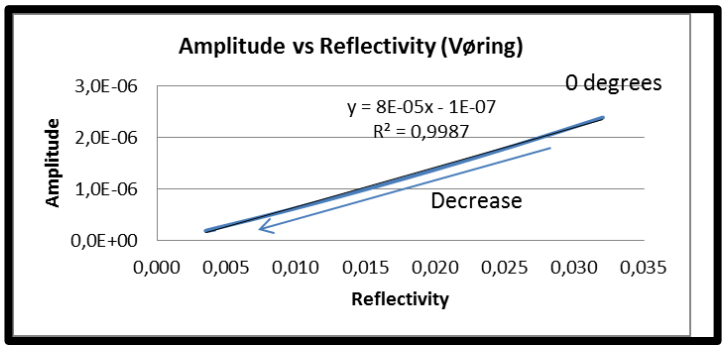

(A)

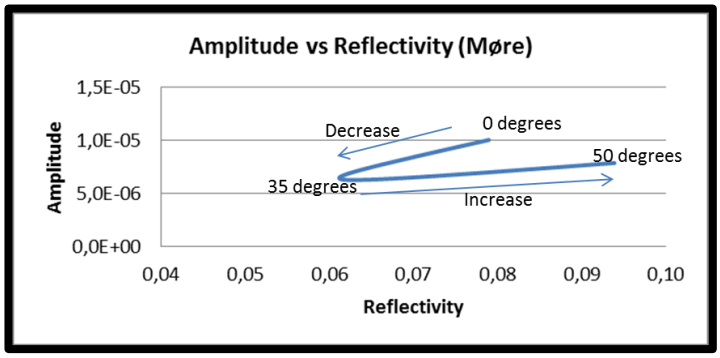

(B)

FIGURE 4. 12 - AMPLITUDE VS REFLECTIVITY FOR VØRING (A) AND MØRE (B) CASES.

Chapter 5: Conclusions

The Nise Fm. and its sand intervals (sometimes so-called Delfin Fm.) represent one of the main Cretaceous reservoirs in the Møre and Vøring Basins. Increments of amplitude with incident angle have been observed in seismic data along Nise Fm., leading to the interpretation of the existence of a reservoir. However, once drilled, the results were very different, some of them discovered hydrocarbons, while in others, no reservoir was found. In this work, four case studies were investigated by modelling to understand the apparent similar seismic responses between the two basins within the same formations, while fluid content and lithology showed to be different: two in the Vøring Basin, with very good quality sandstones but very different gas saturations (Luva discovery (well 6707/10-1) and Gjallar Ridge (well 6704/12-1, with residual gas) and two in the Møre Basin, with no reservoir intervals (Solsikke (well 6403/10-1) and well 6404/11-1).

AVO-AVA forward models (1-D models) were run in each of the cases to study how the variation of elastic properties along the reflector affects the amplitude variation with incident angle. In this part of the study, amplitudes were considered to be a scaled version of reflectivity. The conclusions derived from these synthetic models can be explained by a rearranged version of the three-term Aki-Richards (linearized approximation of the Zoeppritz equation): reflection coefficient (i.e., amplitude) is affected by the acoustic impedance contrast at small incident angles; it is mainly affected by variations in V_p and V_s (i.e. Poisson's ratio) at intermediate incident angles; and it is affected by the variations in V_p at large incident angles.

In the Vøring Basin cases (Gjallar ridge and Luva discovery wells), synthetic models showed that the presence of gas produces negative amplitude in small angles, which becomes more negative when angle increases. The reason is that V_p, Poisson's ratio and density in gas saturated models decrease compared to the brine model whereas V_s is less sensitive to pore fluid. This seismic response was very similar for gas saturations between 50% and 90% in Luva discovery, and between 10% and 20% in Gjallar ridge due to a very similar decrease in V_p velocity and Poisson's ratio. This demonstrates that AVO/AVA analysis will not be able to discriminate between different gas saturations for saturations higher than 10%.

In the Møre Basin cases (Solsikke and 6404/11-1wells), synthetic models showed positive amplitude at zero-offset that, in Solsikke well (flat event) increase with angle, whereas the amplitude remains constant in well 6404/11-1. The reason is an increase in impedance, V_p, V_s and Poisson's ratio in Solsikke well whereas, in well 6404/11-1, there is also an increase in impedance, but a negligible decrease in Poisson's ratio due to a notable increase in V_s compared with V_p.

The comparative analysis between layers above and below the flat events observed in the GWC in Luva discovery (Vøring Basin) and in Solsikke (Møre Basins) demonstrated that there was a higher increase in V_p, density and Poisson's ratio along the transition from gas saturated to water bearing sandstones than through lithology changes. The reason is that V_s

is fluid-insensitive and does not change between gas-saturated sandstones and brine-saturated sandstones (as in Luva discovery), whereas a lithological/diagenetic effect produces changes in V_s (as it might happen in Solsikke well). The consequence in seismic is a higher increase of amplitude with angle in the GWC in Luva discovery than in Solsikke well.

When synthetic models were quantitatively compared with the seismic data, similar seismic response between models and seismic data occurred in Luva discovery and Solsikke, where seismic data was very close to the well location. In Gjallar Ridge, synthetic model and partial stacks showed similar trend in small and intermediate angles, but it was different in large angles (far stack). The reason may be the interference produced by tuning effects due to low frequency content in far stack. The synthetic model in well 6404/11-1, where seismic data was more than 300m away, was not able to replicate the seismic data amplitude variations with angle. The possible causes for the different response can be noise effects (neglected in synthetic model) and wave propagation effects (not considered in 1-D model). Distance between well and seismic data might also have implied small lateral changes in lithology (e.g., small channels or faults) that produced changes of the seismic response.

Two 2D velocity models were built (Gjallar Ridge in Vøring Basin and Solsikke in Møre Basin) and seismic modelling (ray tracing) was used to investigate the assumption that amplitude is a scaled version of reflectivity and to take into account potential complex wave propagation effects. The result showed in both cases that there were no focusing effects and the processing report indicated that geometrical spreading was compensated. Accordingly, reflectivity and amplitude showed a linear relation in these cases and, hence, the assumption in AVO-AVA forward models was considered valid. In addition, the offset-angle relation was found to be linear up to 50° (maximum angle in partial-stack sections), which is interpreted as a consequence of the smooth lateral velocity changes and the almost horizontal configuration of the reflectors around well locations.

For a better understanding of lithological and/or diagenetic changes observed in both Møre and Vøring basins, a proposed future work could include a more detailed rocks physics analysis. This work could focus on defining possible mechanical and/or chemical compaction trends and the transition point between them. If chemical compaction exists, it could be compared with different cementation models.

References

- Aki, K. & Richards, P. G. 2001. *Quantitative seismology*: *Theory and methods*. Sausalito: University Science Books. 700 pp.
- Avseth, P., Mukerji, T. and Mavko, G. and Dvorkin, J. 2005. *Quantitative Seismic Interpretation. Applying Rock Physics Tools to reduce Interpretation Risk*. New York: Cambridge University Press. 340.
- Backus, G. E.1962. Long-wave elastic anisotropy produced by horizontal layering. *J. Geophys. Res.* 67, 4427-4440.
- Batzle, M. and Wang, Z. 1992. Seismic properties of pore fluids. *Geophysics* 57, 1396-1408.
- Blystad, P., Brekke, H., Færseth, R. B., Larsen, B. T., Skogseid, J. and Tørudbakken, B. 1995. *Structural elements of the Norwegian continental shelf. Part II: The Norwegian Sea Region*. NPD-bulletin No 8. Oljedirektoratet, 1-45.
- Brekke, H. 2000. The tectonic evolution of the Norwegian Sea Continental Margin with emphasis on the Vøring and Møre Basins. *In* A. Nøttvedt et al. (eds.). *Dynamics of the Norwegian Margin*. Special Publications, 167. London: Geological Society, 327-378.
- Brekke, H., Dahlgren, S., Nyland, B. and Magnus, C. 1999. The prospectivity of the Vøring and Møre Basins on the Norwegian Sea continental margin. *In* A.J. Fleet and S.A.R. Boldy (eds.). *Petroleum Geology of Northwest Europe.* Proceeding from the 5th Conference. London: Geological Society, 261-274.
- Bukovics, C. and Zieglesr, P. A. 1985. Tectonic development of the Mid-Norway continental margin. *Marine and Petroleum Geology* v 2 (1), 2-22.
- Castagna, J. P., Batzle, M. L and Eastwood, R. L. 1985. Relationships between compressional-wave and shear-wave velocities in clastic silicate rocks. *Geophysics* v 50, 571–581.
- Castagna, J.P. and Swan, H.W. 1997. Principles of AVO crossplotting. *The Leading Edge*, April, 337-342.
- Cerveny, V. 2001. *Seismic Ray Theory*. Cambridge: Cambridge University Press. 724 pp.
- *CWP/SU: Seismic Unix. Colorado School of Mines.* 2012. Available at: http://www.cwp.mines.edu/cwpcodes/ (last access: December 2012).
- Dalland, A., Worsley, D. and Ofstad, K. 1988. A lithostratigrafic scheme for the Mesozoic and Cenozoic succession offshore mid- and northern Norway. NPD-bulletin No 4. Oljedirektoratet, 65 pp.
- Doré, A. G. and Lundin, E. R. 1996. Cenozoic compressional structures on the NE Atlantic margin; nature, origin and potential significance for hydrocarbon exploration. *Petroleum Geoscience* v 2 (4), 299-311.

- Doré, A. G., Lundin, E. R., Fichler, C. and Olesen, O. 1997. Patterns of basement structure and reactivation along the NE Atlantic margin. *Journal of the Geological Society* 154, 85-92.
- Fjellanger, E., Surlyk, F., Wamsteeker, L. C. and Midtun, T. 2005. Upper cretaceous Basin-floor fans in the Vøring Basin, Mid Norway shelf. *In* Bjørn T.G Wandås, J. P. N. E. E. & Felix, G. (eds.) *Norwegian Petroleum Society Special Publications*. Volume 12. Elsevier, 135-164.
- Fugelli, E. M. G. and Olsen, T. R. 2005. Screening for deep-marine reservoirs in frontier Basins: Part 1—Examples from offshore mid-Norway. *AAPG Bulletin* 89, 853-882.
- Færseth, R. B. and Lien, T. 2002. Cretaceous evolution in the Norwegian Sea—a period characterized by tectonic quiescence. *Marine and Petroleum Geology* 19, 1005-1027.
- Gardner, G.H.F., Gardner, L.W. and Gregory, A.R. 1974. Formation velocity and density – the diagnostic basics for stratigraphic traps. *Geophysics* v 39, 770-780.
- Gassmann, F. 1951. Elastic waves through a packing of spheres. *Geophysics v* 16**,** 673-685.
- Gelfand, V., Ng, P., Nguyen, H. and Larner, K. 1986. Seismic Lithologic Modeling of Amplitude-versus-offset Data. *Society of Exploration Geophysicist: proceedings of the 56th Annual Meeting.* Houston, Nov. 2-6, 1986, p. 334-336.
- Gelius, L.J. and Johansen, T. 2010. *Petroleum Geophysics*. Bergen: UniGEO as. 660 pp.
- Gelius, L.J., Stamnes, J. and Heier, H .1991. Pulse distortion in caustic regions. *Geophysical Prospecting*. ISSN 0016-8025. 39, 51- 59.
- Gjøystdal, H., Iversen, E., Lecomte, I., Kaschwish, T., Drottning, Å. and Mispel, J. 2007. Improved applicability of ray tracing in seismic acquisition, imaging, and interpretation. *Geophysics* v 72 (5), SM261-SM271.
- Greenberg, M.L. and Castagna, J.P. 1992. Shear-wave velocity estimation in porous rocks: Theoretical formulation, preliminary verification and applications. *Geophysical prospecting* v 40 (2), 195-209.
- Hampson-Russell manual, version 9.1.2.
- Hashin, Z., and Shtrikman, S. 1963. A variational approach to the elastic behavior of multiphase minerals. *J. Mech. Phys. Solids* 11, 127-140.
- Hill, R. 1963. Elastic properties of reinforced solids: Some theoretical principles. *Journal of the Mechanics and Physics of Solids* 11 (5), 357-372.
- Hubral, P. Krey, T. and Larner, K. L. 1980. *Interval velocities from seismic reflection time measurement.* Society of Exploration Geophysicists. 203 pp.
- Koch, J. O. and Heum, O. R. 1995. Exploration trends of the Halten Terrace. *In* Hanslien, S. (eds.) *Norwegian Petroleum Society Special Publications*, 4. Amsterdam: Elsevier. 235-251.
- Laurain, R. 2006. *Simulation and correction of amplitude anomalies in 3D seismic data*. PhD. Faculty of Mathematics and Natural Science, University of Oslo. 112 pp.

- Lecomte, I., Gjøystdal, H., Drottning, Å., Maaø, F., Johansen, T., and Bakke, R. 2004. Efficient and flexible seismic modeling of reservoirs: A hybrid approach. *The Leading Edge* 23 (5), 432-437.
- Mavko, G., Mukerji, T., and Dvorkin, J. 2003. The *Rock Physics Handbook: Tools for seismic analysis in porous media*. Cambrige: Cambridge University Press. 329 pp.
- Morton, A. C. and Grant, S. 1998. Cretaceous depositional systems in the Norwegian Sea; heavy mineral constraints. *AAPG Bulletin* 82, 274-290.
- NORSAR. NORSAR 2D ray modelling - User's guide, version 5.1, 2011.
- Norwegian Petroleum Directorate (NPD). 2012. *Factmaps* . Available at: http://www.npd.no/en/Maps/Fact-maps/ (last access: December 2012)
- Norwegian Petroleum Directorate (NPD). 2012. *Factpages.* Available at: http://factpages.npd.no/factpages/ (last access: December 2012)
- Ostrander, W.J. 1984. Plane wave reflection coefficients for gas sands at non normal angles of incidence. *Geophysics* 49 (10), 1637-1648.
- Reuss, A. 1929. Berechnung der Fließgrenze von Mischkristallen auf Grund der Plastizitätsbedingung für Einkristalle. *Journal of Applied Mathematics and Mechanics* 9 (1), 49–58.
- Ross, C. P., and Kinman, D. L. 1995. Nonbright spot AVO; Two Examples. *Geophysics* v 60 (5), 1398-1408.
- Rutherford S. R. and Williams R. H. 1989. Amplitude versus offset variation in gas sands. *Geophysics* v 54, 680-688.
- Shuey, R.T. 1985. A simplification of the Zoeppritz equations. *Geophysics* v 50 (4), 609–614.
- Voigt, W., 1910. Lehrbuch der Kristallphysik, Leipzig.
- Wood, A. W. 1955. *A Textbook of Sound.* NewYork: The MacMillan Co. 360 pp.
- Zoeppritz, K. 1919. Erdbebenwellen VIIIB, On the reflection and propagation of seismic waves *through unstable layers*. Göttinger Nachr (I), 66–84.

List of Figures

Figure 1. 1 - Vøring and northern Møre Basins with the main geological features. Locations of wells used in this report are identified with a red star (modified from Norwegian Petroleum Directorate – NPD- Factmaps). 1
Figure 1. 2 - Picked amplitudes in partial-stack sections: Near stack, Near/Mid stack, Far/Mid stack, Far stack. 3
Figure 1. 3 - Wells and seismic lines locations superimposed on the main geological features. 4
Figure 2. 1 - Main structural elements in Norwegian Sea Continental Shelf. Main structures are highlighted. Area in the box is zoomed in Figure 2. Figure modified after Brekke (2000). 8
Figure 2. 2 - Vøring Basin structural evolution. Structures referred in the text are numbered. Figure modified after Fjellanger et al. (2005) 10
Figure 2. 3 - Vøring Basin stratigraphy (Cretaceous-Cenozoic). Lysing Fm, Nise Fm and Springar Fm act as reservoirs and Spekk Fm as possible source rock. Figure modified after Fjellanger et al. (2005) 11
Figure 2. 4 - Campanian paleogeography of the Vøring Basin showing a basin-floor fan system deposited in the deep basin through submarine canyons. Greenland continental shelf. After Fjellanger et al. (2005). 13
Figure 3. 1 - Density correction in well 6404/11-1 15
Figure 3. 2 - Greenberg-Castagna derived curve (orange) and real data (purple). They match in the ellipse. 16
Figure 3. 3 - Vp/Vs crossplot for well 6403/10-1. Linear regression is computed and displayed for the Springer Fm. and the Nise Fm. 16
Figure 3. 4 - V_s calculation for well 6404/11-1. Note how regression (orange) and Greenberg-Castagna (purple) derivations fit in Springar Fm. and Nise Fm 16
Figure 3. 5 - Gjallar Ridge well (6704/12-1) Vsh estimation. GR log is divided into zones based on formations. For each zone, GR_{max} and GR_{min} are defined and V_{sh} is computed. 17
Figure 3. 6 - Gjallar Ridge well (6704/12-1) check-shot correction. Drift curve (centre) is interpolated to show the difference between the time-depth curve log and check-shot data. Time-depth curve (left) and Sonic/ V_p (right) logs are corrected using the drift curve. 18
Figure 3. 7 - Wavelet extracted from Solsikke well (6403/10-1) and seismic line MNR07-208. (3.7a) wavelet length is 150 ms and a constant-phase method is selected. (3.7b) Extracted wavelet with a dominant frequency around 25 Hz. 19
Figure 3. 8 - Well correlation for Solsikke well (6403) and seismic line MNR07-208 showing a correlation of 0.6 in the target zone. 19
Figure 3. 9 - Gamma Ray, density, V_p, V_s, Resistivity and Neutron Porosity from Luva discovery well (6707/10-1) composite log. Poisson's Ratio, P-Impedance and P-Reflectivity are calculated. Area of interest between the Delfin (informal) Fm. top and base of the reservoir is highlighted. 23

Figure 3. 10 - Elastic properties (V_p, V_s, density and Poisson's ratio) from Luva discovery well (6707/10-1) displayed together with wiggled traces for pure brine , 90% gas-10% brine (in-situ fluid saturation), 70% gas-30% brine, and 50% gas-50% brine scenarios 23
Figure 3. 11 - Elastic properties (V_p, V_s, density and Poisson's ratio) from Luva discovery well (6707/10-1) displayed together with wiggled traces for pure brine , 90% gas-10% brine (in-situ fluid saturation), 70% gas-30% brine, and 50% gas-50% brine scenarios 25
Figure 3. 12 - Gamma Ray, density, V_p, V_s, Resistivity and Neutron Porosity from Gjallar Ridge well (6704/12-1) composite log. Poisson's Ratio, P-Impedance and P-Reflectivity are calculated. Area of interest between Delfin (informal) FM top and Nise 2 FM 2 is highlighted. 26
Figure 3. 13 - Elastic properties (V_p, V_s, density and Poisson's ratio) from Gjallar Ridge well (6704/12-1) displayed together with wiggled traces for pure brine , 5% gas-95% brine, 10% gas-90% brine (in-situ fluid saturation) and 20% gas-80% brine scenarios. 26
Figure 3. 14 - Amplitude vs incident-angle in Gjallar Ridge well (6704/12-1) for pure brine, 10% gas-90% brine (in-situ fluid saturation), 20% gas-80% brine, and 30% gas-70% brine scenarios. 27
Figure 3. 15 - Gamma Ray, density, V_p, V_s, Resistivity and Neutron Porosity from Solsikke well (6403/10-1) composite log. Poisson's Ratio, P-Impedance and P-Reflectivity are calculated. Area of interest between Nise Fm. top and Kvitnos Fm. top is highlighted. 28
Figure 3. 16 - P-impedance and Poisson's ratio in Solsikke well (6403/10-1) are displayed for blocking of 25 meters. Synthetic seismic traces for angles between 0 and 50 are also displayed for blocking of 25 meters. 29
Figure 3. 17 - Amplitude vs incident angle variation in Solsikke well (6403/10-1) and Luva discovery well (6707/10-1). 30
Figure 3. 18 - Gamma Ray, density, V_p, V_s, Resistivity and Neutron Porosity from well 6404/11-1 composite log. Poisson's Ratio, P-Impedance and P-Reflectivity are calculated. Area of interest between Nise Fm. top and 3600 meters is highlighted. 31
Figure 3. 19 - P-impedance and Poisson's ration are displayed for blocking of 26 meters. Synthetic seismic traces for angles between 0 and 50 are also displayed. 31
Figure 3. 20 - Amplitude vs angle variation in Well 6404/11-1 with block 25m and well 6707/10-1 32
Figure 3. 21 - (a) V_p vs Poisson´s ratio and (b) V_s vs Poisson´s ratio (Luva gas discovery). Both depth colour coded. 34
Figure 3. 22 - (a) V_p vs Poisson´s ratio and (b) V_s vs Poisson´s ratio (Gjallar Ridge, marginally gas saturated sand case). Both depth colour coded. 35
Figure 3. 23 – (a) Amplitude variation with incident angle in synthetic models and (b) Picked amplitudes in partial stack data (near, Near/Mid, Far/Mid, Far) 38
Figure 4. 1 - Schematic representation of dynamic ray tracing (NORSAR-2D manual) 41
Figure 4. 2 - Interpretation of seismic line MNR04-7452 around Gjallar Ridge well (6704/12-1, sands with marginal gas). The Delfin horizon (dark green at about 3800 ms) is the target in the study. 43
Figure 4. 3 - Interpretation of seismic line MNR07-208 around Solsikke well (6403/10-1, no sand). The Nise horizon (red) is the target in this study. 44

Figure 4. 4 - Cube showing the area definition for the project. Line MNR04-7452 and well 6704/12-1 (Vøring Basin line model) in the north and line MNR07-208 and well 6403/10-1 (Møre Basin line model) in the south. 44
Figure 4. 5 - Vøring Basin line model calibration, showing V_p, V_s and density extracted from the model and from well 6704/12-1 (sands with marginal gas) check-shot and wire log. V_s for the model and check-shot log is derived by Mudrock line equation. 48
Figure 4. 6 - Møre Basin line model calibration, showing V_p, V_s and density extracted from the model and from well 6403/10-1 (no sand) check-shot and wire log. V_s for the model and check-shot log is derived by Greenberg-Castagna (1992) empirical relation. 48
Figure 4. 7 - (a) Vøring-basin 2D model (seismic line MNR04-7452 and well 6704/12-1; sands with marginal gas). (b) Møre-basin 2D model (seismic line MNR07-208 around well 6403/10-1; no sand). Note that the vertical scale (depth) is exaggerated (vertical/horizontal = 5) for a better display. 49
Figure 4. 8 - (a) Vøring basin line model zoomed around well position. V_p property and well 6704/12-1 position with petromarkers are displayed in the left. Reflection point for the same position and traced rays are plotted in the right (b) Zoomed Møre basin line model around well position. V_p property and well 6403/10-1 position with petromarkers are displayed in the left. Reflection point for the same position and traced rays are plotted in the right. 50
Figure 4. 9 - Offset vs angle (a), amplitude vs angle (c) and reflectivity vs angle (e) cross-plots for the Vøring basin line model. Offset vs angle (b), amplitude vs angle (d) and reflectivity vs angle (f) cross-plots for the Møre basin line model. 52
Figure 4. 10 - Amplitude variations due to geometrical spreading vs offset for Vøring and Møre cases. 53
Figure 4. 11 - Effects during propagation which may contribute to amplitude variations. 54
Figure 4. 12 - Amplitude vs Reflectivity for Vøring (a) and Møre (b) cases. 55
Figure A. 1 - Luva gas discovery. Full Stack cross section in cube BPN9601 at well position. 67
Figure A. 2 - Gjallar Ridge well and line MNR04-7452 Full Stack section 68
Figure A. 3 - Solsikke well and line MNR07-208 Full stack section 68
Figure A. 4 - 6404/11-1 well and line MNR06-7124 Full stack section 69
Figure A. 5 - Luva gas discovery. Seismic shows bright amplitudes in large angle (far angle). 69
Figure A. 6 - Gjallar Ridge well and line MNR04-7452. Near, near-mid, far-mid and far partial stack sections are displayed. Picked traces to measure amplitudes are marked by horizontal red lines in the interpreted horizon (top study case). 70
Figure A. 7 - Solsikke well and line MNR07-208. Near, near-mid, far-mid and far partial stack sections are displayed. Picked traces to measure amplitudes are marked by horizontal red lines in the interpreted horizon (top study case). 70
Figure A. 8 - 6404/11-1 well and line MNR06-7124. Near, near-mid, far-mid and far partial stack sections are displayed. Picked traces to measure amplitudes are marked by horizontal red lines in the interpreted horizon (top study case). 71
Figure B. 1 - Reflection and transmission between two elastic media. After Avseth et al, 2005. 72

Figure B. 2 - P-wave normal incident between two elastic media, where ρ, V_p and Z are density, p-wave velocity and impedance respectively. 74
Figure B. 3 - AVO Class classification. After Castagna et alt 1997 79
Figure C. 1 - Seismic cube BPN9601 and well 6707/10-1 (Luva gas discovery) correlation. The correlation is 0.86, showing a very good match between synthetic traces and actual seismic data. 80
Figure C. 2 - Seismic line MNR04-7452 and well 6704/12-1 (Gjallar Ridge) correlation. The correlation is 0.69, showing a good match between synthetic traces and actual seismic data in the target area (between yellow horizontal lines)..... 80
Figure C. 3 - Seismic line MNR07-208 and well 6403/10-1 (Solsikke) correlation. The correlation is 0.61, showing a good match between synthetic traces and actual seismic data in the target area (between yellow horizontal lines)..... 81
Figure C. 4 - Seismic line MNR06-7124 and well 6404/11-1 correlation. The correlation is 0.51, showing the poorest match between synthetic traces and actual seismic data. However, given that the distance between the line and the well is around 325 m, this correlation is considered good enough..... 81
Figure D. 1 - Interpreted flat event in Luva gas discovery due to gas-water contact (Vøring Basin). 82
Figure D. 2 - Interpreted flat event in Solsikke well (Møre Basin). Displayed line is 3002 to better show the event..... 82
Figure D. 3 - Interpreted flat event in Solsikke discovery (Møre Basin). MNR07-208 far stack section (left) is compared with line is 3002 (right) to show the match between the two sections. Flat event is interpreted at around 3560 ms. 83
Figure F. 1 - NORSAR-2D velocity estimator..... 87
Figure F. 2 - Depth conversion..... 88
Figure Gl. 1 - Seismic model example. Seismic line MNR07-208..... 91

List of Tables

Table 1. 1 – Angle range for each partial stack section 5
Table 1. 2 – Well/Seismic line relation. Well position (well projection on the line) and well/Seismic line distance. 5
Table 3. 1 – Upscalling block sizes based on Tuning thickness. 20
Table 3. 2 – Depth intervals for target formations (Nise FM. in Møre Basin and Delfin Fm. in Vøring Basin) 21
Table 3. 3 – Quartz and clay Density (ρ), Bulk (K) and Shear (μ) modulus 21
Table 3. 4 - Brine and Gas Density (ρ) and Bulk (K) modulus 22
Table 3. 5 – V_p, V_s, Density and Poisson's Ratio in overburden layer and in reservoir for different pore saturations (Luva discovery) 24
Table 3. 6 - V_p, V_s, Density and Poisson's Ratio percentage variation for the modelled gas saturations with respect to the brine case (Luva discovery) 24
Table 3. 7 - V_p, V_s, Density and Poisson's Ratio in overburden layer and in reservoir for different pore saturations (Gjallar Ridge) 27
Table 3. 8 - V_p, V_s, Density and Poisson's Ratio percentage variation for the modelled gas saturations with respect to the brine case (Gjallar Ridge) 27
Table 3. 9 - V_p, V_s, Density and Poisson's Ratio above and below flat events observed at the reservoir base of Luva gas discovery well (6707/10-1) and at Solsikke well (6403/10-1) 29
Table 3. 10 - V_p, V_s, Density and Poisson's Ratio variations along the flat event in Luva gas discovery (6707/10-1) and in Solsikke well (6403/10-1) 30
Table 3. 11 - V_p, V_s, Density and Poisson's Ratio above and below positive reflector observed in well 6404/11-1 32
Table 3. 12 - V_p, V_s, Density and Poisson's Ratio variations along the positive reflector in well 6404/11-1 32
Table 3. 13 - V_p, V_s, Density and Poisson's Ratio variations along top reflectors in Luva gas discovery (6707/10-1) and Gjallar Ridge (6704/12-1) 35
Table 4. 1 - Angle range for each partial stack section 51
Table A. 1 – Picked amplitudes in partial stack sections 71
Table B. 1 – Effective medium models 77
Table E. 1 - V_P, V_S, Density and Poisson's ratio in overburden layer and in reservoir for in-situ case (Luva Discovery) 84
Table E. 2 - V_P, V_S, Density and Poisson's ratio variation and average between overburden layer and reservoir for in-situ case (Luva Discovery) 84
Table E. 3 - Rp, G and F coefficients in top reservoir (Luva Discovery) 84
Table E. 4 - V_P, V_S, Density and Poisson's ratio in reservoir and layer below for in-situ case (Luva Discovery) 84
Table E. 5 - V_P, V_S, Density and Poisson's ratio variation and average between reservoir and layer below for in-situ case (Luva Discovery) 84
Table E. 6 - Rp, G and F coefficients in base reservoir (Luva Discovery) 84

Table E. 7 - V_P, V_S, Density and Poisson's ratio in overburden layer and in reservoir for in-situ case (Gjallar Ridge) 85
Table E. 8 - V_P, V_S, Density and Poisson's ratio variation and average between overburden layer and reservoir for in-situ case (Gjallar Ridge) 85
Table E. 9 - Rp, G and F coefficients in top reservoir (Luva Discovery) 85
Table E. 10 - V_P, V_S, Density and Poisson's ratio in layers above and below the flat event (Solsikke) 85
Table E. 11 - V_P, V_S, Density and Poisson's ratio variation and average between layers above and below the flat event (Solsikke) 85
Table E. 12 - Rp, G and F coefficients in flat event (Solsikke) 85
Table E. 13 - V_P, V_S, Density and Poisson's ratio in layers above and below the reflector (6404/11-1) 86
Table E. 14 - V_P, V_S, Density and Poisson's ratio variation and average between layers above and below the reflector (6404/11-1) 86
Table E. 15 - Rp, G and F coefficients in reflector (6404/11-1) 86

Appendix

Appendix A: Full stack and Observed variation in partial stacks

This appendix presents the seismic data available:

- Full stack sections with interpreted horizons.
- Partial stack sections, in which variation in amplitudes between small and large incident angles is observed.

Full stack sections

Well 6707/10-1 (Nyk High) – Luva gas discovery

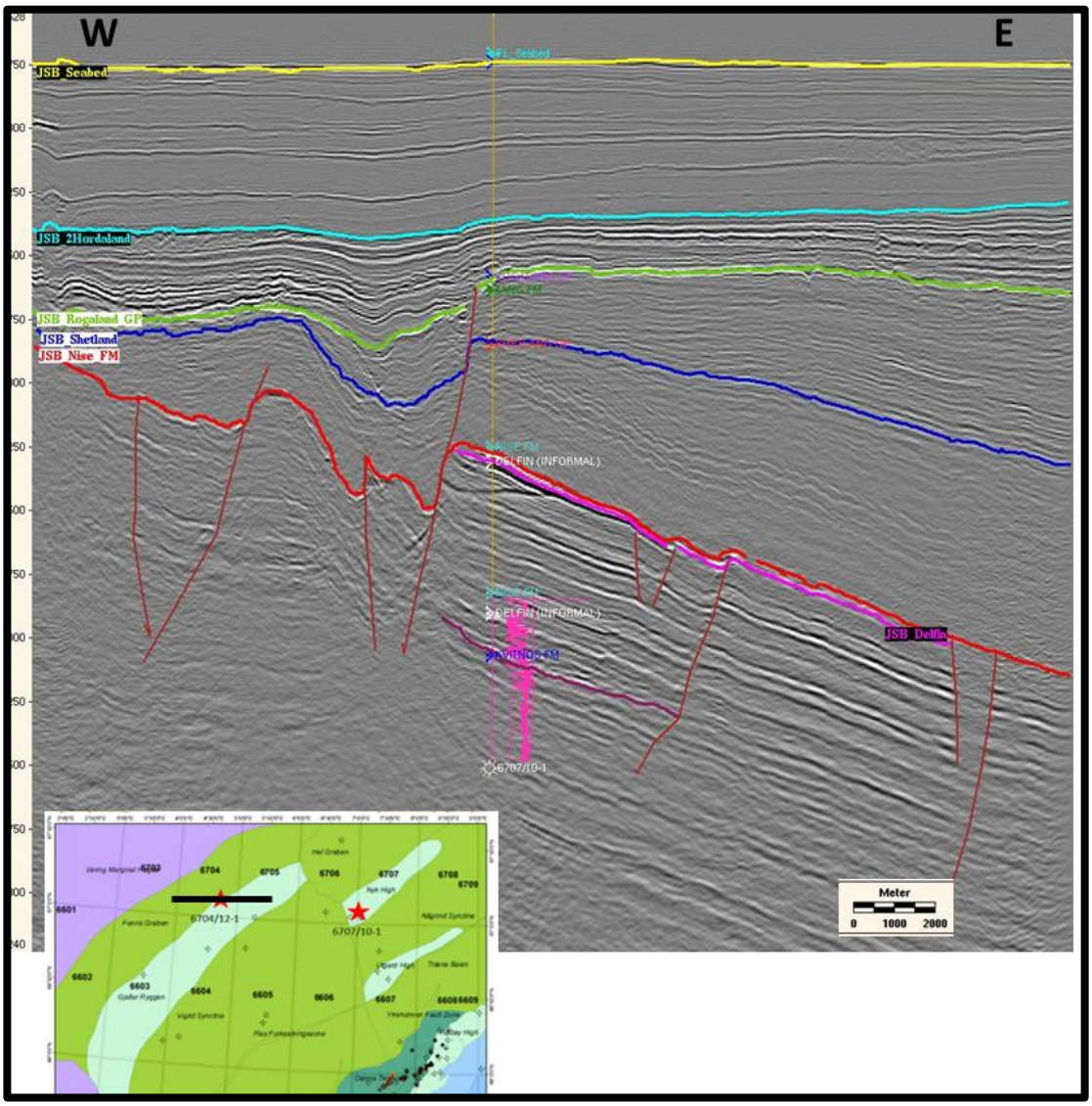

FIGURE A. 1 - LUVA GAS DISCOVERY. FULL STACK CROSS SECTION IN CUBE BPN9601 AT WELL POSITION.

Well 6704/12-1 (Gjallar Ridge) – Marginally gas saturated sand

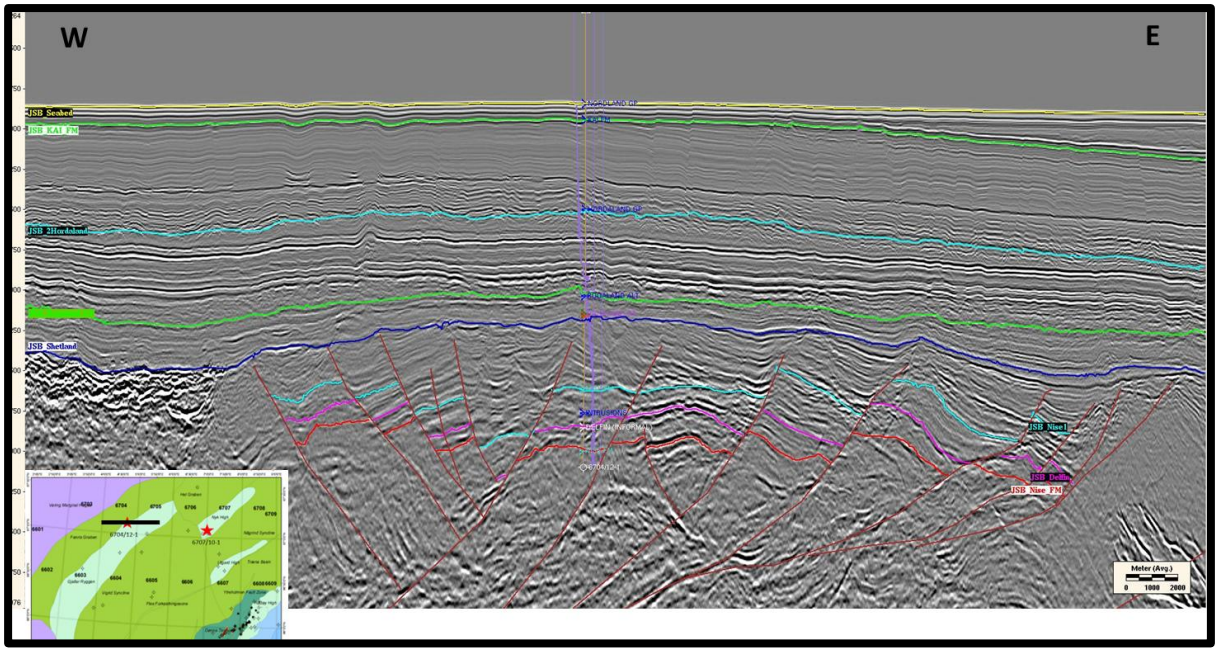

FIGURE A. 2 - GJALLAR RIDGE WELL AND LINE MNR04-7452 FULL STACK SECTION

Well 6403/10-1 (Solsikke) – Flat lithological event

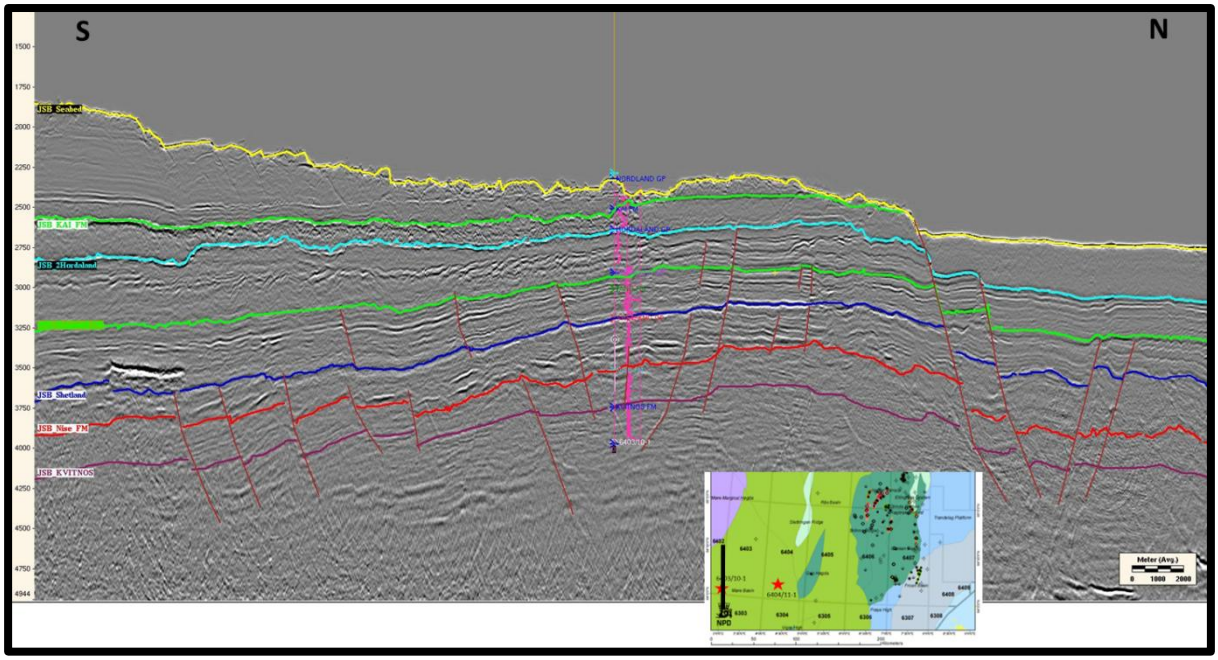

FIGURE A. 3 - SOLSIKKE WELL AND LINE MNR07-208 FULL STACK SECTION

Well 6404/11-1 – No-sand reservoir

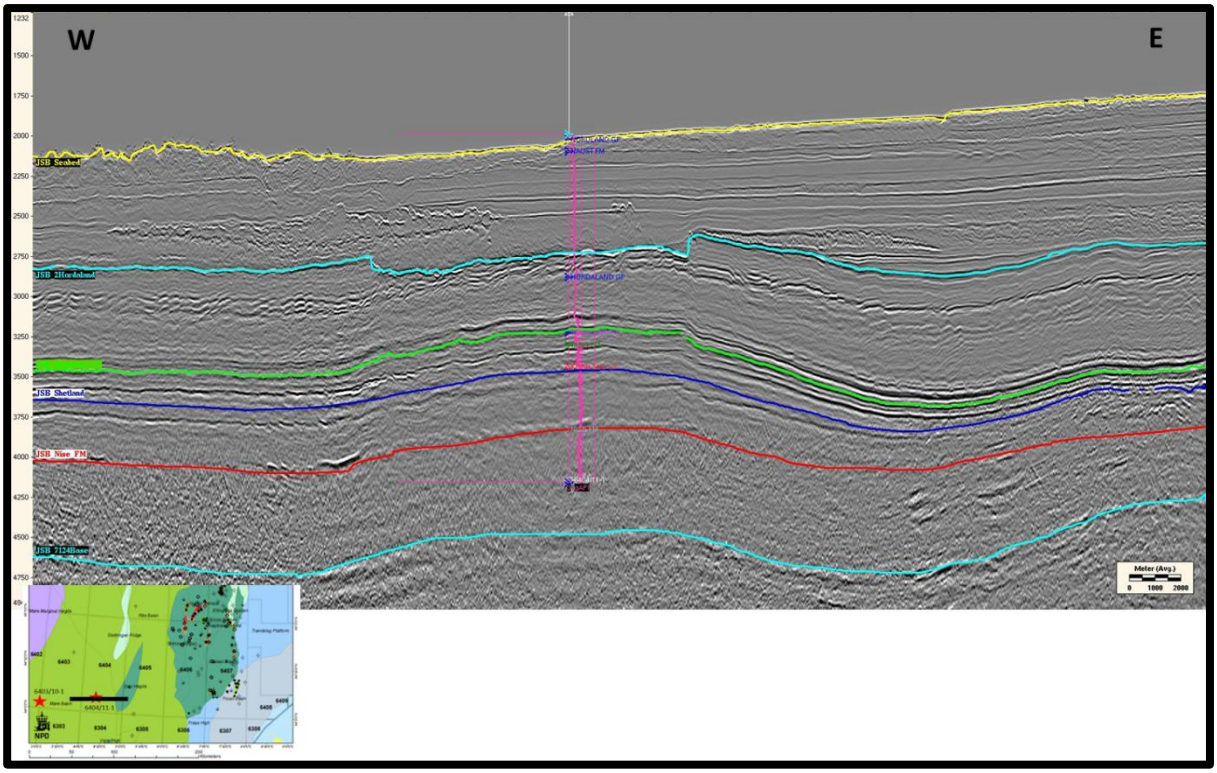

FIGURE A. 4 - 6404/11-1 WELL AND LINE MNR06-7124 FULL STACK SECTION

Partial Stack sections

Well 6707/10-1 (Nyk High) – Luva gas discovery

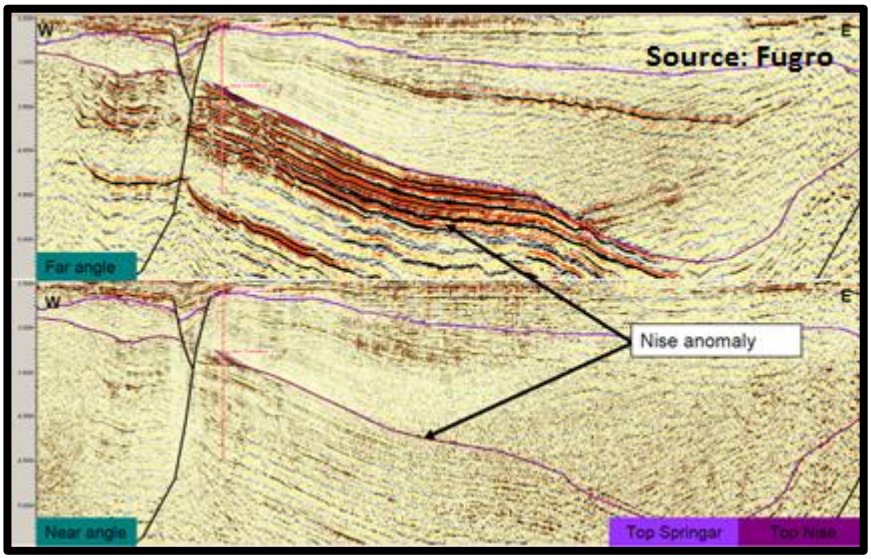

FIGURE A. 5 - LUVA GAS DISCOVERY. SEISMIC SHOWS BRIGHT AMPLITUDES IN LARGE ANGLE (FAR ANGLE).

Well 6704/12-1 (Gjallar Ridge) – Marginally gas saturated sand

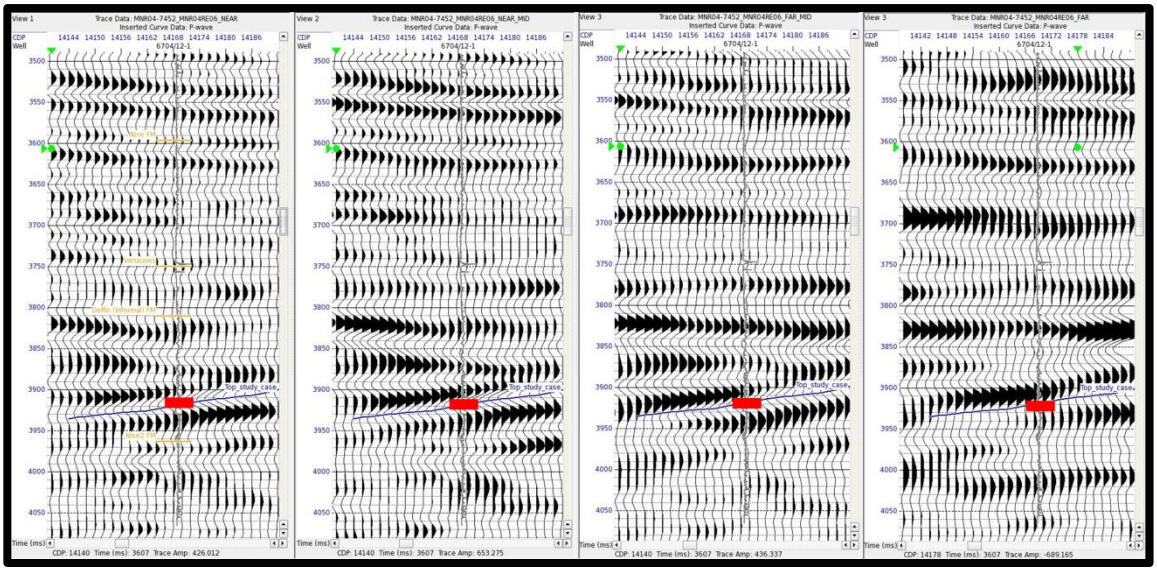

FIGURE A. 6 - GJALLAR RIDGE WELL AND LINE MNR04-7452. NEAR, NEAR-MID, FAR-MID AND FAR PARTIAL STACK SECTIONS ARE DISPLAYED. PICKED TRACES TO MEASURE AMPLITUDES ARE MARKED BY HORIZONTAL RED LINES IN THE INTERPRETED HORIZON (TOP STUDY CASE).

Well 6403/10-1 (Solsikke) – Flat lithological event

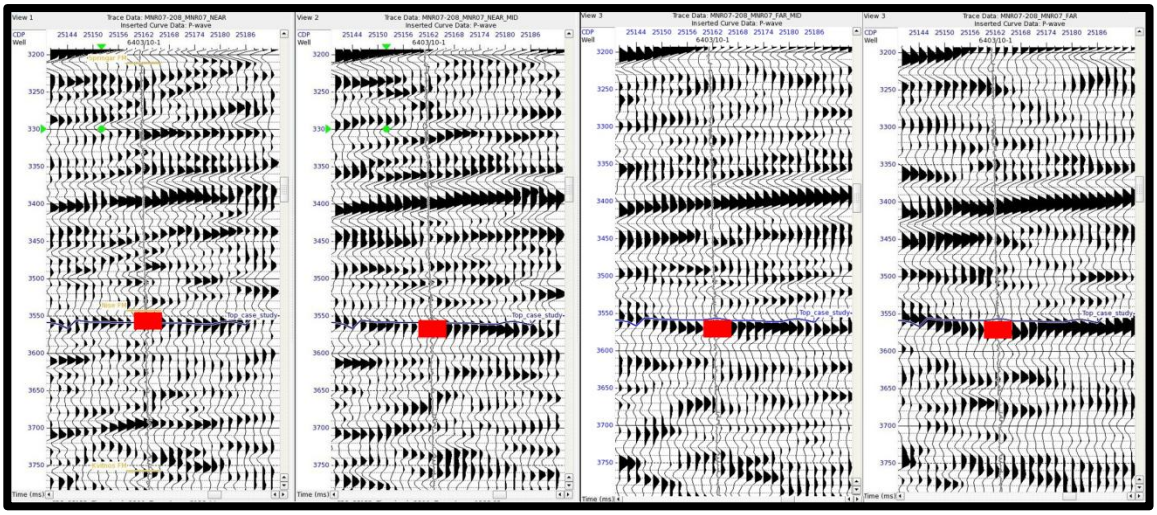

FIGURE A. 7 - SOLSIKKE WELL AND LINE MNR07-208. NEAR, NEAR-MID, FAR-MID AND FAR PARTIAL STACK SECTIONS ARE DISPLAYED. PICKED TRACES TO MEASURE AMPLITUDES ARE MARKED BY HORIZONTAL RED LINES IN THE INTERPRETED HORIZON (TOP STUDY CASE).

Well 6404/11-1 – No-sand reservoir

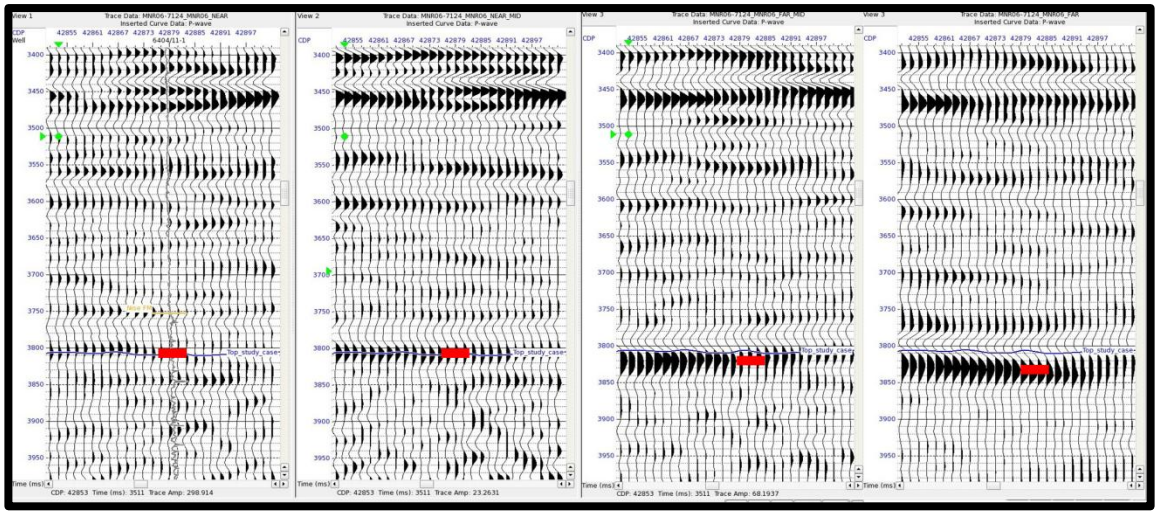

FIGURE A. 8 - 6404/11-1 WELL AND LINE MNR06-7124. NEAR, NEAR-MID, FAR-MID AND FAR PARTIAL STACK SECTIONS ARE DISPLAYED. PICKED TRACES TO MEASURE AMPLITUDES ARE MARKED BY HORIZONTAL RED LINES IN THE INTERPRETED HORIZON (TOP STUDY CASE).

Amplitudes at picked points in seismic events

In Table A.1, picked amplitudes in interpreted horizons where partial stack sections are available are shown. The area which was picked is marked by a red horizontal line in Figures A.6, A.7 and A.8. In Table A.1, negative amplitudes in Gjallar Ridge well show an increment (in absolute value) in partial stacks covering mid and mid-far angles, but in far angle stack the amplitude drops. Positive amplitudes in 6403/10-1 (Solsikke) and 6404/11-1 (No-sand reservoir) wells show an increment for partial stack sections covering large angles.

TABLE A. 1 – PICKED AMPLITUDES IN PARTIAL STACK SECTIONS

	Near	Near/mid	Far/Mid	Far
6704/12-1 (Gjallar Ridge)	-1403	-1413	-1630	-463
6403/10-1 (Solsikke)	1720	1885	1867	2192
6404/11-1 (No-sand reservoir)	194	586	603	1365

Appendix B: AVO-AVA theoretical framework

Reflection coefficient: variation with incident angle

When a plane P-wave incidents at the interface between two elastic mediums (layer 1, with density ρ_1, P-velocity V_{p1} and S-velocity V_{s1}, and layer 2 with density ρ_2, P-velocity V_{p2} and S-velocity V_{s2}) with an angle $\theta>0$, reflected and transmitted P- and SV-waves are generated (mode conversion) (Figure B.1). In the case of normal incidence ($\theta=0$), only P-waves are generated.

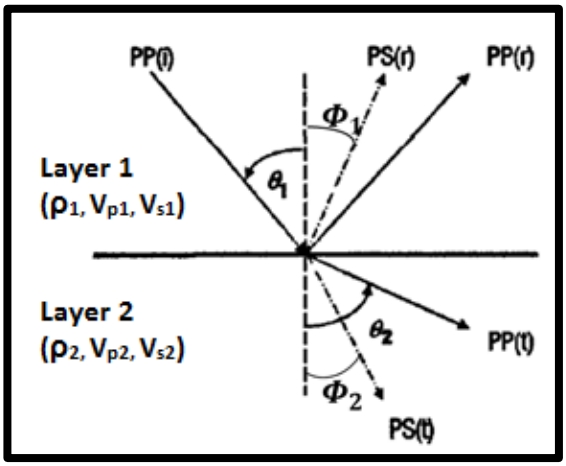

FIGURE B. 1 - REFLECTION AND TRANSMISSION BETWEEN TWO ELASTIC MEDIA. AFTER AVSETH ET AL, 2005.

The relation between incident, reflected and transmitted angles is given by Snell's law.

$$p = \frac{\sin\theta_1}{V_{p1}} = \frac{\sin\theta_2}{V_{p2}} = \frac{\sin\Phi_1}{V_{s1}} = \frac{\sin\Phi_2}{V_{s2}} = constant \qquad \text{(B. 1)}$$

Where p is the ray parameter.

Zoeppritz equations (Zoeppritz, 1919) describe the variation of P-P reflection coefficient (R_{pp}) as a function of incident angle.

$$R_{pp} = \left[\left(b\frac{cos\theta_1}{V_{p1}} - c\frac{cos\theta_2}{V_{p2}}\right)F - \left(a + d\frac{cos\theta_1}{V_{p1}}\frac{cos\Phi_2}{V_{s2}}\right)Hp^2\right]/D \qquad \text{(B. 2)}$$

Where a,d,c,d,D,E,F,G and H coefficients are defined by the expressions:

$$a = \rho_2(1 - 2V_{s2}^2p^2) - \rho_1(1 - 2V_{s1}^2p^2), \qquad \text{(B. 3)}$$

$$b = \rho_2(1 - 2V_{s2}^2p^2) + 2\rho_1V_{s1}^2p^2 \qquad \text{(B. 4)}$$

$$c = \rho_1(1 - 2V_{s1}^2p^2) + 2\rho_2V_{s2}^2p^2, \qquad \text{(B. 5)}$$

$$d = 2(\rho_2V_{s2}^2 - \rho_1V_{s1}^2), \qquad \text{(B. 6)}$$

$$D = EF + GHp^2, \qquad \text{(B. 7)}$$

$$E = b\frac{cos\theta_1}{V_{p1}} + c\frac{cos\theta_2}{V_{p2}}, \quad \text{(B. 8)}$$

$$F = b\frac{cos\Phi_1}{V_{s1}} + c\frac{cos\Phi_2}{V_{s2}}, \quad \text{(B. 9)}$$

$$G = a - d\frac{cos\theta_1}{V_{p1}}\frac{cos\Phi_2}{V_{s2}}, \quad \text{(B. 10)}$$

$$H = a - d\frac{cos\theta_2}{V_{p2}}\frac{cos\Phi_1}{V_{s1}} \quad \text{(B. 11)}$$

The Zoeppritz equations are however not easy to handle and have a difficult physical interpretation. Some simplifications of Zoeppritz equations make possible an easy physical interpretation which can be applied practically to relate rock properties with seismic responses.

Aki-Richards (1980) gave, after a first-order linearized analysis, a Zoeppritz equation approximation which can be rearranged as:

$$R_{pp}(\theta) = \frac{1}{2}\left[\left(\frac{\Delta V_p}{V_p} + \frac{\Delta\rho}{\rho}\right)\right] - 2\left(\frac{V_s}{V_p}\right)^2\left[2\frac{\Delta V_s}{V_s} + \frac{\Delta\rho}{\rho}\right]sin^2\theta + \frac{1}{2}\frac{\Delta V_p}{V_p}(tan^2\theta - sin^2\theta) =$$

$$= R_p + Gsin^2\theta + F(tan^2\theta - sin^2\theta) \quad \text{(B. 12)}$$

Where: $\theta = \frac{\theta_1 + \theta_2}{2} \approx \theta_1, \Delta\theta = \theta_2 - \theta_1, V_p = \frac{V_{p1} + V_{p2}}{2}, \Delta V_p = V_{p2} - V_{p1}, V_s = \frac{V_{s1} + V_{s2}}{2}, \Delta V_s = V_{s2} - V_{s1}$ and $\rho = \frac{\rho_1 + \rho_2}{2}, \Delta\rho = \rho_2 - \rho_1$.

And it can be interpreted in terms of different angles (Avseth et al, 2005) where:

- $R_p = \frac{1}{2}\left(\frac{\Delta V_p}{V_p} + \frac{\Delta\rho}{\rho}\right)$ is the normal incidence reflection coefficient. (B. 13)
- $G = \frac{1}{2}\frac{\Delta V_p}{V_p} - 2\left(\frac{V_s}{V_p}\right)^2\left[2\frac{\Delta V_s}{V_s} + \frac{\Delta\rho}{\rho}\right]$ is the dominant term in intermediate angles. (B. 14)
- $F = \frac{1}{2}\frac{\Delta V_p}{V_p}$ is the dominant term in far angles, near the critical angle. (B. 15)

Wiggens or Gelfand's (Gelfand, 1986) approximation simplified even more Aki-Richards equations assuming small angles ($\tan\theta \approx \sin\theta$) and a relation $V_p/V_s=2$.

$$R_{pp}(\theta) = R_p + Gsin^2\theta \quad \text{(B. 16)}$$

where:

- $G = R_p - 2R_s$ is the AVO gradient. (B. 17)
- $R_p = \frac{1}{2}\left(\frac{\Delta V_p}{V_p} + \frac{\Delta\rho}{\rho}\right)$ is the AVO intercept. (B. 18)
- $R_s = \frac{1}{2}\left(\frac{\Delta V_s}{V_s} + \frac{\Delta\rho}{\rho}\right)$ (B. 19)

Poisson's ratio is the ratio of lateral to axial strain and it measures the compressibility of a material when an axial stress is applied: Tensile deformation is considered positive and compressive deformation is considered negative. Poisson's ratio is considered a good lithological indicator as it is related to V_p/V_s ratio in an isotropic elastic material with the equation (e.g., Gelius and Johansen, 2010).

$$\vartheta = \frac{0.5\left(\frac{v_p}{v_s}\right)^2 - 1}{\left(\frac{v_p}{v_s}\right)^2 - 1} \quad \text{(B. 20)}$$

Shuey (1985) proposed a relation between R and G and Poisson's ratio variation ($\Delta\vartheta$) for small angles based on a first order linearized analysis together with the approximation V_p/V_s=2 (and hence $\vartheta = \frac{1}{3}$).

$$\Delta\vartheta = \frac{4}{9}\left(R_p + G\right) \quad \text{(B. 21)}$$

All approximations are accurate up to 20°, with Gelfand's or Wiggens' best fit up to 35°and Shueys's approximation with accurate result in the full rank of angles up to 45° (Gelius and Johansen, 2010).

1-D convolutional trace model

AVO-AVA forward modelling uses well logs (density, V_s and V_p logs) as inputs and generates synthetic traces as outputs. The generation of these traces relies on the 1-D convolutional trace model, which is based on the assumptions:

- Horizontally layered earth model.
- Stationary source pulse (no attenuation effect).
- Noise contribution is neglected

Acoustic impedance (Z_i) is defined as the multiplication of density (ρ_i) and velocity (V_{pi}) for a given layer (Figure B.2).

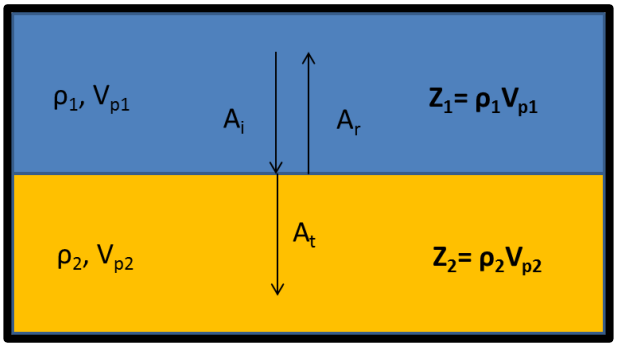

FIGURE B. 2 - P-WAVE NORMAL INCIDENT BETWEEN TWO ELASTIC MEDIA, WHERE P, V_P AND Z ARE DENSITY, P-WAVE VELOCITY AND IMPEDANCE RESPECTIVELY.

The zero offset reflection coefficient (reflected/incident wave amplitude ratio) for an interface between two layers with impedance contrast is given by:

$$R = \frac{A_t}{A_i} = \frac{Z_2 - Z_1}{Z_2 + Z_1} \quad \text{(B. 22)}$$

The earth reflectivity series is a time series of spikes, where each spike represents the reflection coefficient for a specific interface positioned at the zero-offset two-way traveltime. From the equation above, the earth reflectivity series can be computed.

Finally, according to the 1-D convolutional trace model, the seismic trace can be described as the linear convolution between the source pulse (wavelet, *w(t)*) and the earth reflectivity series.

$$x(t) = w(t) * r(t) = \int w(\tau) r(t - \tau) d\tau \quad \text{(B. 23)}$$

As it is observed in equation B.23, the wavelet is one of the most important input parameters to generate synthetic traces. A narrow wavelet with small or no sidelobes will define the boundaries between two layers better than a wider wavelet with big sidelobes.

Gassmann Fluid substitution

Fluid substitution is applied in AVO modelling as it gives information of insitu fluid scenarios and it allows the evaluation of other scenarios under different conditions (grain composition, fluid saturation or porosity).

One of the most common methods used for fluid substitution is based on Gassmann (1951) model. Porous rocks can be defined as set of grains and fluid domains with different size, shape and physical properties. When the physical properties are referred for the whole rock, then, they are called effective properties. According to Gassmann equations:

$$K = K_d + \frac{\left(1 - \frac{K_d}{K_s}\right)^2}{\frac{\Phi}{K_f} + \frac{1-\Phi}{K_s} + \frac{K_d}{K_s^2}} \quad \text{(B. 24)}$$

$$\mu = \mu_d \text{ (Fluids are not sensible to shear stress)} \quad \text{(B. 25)}$$

Where K is the effective saturated bulk modulus, Φ is the porosity, K_d is the effective bulk modulus for dry rock, K_s is the bulk modulus of the grains, K_f is the bulk modulus of the fluids, μ is the effective saturated shear modulus and μ_d is the effective shear modulus for dry rock. The main assumptions of this theory are:

- Open pore rock where all pores are connected. Note that $\mu=\mu_d$ under this conditions because shear modulus is zero for fluids.
- All the grains have the same physical properties. In case of different mineral composition, the effective elastic properties must be calculated by using effective medium models.
- Pore is fully and homogeneously saturated. In case of different phases on the fluid system, the effective elastic properties must be calculated. Wood (1955) or Reuss (1929) isostress model (Table B.1) can be used for this purpose.

$$\frac{1}{K_f^{(w)}} = \sum_{i=1}^{N} \frac{S_i}{K_{fi}} = \frac{S_{brine}}{K_{brine}} + \frac{S_{oil}}{K_{oil}} + \frac{S_{gas}}{K_{gas}} \quad \text{(B. 26)}$$

Where S_i is the saturation of fluid i and K_{fi} is the bulk modulus for fluid i. For an homogeneous mixture of brine, oil and gas $S_{brine} + S_{oil} + S_{gas} = 1$.

- In the case of low frequencies, the wavelength must be much larger than the maximum size of pores or grains (Gelius and Johansen, 2010).

Alternatively, as the effective bulk modulus for dry rock is independent of the fluid, the effective saturated bulk modulus can be computed in a reservoir saturated with a specific fluid (f_1) from the information of the effective parameters when the reservoir is saturated by other fluid (f_2).

$$\frac{K_1}{K_s - K_1} - \frac{K_{f1}}{\Phi(K_s - K_{f1})} = \frac{K_2}{K_s - K_2} - \frac{K_{f2}}{\Phi(K_s - K_{f2})} \quad \text{(B. 27)}$$

Finally, elastic parameters can be linked to seismic responses due to the relation between density, Vp and Vs and the effective elastic modules.

$$v_p = \sqrt{\frac{K + \frac{4}{3}\mu}{\rho}} \quad \text{(B. 28)}$$

$$v_s = \sqrt{\frac{\mu}{\rho}} \quad \text{(B. 29)}$$

Where the effective density for fluid mixture or grain mixture is given by an average in volume:

$$\rho = \sum_{j=1}^{M} V_j \rho_j \quad \text{(B. 30)}$$

With V_j and ρ_j are the volume fraction and density of each constituents.

In the case of saturated sandstone-shale system, equation B.30 can be expressed as:

$$\rho = (1 - \Phi)\rho_{matrix} + \Phi\rho_{fluid} \quad \text{(B. 31)}$$

Where:

- Φ is the porosity.
- $\rho_{matrix} = (1 - C)\rho_{quartz} + C\rho_{clay}$, where C is the shale volume.
- $\rho_{fluid} = S_{brine}\rho_{brine} + S_{oil}\rho_{oil} + S_{gas}\rho_{gas}$, where S_i is the saturation of element i. Note that $S_{brine} + S_{oil} + S_{gas} = 1$.

TABLE B. 1 – EFFECTIVE MEDIUM MODELS

Model name	Equation	Model assumption
Reuss (1929)	$\frac{1}{K_s^{(R)}} = \sum_{i=1}^{N} \frac{V_i}{K_{si}}$ $\frac{1}{\mu_s^{(R)}} = \sum_{i=1}^{N} \frac{V_i}{\mu_{si}}$	Iso-stress model. Represent the softest composite when mixed two materials (lower boundary). V_i and K_{si} are the fraction volume and bulk modulus of mineral i.
Voigt (1910)	$K_s^{(V)} = \sum_{i=1}^{N} V_i K_{si}$ $\mu_s^{(V)} = \sum_{i=1}^{N} V_i \mu_{si}$	Iso-strain model. Represent the stiffest composite when mixed two materials (upper boundary). V_i and K_{si} are the fraction volume and bulk modulus of mineral i.
Hill (1963)	$K^{(H)} = \frac{1}{2}\left(K^{(R)} + K^{(V)}\right)$ $\mu^{(H)} = \frac{1}{2}\left(K^{(R)} + K^{(V)}\right)$	Reuss (1929) and Voigt (1910) average.
Hashin-Shtrikman (1963)	$K^{(HS\pm)} = K_1 + \frac{V_2}{(K_2 - K_1)^{-1} + V_1\left(K_1 + \frac{4}{3}\mu_1\right)^{-1}}$ $\mu^{(HS\pm)} = \mu_1 + \frac{V_2}{(\mu_2 - \mu_1)^{-1} + \frac{2V_1(K_1 + 2\mu_1)}{5\mu_1\left(K_1 + \frac{4}{3}\mu_1\right)}}$	Upper bound (+) is computed when material 1 is the stiffest and Lower bound (-) when material 1 is the softest. K mineral can be calculated as an average: $K = \frac{1}{2}(K^{(HS+)} + K^{(HS-)})$

AVO classification scheme

Based on the variation of amplitude with offset described by Zoeppritz equations, Rutherford and William (1989) proposed an AVO classification for different types of gas sands and defined three types: Class I, Class II and Class III. Ross and Kinman (1995) identify a new

subclass (Class IIp) and Castagna and Swan (1997) included a new class (Class IV). All these classes (Figure B.3) are summarized below:

AVO Class I

Sands with higher impedance and lower V_p/V_s ratio compared with the surrounding shales. They are mature sands with high to moderate compaction and they are common in offshore areas. The reflection coefficient in the interface between cap rock (shale) and sand is large and positive at zero-offset and, then, it decreases with offset.

AVO Class II

Impedance in these sands is similar than in surrounding shales. They are moderately compacted and consolidated and they can be present in both offshore and onshore areas. In class II, the reflection coefficient in the interface between cap rock (shale) and sand is close to zero and negative at zero-offset and, then, it decreases with offset. They are difficult to see in stack sections because they are often "dim spots" (Avseth et al, 2005).

In Class IIp, the reflection coefficient is close to zero and positive at zero-offset and it decreases with offset, producing polarity change. It can sometimes be observed as negative amplitude on full stack.

AVO Class III

Sands with lower impedance compared with the surrounding shales. They are unconsolidated sands and produce "bright spots" on stacked sections. The reflection coefficient in the interface between cap rock (shale) and sand is negative and large for all offsets and it increases (more negative) with offset. It is associated with marine environment.

AVO Class IV

Impedance in these sands is lower than in the cap rock (very compacted or silty shales) and Vp/Vs ratios in cap rock are a bit higher than in sand. They are unconsolidated sands associated with areas offshore. The reflection coefficient is negative and large for all offsets and it decreases (less negative) with offset.

Cross-plot intercept vs gradient is commonly used for AVO analysis. It is based on:

- The AVO class classification scheme.
- The background trend. In the case of water saturated sandstone-shale system, this trend is given by the "mudrock line" defined by Castagna (1985).

$$V_p = 1.16V_s + 1.36 \rightarrow \frac{\Delta V_p}{\Delta V_s} = 1.16 \qquad \text{(B. 32)}$$

- All the samples that are far away from the trend in the Cross-plot are considered anomalous cases and, hence, possible gas sands. The type of sand is given by the position in the diagram (Gelius and Johansen, 2010).

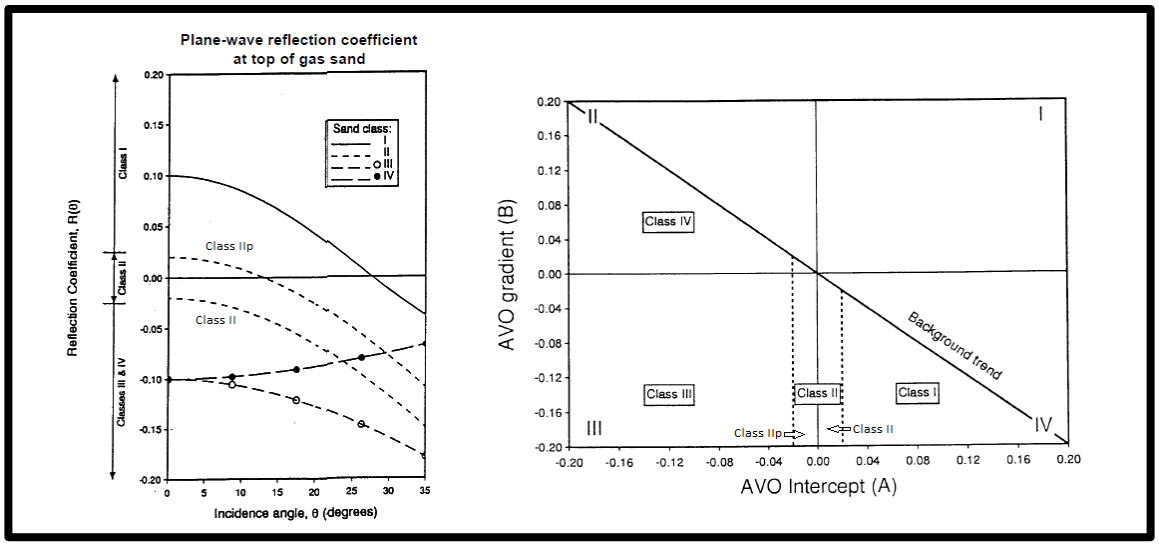

FIGURE B. 3 - AVO CLASS CLASSIFICATION. AFTER CASTAGNA ET ALT 1997

Although the AVO classes were initially defined to classify gas sands, it is commonly used to describe AVO anomalies that are not always related with gas sands (Avseth et al, 2005).

Appendix C: Well correlations

The purpose of this appendix is to show the result of well correlations when well were tied to their corresponding seismic lines.

Vøring Basin cases

Well 6707/10-1 (Nyk High) – Luva gas discovery

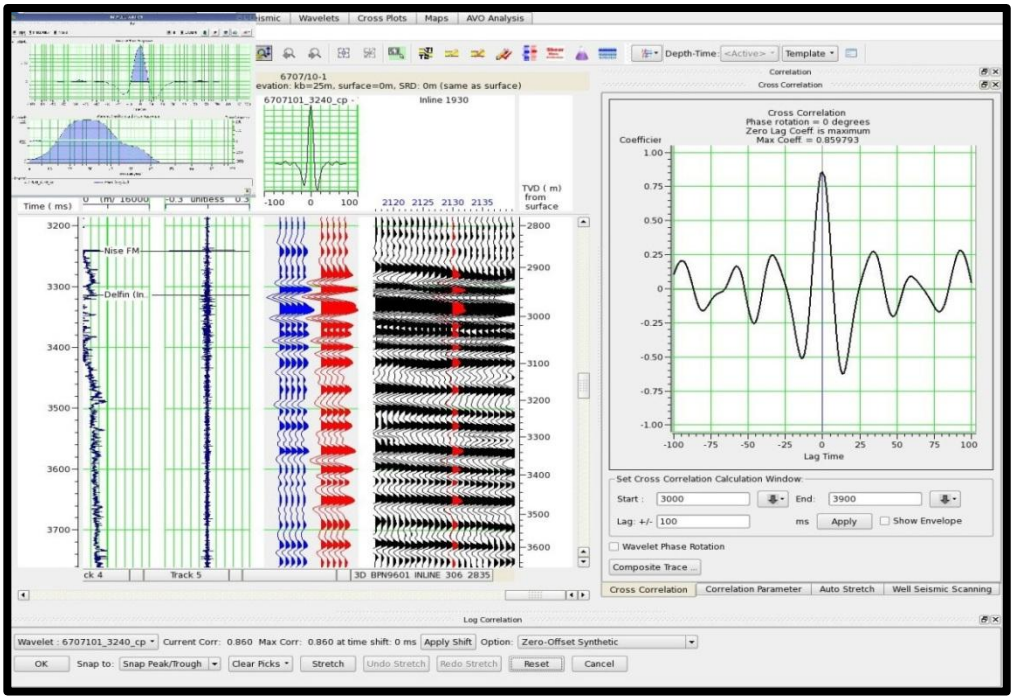

FIGURE C. 1 - SEISMIC CUBE BPN9601 AND WELL 6707/10-1 (LUVA GAS DISCOVERY) CORRELATION. THE CORRELATION IS 0.86, SHOWING A VERY GOOD MATCH BETWEEN SYNTHETIC TRACES AND ACTUAL SEISMIC DATA.

Well 6704/12-1 (Gjallar Ridge) – Marginally gas saturated sand

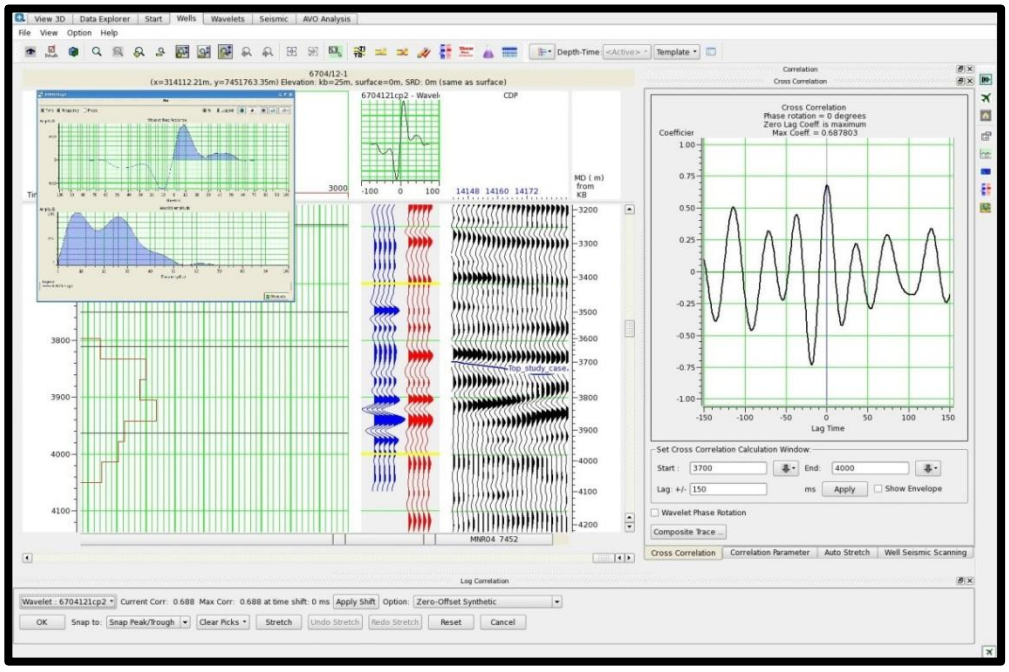

FIGURE C. 2 - SEISMIC LINE MNR04-7452 AND WELL 6704/12-1 (GJALLAR RIDGE) CORRELATION. THE CORRELATION IS 0.69, SHOWING A GOOD MATCH BETWEEN SYNTHETIC TRACES AND ACTUAL SEISMIC DATA IN THE TARGET AREA (BETWEEN YELLOW HORIZONTAL LINES).

Møre Basin cases

Well 6403/10-1 (Solsikke) – Flat lithological event

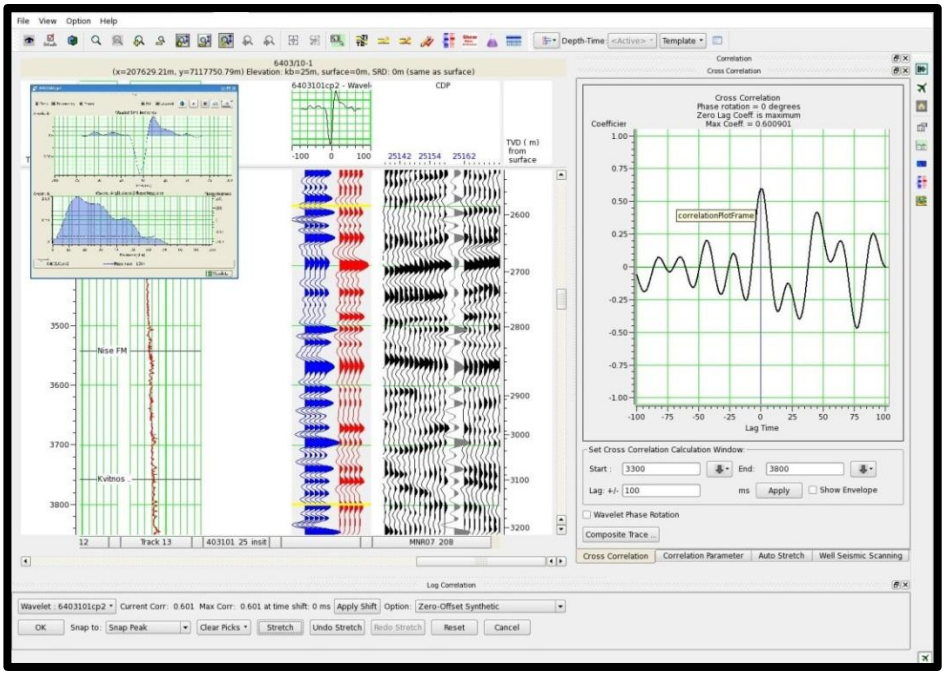

FIGURE C. 3 - SEISMIC LINE MNR07-208 AND WELL 6403/10-1 (SOLSIKKE) CORRELATION. THE CORRELATION IS 0.61, SHOWING A GOOD MATCH BETWEEN SYNTHETIC TRACES AND ACTUAL SEISMIC DATA IN THE TARGET AREA (BETWEEN YELLOW HORIZONTAL LINES).

Well 6404/11-1 – No-sand reservoir

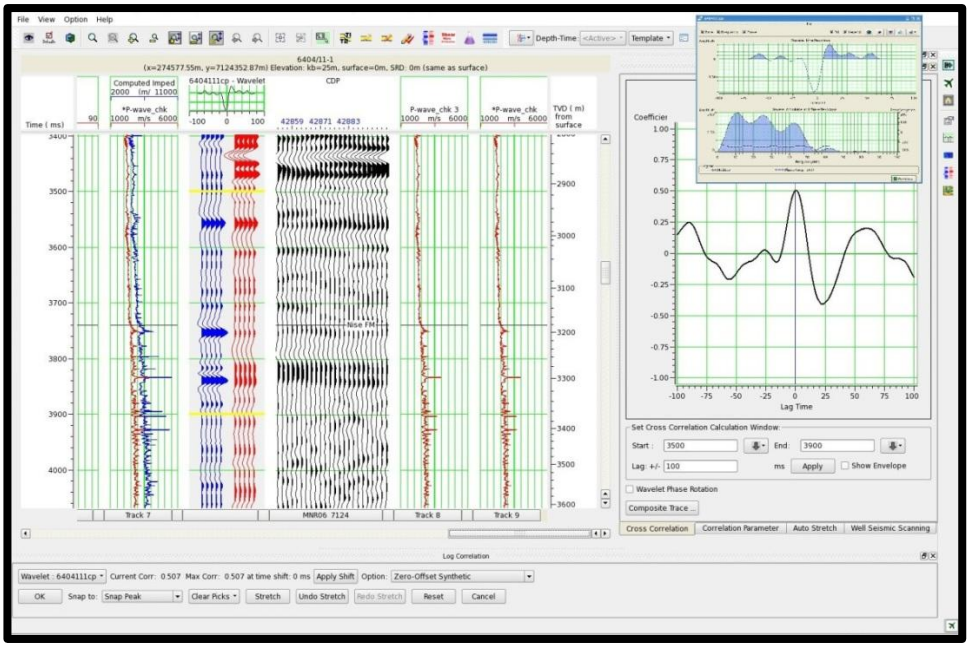

FIGURE C. 4 - SEISMIC LINE MNR06-7124 AND WELL 6404/11-1 CORRELATION. THE CORRELATION IS 0.51, SHOWING THE POOREST MATCH BETWEEN SYNTHETIC TRACES AND ACTUAL SEISMIC DATA. HOWEVER, GIVEN THAT THE DISTANCE BETWEEN THE LINE AND THE WELL IS AROUND 325 M, THIS CORRELATION IS CONSIDERED GOOD ENOUGH.

Appendix D: Flat events

This appendix shows two interpreted flat events:

- One in Luva gas discovery in Vøring Basin (Well 6707/10-1 in Nyk High) due to gas water contact (GWC).
- Other in Solsikke well (6403/10-1) in Møre Basin related with a lithological event.

Flat event– Luva gas discovery (Nyk High, Vøring Basin)

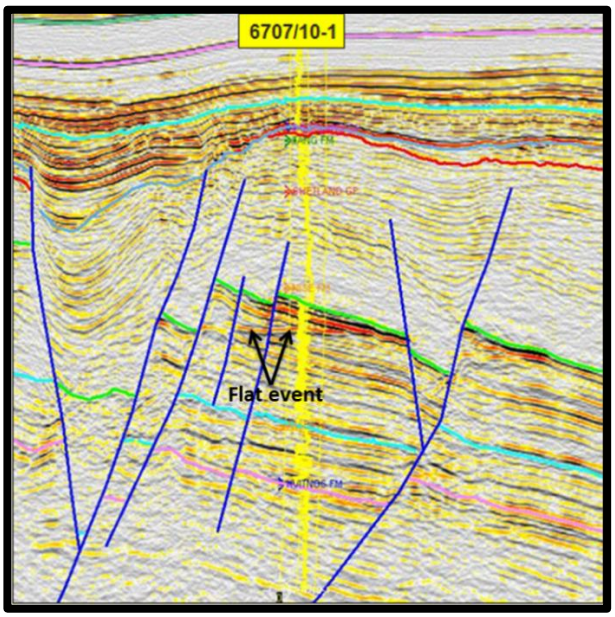

FIGURE D. 1 - INTERPRETED FLAT EVENT IN LUVA GAS DISCOVERY DUE TO GAS-WATER CONTACT (VØRING BASIN).

Flat lithological event – Solsikke (Møre Basin)

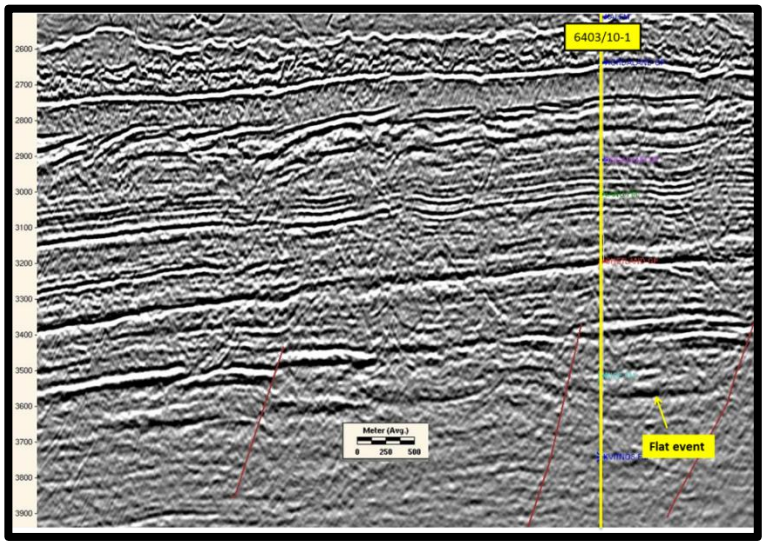

FIGURE D. 2 - INTERPRETED FLAT EVENT IN SOLSIKKE WELL (MØRE BASIN). DISPLAYED LINE IS 3002 TO BETTER SHOW THE EVENT.

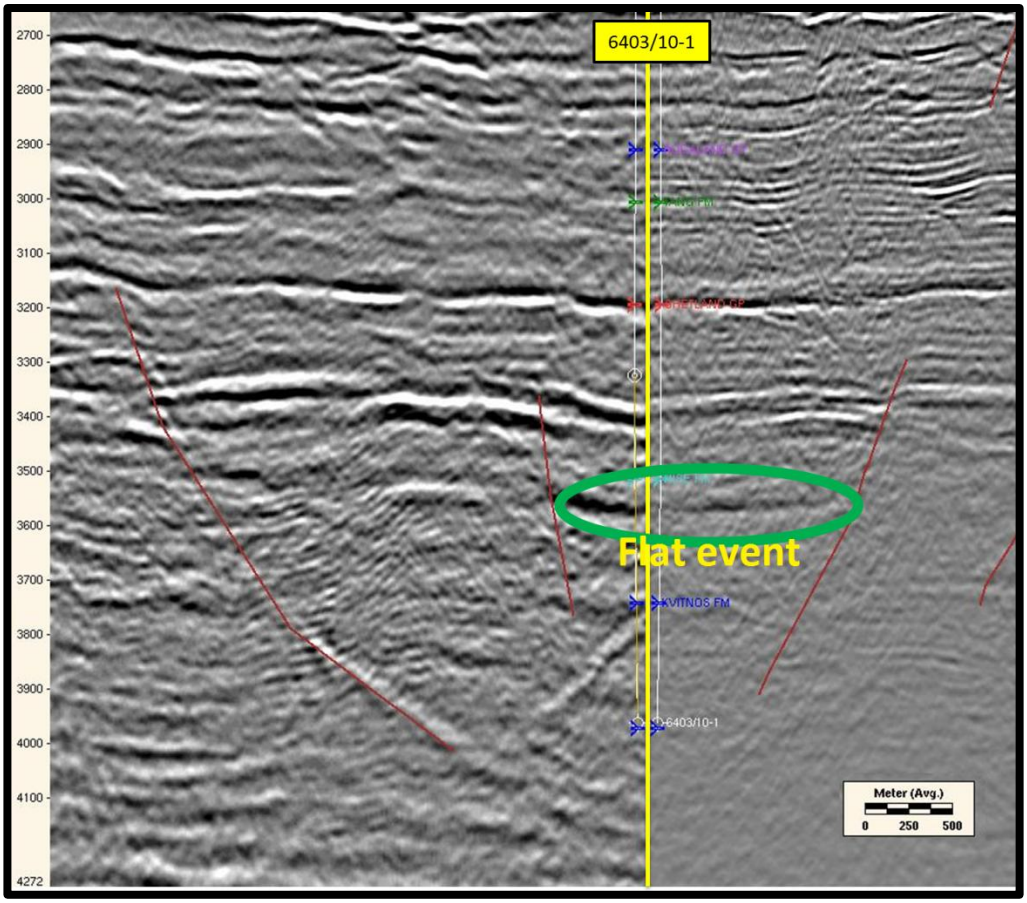

FIGURE D. 3 - INTERPRETED FLAT EVENT IN SOLSIKKE DISCOVERY (MØRE BASIN). MNR07-208 FAR STACK SECTION (LEFT) IS COMPARED WITH LINE IS 3002 (RIGHT) TO SHOW THE MATCH BETWEEN THE TWO SECTIONS. FLAT EVENT IS INTERPRETED AT AROUND 3560 MS.

Appendix E: Detailed calculation of R_p, G and F

In this appendix, Rp, G and F coefficients of the rearranged Aki-Richards (1980) first-order linearized approximation of Zoeppritz equation (Zoeppritz, 1919) are calculated as follow:

- For each target reflector, V_p, V_s, density and Poisson's Ratio are measured for upper and lower layers.
- Variations and average of V_p, V_s, density and Poisson's Ratio (υ) between layers are calculated.
- Finally, Rp, G and F coefficients are calculated based on three terms Aki-Richards approximation.

Vøring Basin cases

Well 6707/10-1 (Nyk High) – Luva gas discovery

Top

TABLE E. 1 - V_P, V_S, DENSITY AND POISSON'S RATIO IN OVERBURDEN LAYER AND IN RESERVOIR FOR IN-SITU CASE (LUVA DISCOVERY)

	Vp (m/s)	Vs (m/s)	Density (g/cm3)	Poisson's Ratio
Overburden	2808	1443	2.445	0.305
Reservoir	2613	1544	2.146	0.234

TABLE E. 2 - V_P, V_S, DENSITY AND POISSON'S RATIO VARIATION AND AVERAGE BETWEEN OVERBURDEN LAYER AND RESERVOIR FOR IN-SITU CASE (LUVA DISCOVERY)

ΔVp	ΔVs	Δρ	Δυ
-195	101	-0.299	-0.071
Vp	**Vs**	**ρ**	**υ**
2710	1493	2.295	0.266

TABLE E. 3 - RP, G AND F COEFFICIENTS IN TOP RESERVOIR (LUVA DISCOVERY)

Rp	G	F
-0.1010	-0.0388	-0.0359

Base

TABLE E. 4 - V_P, V_S, DENSITY AND POISSON'S RATIO IN RESERVOIR AND LAYER BELOW FOR IN-SITU CASE (LUVA DISCOVERY)

	Vp (m/s)	Vs (m/s)	Density (g/cm3)	Poisson's Ratio
Overburden	2755	1646	2.170	0.234
Reservoir	3042	1647	2.230	0.291

TABLE E. 5 - V_P, V_S, DENSITY AND POISSON'S RATIO VARIATION AND AVERAGE BETWEEN RESERVOIR AND LAYER BELOW FOR IN-SITU CASE (LUVA DISCOVERY)

ΔVp	ΔVs	Δρ	Δυ
287	1	0.06	0.057
Vp	**Vs**	**ρ**	**υ**
2899	1646	2.20	0.263

TABLE E. 6 - RP, G AND F COEFFICIENTS IN BASE RESERVOIR (LUVA DISCOVERY)

Rp	G	F
0.0632	0.0311	0.0495

Well 6704/12-1 (Gjallar Ridge) – Marginally gas saturated sand

TABLE E. 7 - V_P, V_S, DENSITY AND POISSON'S RATIO IN OVERBURDEN LAYER AND IN RESERVOIR FOR IN-SITU CASE (GJALLAR RIDGE)

	Vp (m/s)	Vs (m/s)	Density (g/cm3)	Poisson's Ratio
Overburden	3740	2101	2.542	0.267
Reservoir	3535	2115	2.470	0.216

TABLE E. 8 - V_P, V_S, DENSITY AND POISSON'S RATIO VARIATION AND AVERAGE BETWEEN OVERBURDEN LAYER AND RESERVOIR FOR IN-SITU CASE (GJALLAR RIDGE)

ΔVp	ΔVs	Δρ	Δυ
-205	14	-0.072	-0.051
Vp	**Vs**	**ρ**	**υ**
3637	2108	2.506	0.242

TABLE E. 9 - RP, G AND F COEFFICIENTS IN TOP RESERVOIR (LUVA DISCOVERY)

Rp	G	F
-0.0426	-0.0178	-0.0282

Møre Basin cases

Well 6403/10-1 (Solsikke) – Flat lithological event

TABLE E. 10 - V_P, V_S, DENSITY AND POISSON'S RATIO IN LAYERS ABOVE AND BELOW THE FLAT EVENT (SOLSIKKE)

	Vp (m/s)	Vs (m/s)	Density (g/cm3)	Poisson's Ratio
Above flat event	2387	1040	2.260	0.382
Below flat event	2494	1057	2.275	0.389

TABLE E. 11 - V_P, V_S, DENSITY AND POISSON'S RATIO VARIATION AND AVERAGE BETWEEN LAYERS ABOVE AND BELOW THE FLAT EVENT (SOLSIKKE)

ΔVp	ΔVs	Δρ	Δυ
107	17	0.015	0.007
Vp	**Vs**	**ρ**	**υ**
2441	1049	2.268	0.386

TABLE E. 12 - RP, G AND F COEFFICIENTS IN FLAT EVENT (SOLSIKKE)

Rp	G	F
0.0252	0.0075	0.0219

Well 6404/11-1 – No-sand reservoir

TABLE E. 13 - V_P, V_S, DENSITY AND POISSON'S RATIO IN LAYERS ABOVE AND BELOW THE REFLECTOR (6404/11-1)

	Vp (m/s)	Vs (m/s)	Density (g/cm3)	Poisson's Ratio
Above reflector	2610	1139	2.330	0.381
Below reflector	2660	1177	2.340	0.377

TABLE E. 14 - V_P, V_S, DENSITY AND POISSON'S RATIO VARIATION AND AVERAGE BETWEEN LAYERS ABOVE AND BELOW THE REFLECTOR (6404/11-1)

ΔVp	ΔVs	Δρ	Δυ
50	38	0.010	-0.004
Vp	**Vs**	**ρ**	**υ**
2635	1158	2.335	0.379

TABLE E. 15 - RP, G AND F COEFFICIENTS IN REFLECTOR (6404/11-1)

Rp	G	F
0.0116	-0.0175	0.0095

Appendix F: Interval velocity estimation and depth conversion with NORSAR-2D.

The purpose of this appendix is to give an example of the detailed steps followed during interval velocity estimation from stacking velocity and the depth conversion.

Velocity estimation process is showed in Figure F.1:

- The velocity estimator needs an initial model in depth as input. In this case, the model has two layers with a constant Vp corresponding to the sea water (1480 m/s) separated by the seabed interface (previously depth migrated) (Figure F.1a).
- Stacked velocity grid is computed from smoothed stacking velocity functions (Stab files). Stab files were created from Charisma stacking velocity files (VBASE) by using the script in appendix G. CMP positions from which the velocity will be estimated are also loaded in this step (Figure F.1b).
- The selected horizon is displayed in time domain. Note that these horizons must be always selected from shallow to depth. On the top, red triangles identify the CMP position at which the velocity will be estimated (Figure F.1c).
- The first time horizon below seabed is selected and the uncertainties and acceptance limits for velocity estimation are set (5% on the stacking velocity and of 100% on the interval velocity in this case). The velocity sample file has the same name as the horizon used for the estimation. The [Estimate] button starts the process (Figure F.1d).

- The output velocity sample file is displayed in the velocity domain. Every interval velocity sample has associated a measurement of the uncertainty. Note that the deeper the horizon is, the larger the uncertainty will be. This is because for each new horizon, the previous internal velocities are used and, hence, their uncertainties are propagated (Figure F.1e).

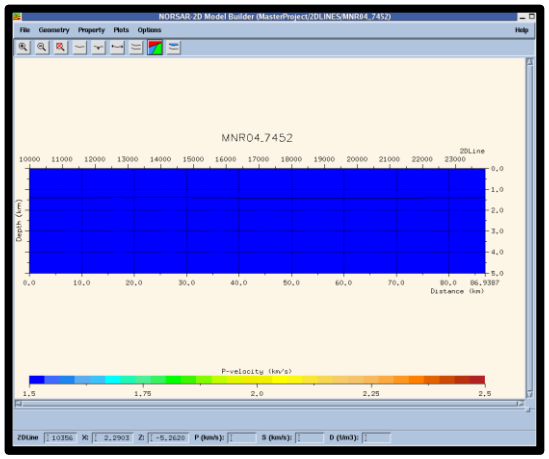

(A) INITIAL MODEL IN DEPTH

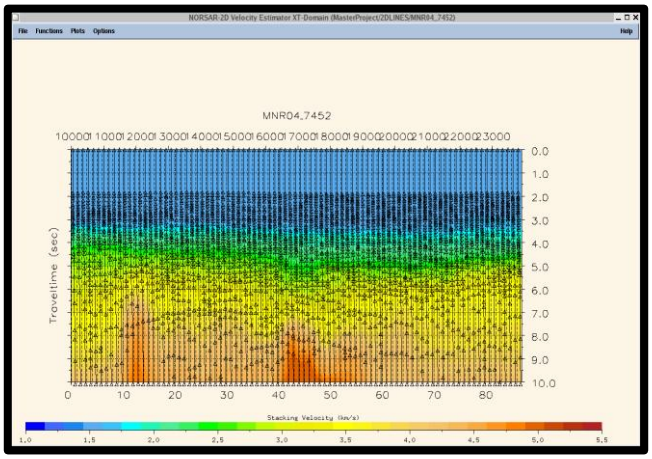

(B) STACKING VELOCITY GRID

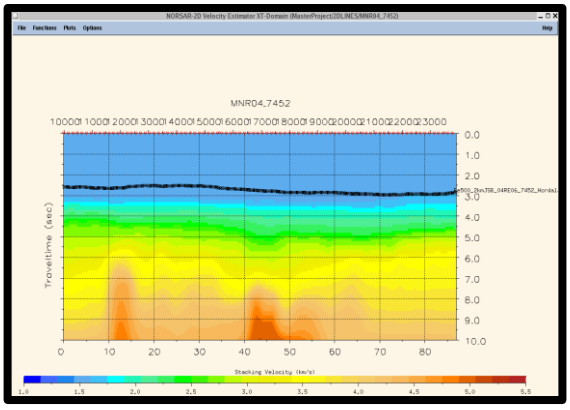

(C) HORIZON USED FOR ESTIMATION IN TIME DOMAIN

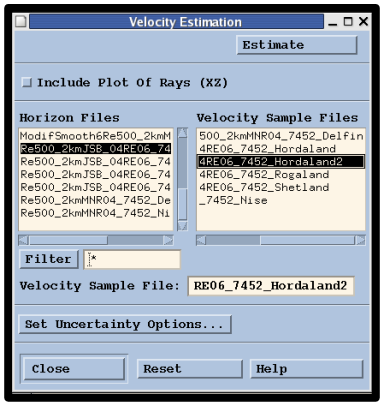

(D) VELOCITY ESTIMATOR

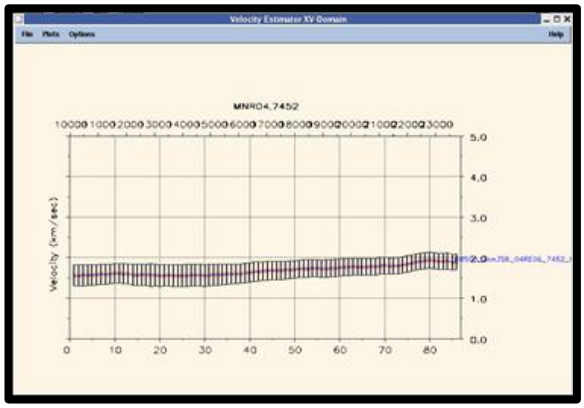

(E) ESTIMATED VELOCITY

FIGURE F. 1 - NORSAR-2D VELOCITY ESTIMATOR.

Depth conversion process is showed in Figure F.2:

- The velocity sample (output of previous step) file is loaded in NORSAR-2D model builder and it can be modified and smoothed before creating a sampled velocity function (constant, linear trend or spline representation). In the example, spline is selected with an increment every 500m (Figure F.2a).
- When the velocity function is stored, it is assigned to the deepest layer in the model. The corresponding horizon (Hordaland, in the example) is finally depth converted with image ray tracer technique (Figure F.2b).
- A new model is created with an additional layer below the depth-converted horizon. This model can be loaded in NORSAR-2D velocity estimator module and repeat the same process for the rest of the horizons (Figure F.2c).

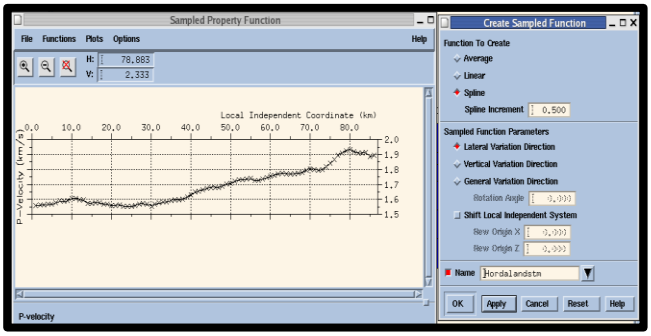

(A) SAMPLE VELOCITY FUNCTION

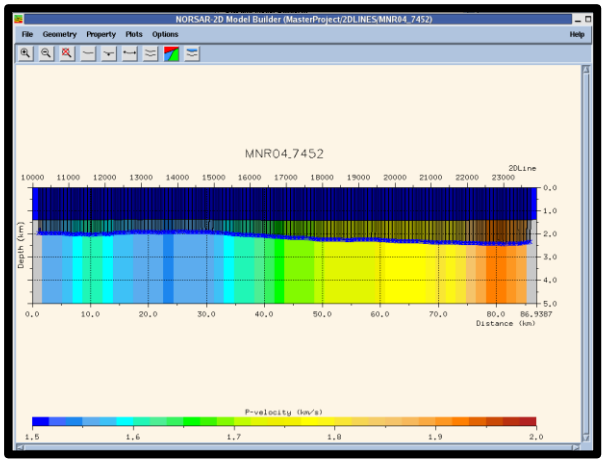

(B) DEPTH CONVERSION

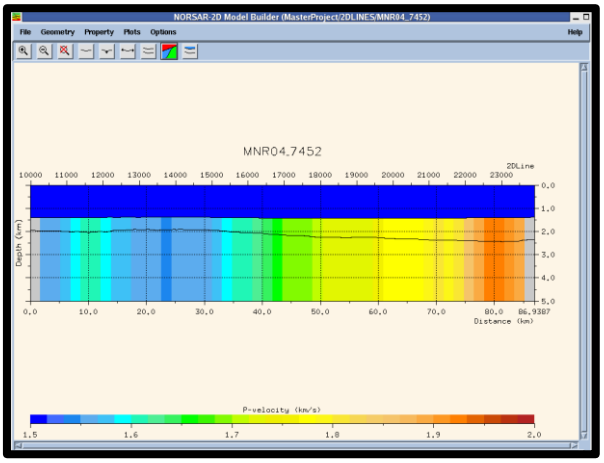

(C) FINAL MODEL

FIGURE F. 2 - DEPTH CONVERSION.

Appendix G: Script to convert stacking velocity from Charisma (*.VG_VBASE) to NORSAR-2D (*.Stab) format.

The following script is developed in vbscript and it can be executed in any windows platform. It covers charisma VG_VBASE files containing stacking velocities into NORSAR-2D format (*.Stab). Details of these formats can be found in Charisma and NORSAR-2D manuals.

```
'Scriptname: VBASE2STAB.vbs.
' Language: vbscript.
'Seismic line information
line = "name_of_section" 'example: "MNR06-7124"
nInitCDP = InitialCDP 'example: 26813
nStep = SeparationBetweenCDPs 'example: 0.0062164
strVBase = InputCharismaFile 'example: "MNR06_7124_VBASE.dat"
'Output files
foutput = OutputN2Dfile 'example: "Final_" & line & ".Stab"
'Main program
Set fso = CreateObject("Scripting.FileSystemObject")
Set VBaseFile = fso.OpenTextFile(strVBase)
Set outfile =  fso.CreateTextFile(foutput,true)
outfile.Writeline("tabular property-1")
outfile.Writeline("    1    1    2    6    1")
do while not VBaseFile.AtEndOfStream
   fName =  VBaseFile.ReadLine()
   If InStr(fName, "CDP")<>0 then
                        strLine = left(fName,29)
                        strLine = Replace(strLine, "SP", "")
                        strLine = Replace(strLine, "CDP", ";")
                        strLine = Replace(strLine, "NV", ";")
                        arrRef = split(strLine,";")
      strSP = Trim(arrRef(0))
      strCDP = Trim(arrRef(1))
                        strNV = Trim(arrRef(2))
                        xpos = round((int(strCDP) - nInitCDP)*nStep,4)
                        strLine = strSP & "-" & strCDP & "-" & xpos & "-" & strNV
                        sout = "*****************************" & vbCrLf
                        sout = sout & "   " & xpos & "       " & strCDP & "       " & strNV
                        outfile.writeline(sout)
                        else
                        VTpair = split(fName,"T")
                        for each pair in VTpair
                        If InStr(pair, "V")<>0 then
                                    Data = split(pair,"V")
                                    ms = trim(Data(0))
                                    ks = round(int(ms)/1000,4)
                                    mse = trim(Data(1))
                                    se = round(int(mse)/1000,4)
                                    sout = "   " & ks & "     " & se
                                    outfile.writeline(sout)
                                    end if
            next
          end if
loop
outfile.close
'Change "," by "." as decimal separator
Set outfile = fso.OpenTextFile(foutput)
contents = outfile.readall
outfile.close
Rep2 = replace(contents,",",".")
fouttmp = "tmp_" & foutput
Set outfiletmp =  fso.CreateTextFile(fouttmp,true)
outfiletmp.write Rep2
outfiletmp.close
fso.deletefile foutput
fso.MoveFile fouttmp, foutput
```

Glossary

- **AVA** – Amplitude versus angle.
- **AVO** – Amplitude versus offset.
- **Common Midpoint (CMP)** – For a source-receiver pair, the midpoint can be calculated. Traces with common midpoint between sources and receivers are gathered in groups called CMP gathers. In the case of horizontal layers, traces from the same CMP are reflected in the same CDP (common depth point).
- **Dix approximation** – In horizontal and parallel layers, the interval velocity for a layer between two reflectors can be approximated by:

$$v_{int} \cong \sqrt{\frac{t_n v_{RMS_n}^2 - t_{n-1} v_{RMS_{n-1}}^2}{t_n - t_{n-1}}} \qquad \text{(Gl. 1)}$$

  where v_{int} is the interval velocity in the layer number n, t_{n-1} and t_n are the traveltimes of the first and second reflectors and v_{RMSn} and v_{RMSn-1} are the RMS velocities (approximated by stacking velocities) of the n and n-1 layers.

- **Fan system** - Accumulation of land-provenance sediments on the basin-floor normally through submarine canyon-channel systems.
- **GWC** – Gas-water contact.
- **Normal Move Out** – It is the difference between a certain offset traveltime and the zero-offset traveltime in a CMP gather. This difference must be corrected before stacking (NMO correction).
- **Play –** Group of known or proposed hydrocarbon accumulations with similar geologic, geographic and temporal characteristics, e.g., similar source rock, migration pathways, timing, trapping mechanism and hydrocarbon type.
- **Root-mean-square velocity (V_{RMS})** – it is the effective velocity of a wave travelling from the surface to a given reflector. It is defined as:

$$V_{RMS} = \sqrt{\frac{\sum v_i^2 \Delta t_{i0}}{\sum \Delta t_{i0}}} \qquad \text{(Gl. 2)}$$

  where V_{RMS} is the root-mean-square velocity in the layer n, v_i is the interval velocity in layer I and Δt_{i0} is the vertical traveltime in layer i. V_{RMS} can be approximated by stacking velocity for horizontal reflectors and small offsets.

- **Stacking velocity** – The traveltime variation with the offset can be expressed with the hyperbola:

$$t^2 \cong t_0^2 + \frac{x^2}{v^2} \qquad \text{(Gl. 3)}$$

  where t_0 is the traveltime at zero-offset, x is the offset, t is the traveltime at offset x and v is the velocity. The stacking velocity is the velocity that will give the best stack

of the data. If v=stacking velocity, the difference between t and t_0 after NMO correction should be zero.

In NOSAR2D, the "stacking velocity function" represents the stacking velocity variations with depth for a specific CMP.

- **Interval velocity** – It is the velocity within a layer (or block).
- **Image Ray** – Ray path starting at the surface in the vertical direction, used for local depth conversion of a Migrated Time Horizon (MTH).
- **Seismic model** (ray tracing model in NORSAR-2D – In the context of this study, the seismic model is represented by:
    - Interfaces – Surfaces representing the discontinuity between two mediums with different physical properties (Figure Gl1a). In NORSAR2D, each interface must have two intersections (with the model box or with other interface).
    - Blocks or layers – Zones between surfaces (Figure Gl1b).
    - Material properties – Density, V_p and V_s assigned to each block. These properties can be constant or defined by a function (Figure Gl1c).

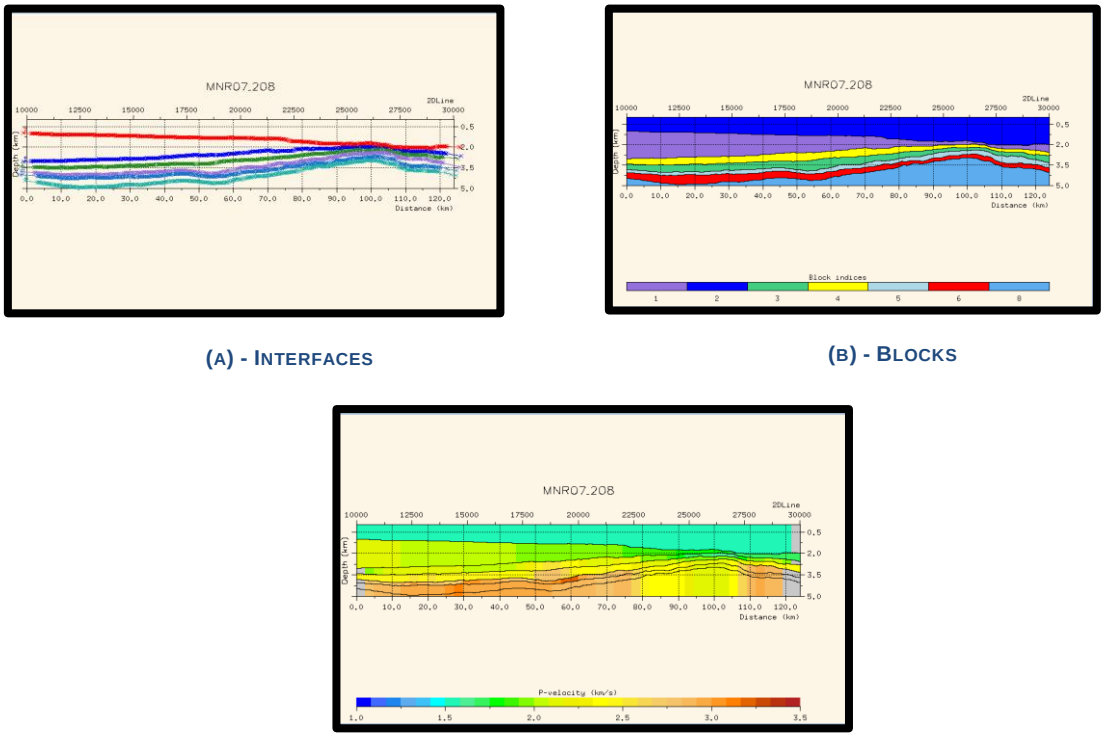

(A) - INTERFACES

(B) - BLOCKS

(C) – MATERIAL PROPERTIES (V_P)

FIGURE GL. 1 - SEISMIC MODEL EXAMPLE. SEISMIC LINE MNR07-208.

- **Tuning effect** – Constructive or destructive interference of waves from closely spaced reflectors. Tuning effect starts when the spacing between reflectors is lower than Tuning thickness.